UNIVERSITÉ DE STRASBOURG

ÉCOLE DOCTORALE DES SCIENCES CHIMIQUES

UMR 7140 & UMR 7515

THÈSE présentée par :

Nizami ISRAFILOV

soutenue le : **30 Septembre 2022**

pour obtenir le grade de : **Docteur de l'Université de Strasbourg**

Discipline/ Spécialité : Sciences Chimiques

Élaboration de nouveaux matériaux de types MOF dotés de fonctionnalités supramoléculaires. Synthèse, études physicochimiques et applications.

THÈSE dirigée par :	
M. PLANEIX Jean-Marc	Professeur, Université de Strasbourg
M. LOUIS Benoît	Directeur de Recherche CNRS, Université de Strasbourg
RAPPORTEURS :	
M. DEVIC Thomas	Directeur de Recherche, Université de Nantes
M. FARRUSSENG David	Directeur de Recherche CNRS, IRCE Lyon
AUTRES MEMBRES DU JURY :	
Mme BOURRELLY Sandrine	Maîtresse de Conférence, Université de Aix-Marseille
M. DAOU Jean	Professeur, Université de Haute Alsace
INVITÉ :	
M. FRANÇOIS Yannis	Maître de Conférence, Université de Strasbourg

Dedicated to my daughter Asena

Table of contents

Acknowledgments

Firstly, I want to thank the members of the jury, Dr. Thomas Devic, Dr. David Farrusseng, Prof. Jean Daou, Dr. Sandrine Bourrelly, and Dr. Yannis Francois, who spent one of the most precious things – their time to read and/or assess my thesis.

I also express my gratitude to Prof. Mir Wais Hosseini, for acceptance, to work in his laboratory, for his precious advice, and his confidence in me. He was an example scientist for me, working in his laboratory was a big responsibility and at the same time a big motivation for me. Also, I show courtesy to the director of ICPEES Prof. Guy Schlatter, where I conducted part of the work.

Next, I represent my appreciation to my thesis directors Prof. Jean-Marc Planeix and Dr. Benoit Louis. If I write everything they made for me, it will be another 200 pages thesis. I thank them for believing in me in all steps of my Ph.D.

My following gratitude goes to all members of the laboratory. Everyone in the laboratory helped me, with their technical skills, advice, valuable discussions, etc. Especially, during the first days (months) of my thesis, the guidance of Audrey with her technical skills was decisive for the formation of my own approach to synthesis and purification. Also, I thank Aziz for his advice and technical help. As he has a huge experience, his advice helped me a lot to do difficult reactions in the simplest ways. I want to thank also to Nathalie for obtaining beautiful structures with ugly crystals.

Moreover, I thank other members and non-members of both laboratories where I worked, Stephane, Sylvie, Veronique, Thierry, Sanaa, Ashok, Muthu, Sukhen, Renata, and Julien for their advice, support, analyses, help, etc.

I want also to express my gratitude to the members of the SATT-Conectus for accompanying us on this adventure. Especially to Anais- manager of our project.

Later, I want to show courtesy to the technical staff who cleaned our rooms, and laboratories, repaired water leaks, transported the waste solvents, etc.

I want also to appreciate the help of my parents. Without their help, I could not do my Ph.D. I am not even talking about their effort to grow me up.

Life is like a synthesis of crystals, despite the main ingredients being salt, ligand, and solvent, a trace amount of impurity or small quantity of modulator can change the fate of the reaction. That's why I thank all people, kind or not, who have contributed to the formation of my identity. Finally, I thank God, for this complex algorithm and even for the "impurities" that led me here.

List of abbreviations

MOF- Metal Organic Framework
SBU- Secondary Building Unit
MIL- Materials Institute Lavoisier
ULM- University Le Mans
BTC- Benzene Tri Carboxylate
DAC- Direct Air Capture
CCS- Carbon Capture and Storage
OMS- Open Metal Sites
CUS- Coordinatively Unsaturated Sites
OCS- Open Coordination Sites
HKUST- Hong-Kong University of Science and Technology
UiO- University of (i) Oslo
NOTT- Nottingham University
ZIF- Zeolitic Imidazolate Framework
TPTC- TerPhenyl TetraCarboxylic
PCN- Porous Coordination Network
UTSA- University of Texas in San-Antonio
MMM- Mixed Matrix Membrane
PEG- Polyethylene Glycol
DMF- DiMethylFormamide
THF- TetraHydroFuran
XRD- X-Ray Diffraction (P-Powder, SC-Single Crystal)
FT-IR- Fourier Transform Infra-Red
UV-Vis- Ultra-Violet Visible
TGA- Thermo Gravimetric Analysis
SEM- Scanning Electronic Microscope
TEM- Transmission Electronic Microscope
BET- Branuer- Emmett Teller
DMA- DiMethylAcetamide
SUM- Strasbourg University Materials
LBM- Le Bel Materials
SBA- Santa Barbara Amorphous
MB- Methylene Blue
MO- Methyl Orange
PPM- Part Per Million
PFO- Pseudo First Order
PSO- Pseudo Second Order
VOC- Volatile Organic Compound

Résumé

Introduction

Les MOF ou Metal Organic Frameworks constituent une classe de polymères de coordination associant deux types d'unités de construction (tectons*) des ions métalliques et des ligands organiques. Les assemblages de ces unités conduisent à des structures mono-, bi- ou tridimensionnelles de topologie et géométrie variées. Théoriquement, des millions de structures de MOF sont possibles et 500 000 d'entre elles sont prédites. A ce jour, plus de 90 000 MOF ont été synthétisés [1].

Connu dès le 18ème siècle, le bleu de Prusse composé d'ions de fer et de cyanure est constitué de structures polymériques de coordination. Le bleu de Prusse et ses analoguessont encore aujourd'hui utilisés pour la catalyse, le stockage de gaz ou encore comme aimants moléculaires [2]. Depuis cette époque différents composés de coordination et organométalliques ont été synthétisés, la nature de la liaison entre un centre métallique et un ligand pouvant varier fortement selon que l'on s'intéresse à l'acétate de zinc [3], au ferrocène [4] ou aux polyoxométalates [5]… Une nouvelle étape pour la synthèse et l'étude de polymères de coordination synthétiques 3D a été ouverte par R. Robson et B.F. Hoskins dans les années 1990 [6]. Ils ont synthétisé en particulier des polymères de coordination à base de cuivre et de zinc.

L'élimination des solvants piégés dans ces cavités à l'issue de leur synthèse conduit à des modifications significatives de leurs propriétés structurales et de leurs propriétés. En outre, ils ont prédit les futures améliorations et applications possibles de ces matériaux. Ci-dessous, l'une des conclusions intéressantes est tirée de leur article original :

"Despite Nature's abhorrence of a vacuum it may be possible to devise rods with sufficient rigidity to support the existence of solids with relatively huge empty cavities. Materials combining good or even high thermal, chemical, and mechanical stability with unusually low density may thereby be afforded"

Au cours de la même période, les travaux sur la synthèse de structures plus rigides se sont intensifiés et au milieu des années 90, plusieurs groupes O. Yaghi [7], S. Kitagawa [8] et G. Ferey [9] ont décrit de nouveaux matériaux qu'ils ont nommés MOF et qui avaient une surface spécifique élevée, dépassant parfois celle des adsorbants bien connus tels que les zéolithes ou le charbon actif.

Plus tard en 1999, Yaghi et al. ont synthétisé un MOF (MOF-5) dont la structure est celle d'un polymère de coordination tridimensionnel et qui, en raison de sa microporosité possède une très grande surface spécifique [10] (fig. 1).

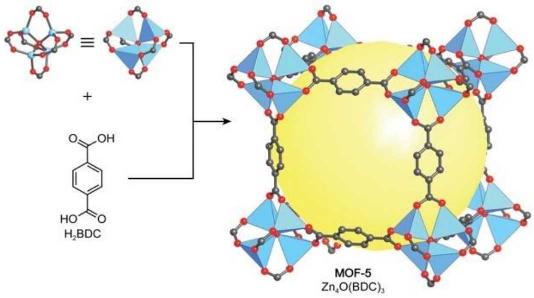

Figure 1. MOF-5 de Yaghi.

Aujourd'hui encore, c'est l'un des composés de type MOF de référence, les unités de construction des MOF étant des ligands organiques et des ions métalliques (ou clusters). Dans la terminologie des MOF, cette dernière est appelée SBU-Secondary Building Unit. La SBU du MOF-5 est composé nœud de [ZnO4] et le ligand organique est l'acide téréphtalique. En général, le zinc et le cuivre font partie des métaux couramment utilisés dans la synthèse des MOF, pouvant former d'autres type de SBU. Au milieu des années 90, d'autres groupes ont développé des MOF. En France, les pionniers de ce domaine furent l'équipe de Gérard Ferey et Christian Serres à l'Institut Lavoisier de l'Université de Versailles Saint-Quentin-en-Yvelines. Leurs résultats ont ouvert une nouvelle voie dans la synthèse des MOF avec la série des MIL (Matériaux Institut Lavoisier) qui présentent le très grand avantage d'être stables en milieu aqueux. La principale raison de leur stabilité repose sur la « force » de la liaison de coordination des SBU, composés d'ions Fe et Cr formant un cluster très stable avec des atomes d'oxygène. La taille des pores est modulable par le choix de ligands de « longueurs » variables, les MOF ont ainsi des applications potentielles très variées (fig. 2). Leurs applications se déclinent de la simple utilisation pour l'adsorption jusqu'à celles du diagnostic médical ou du traitement de cancer en passant par la catalyse...

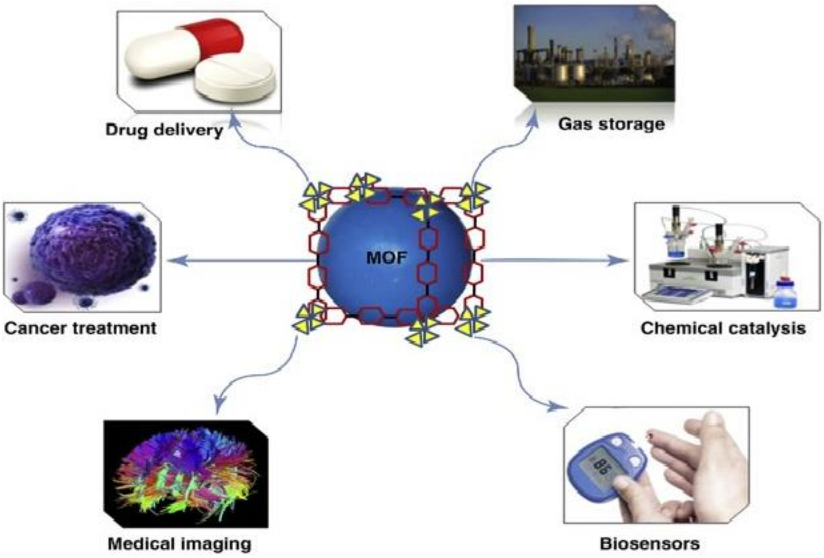

Figure 2. Les domaines d'utilisation des MOF

Malgré les nombreuses applications des MOF décrites dans des études fondamentales, les MOF ne sont pas toujours pas utilisés à l'échelle industrielle. En dépit des performances exceptionnelles de certains MOF, leur coût comme leur sensibilité aux milieux ambiants limitent aujourd'hui significativement leur application à grande échelle.

La problématique de cette étude peut être résumée par les quelques questions suivantes :

Peut-on préparer efficacement des MOF à partir de ligands possédant des fonctions de « reconnaissance » supramoléculaires ? Comment la présence de telles fonctions influe-t-elle sur la stabilité et sur les propriétés structurales de ces solides ? Ces nouveaux matériaux peuvent-ils être utilisés dans les principales applications des matériaux poreux comme l'adsorption en phase gazeuse ou liquide, la séparation ou l'extraction ? Ces nouveaux matériaux apportent-ils des propriétés nouvelles ou différentes ? Comment les interactions supramoléculaires interviennent-elles ou sont-elles à l'origine de telles propriétés ?

Résultats et discussions

Les ligands synthétisés dans ce travail sont représentés sur la figure 3.

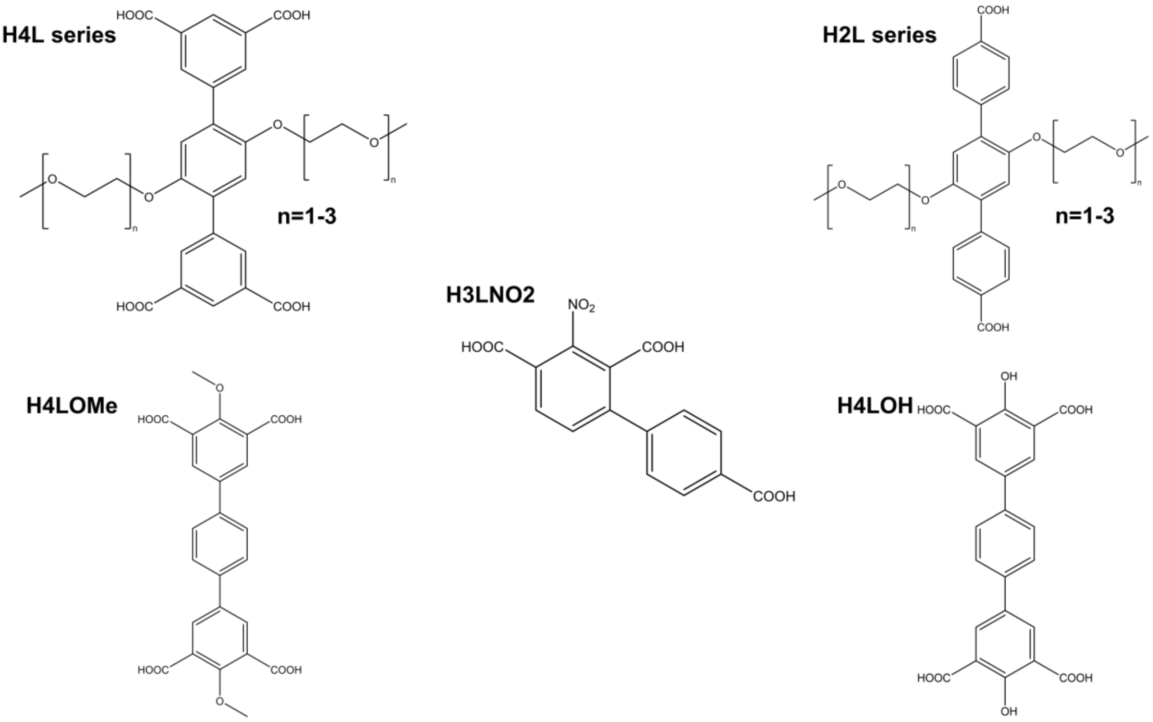

Figure 3. Tous les ligands synthétisés.

La nomenclature des ligands est basée sur le nombre d'atome d'oxygène dans la chaîne, plutôt que sur le nombre n de chaînes éthylèneoxy. Ainsi, le nom du ligand comporte le fragment L n+1. Par exemple, pour H4L3, le nombre n de chaînes éthylèneoxy est égal à 2. Les ligands et les MOF semblant les plus intéressantes sont ceux obtenus à partir des ligands H4L2 et le H4L3.

Une série de MOF a été obtenue pour chaque ligand par coordination de différents métaux, ceux précisés ci-dessous ont pu être caractérisés par diffraction de rayons X sur monocristaux.

Tableau 1. Les MOFs synthétisés.

Ligand	H4L2	H4L3	H4L4	H2L2/bipy	H2L3	H2L4	H4LOMe	H4LOH
Métal	Cu ,Ni,Ca	Cu,Zn,Ni, Ca,Mg	Cu ,Ni,Ca	Zn	Zn,Zr	Zn	Cu,Zn,Ca	Cu, Ca

Alors que le NOTT-101 (MOF au cuivre constitué d'un ligand analogue sans chaînes latérales) n'est pas stable dans l'eau. (NOTT- est abréviation qui vient de Université de Nottingham), nous avons montré que l'ajout de chaînes latérales de diglyme a donné au MOF une stabilité dans l'eau en augmentant considérablement les domaines d'application de ces MOF.

Les ligands de types de H2L et H4L ont été synthétisés en plusieurs (3-5) étapes intégrant la synthèse d'éther de Williamson, le couplage Suzuki-Miyaura et les réactions de saponification. La caractérisation complète (H-NMR, C-NMR, LR-MS, analyse élémentaire) de ces ligands est reportée dans la partie expérimentale et dans l'ESI de l'article publié [12]. Plus tard, sur la base de ce ligand, nous avons synthétisé le MOF correspondant à base de cuivre. A cet effet, le sel de nitrate de cuivre et le ligand ont été chauffés dans une solution de DMF dans des conditions légèrement acides. Après 24 heures, la poudre microcristalline bleue a été filtrée et rincée avec du DMF. Les MOF sont nommés SUM-102 (glyme), 103 (diglyme) et 104 (triglyme) (SUM étant selon la pratique du domaine l’acronyme de Strasbourg University Materials). Pour ces trois MOF, les analyses SCXRD et PXRD montrent la même topologie et le même mode de connectivité des ligands tétracarboxyliques que le parent NOTT-101. Cependant, l’analyse des monocristaux de ces matériaux montre que l’organisation des chaînes latérales dans la cavité est désordonnée, l’affinement de la position de ces chaînes n’étant pas possible à partir des données de diffractions. Comme prévu, la poudre XRD de SUM-102, SUM-103 et SUM-104 ont montré pour la structure globale du réseau une correspondance exacte avec NOTT-101 (fig. 4).

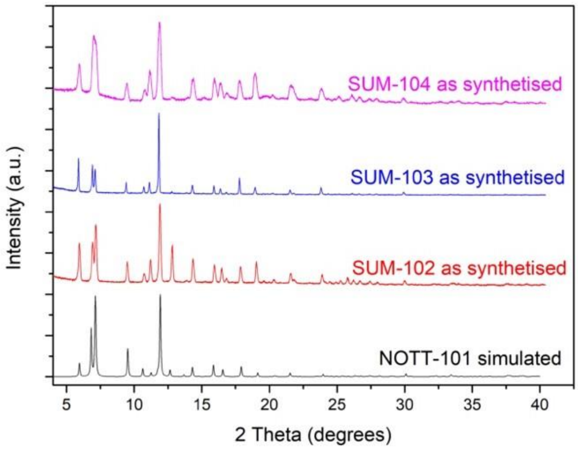

Figure 4. DRX des MOFs de série de SUM-100 (Cu@H4L).

De même, après chauffage sous vide pendant 8 h à 160 °C et réexposition à l'air ambiant, le SUM-103 ne subit aucune altération structurale. Dans le cas du SUM-102, une perte significative de cristallinité a été observée. Contrairement à SUM-103 (et dans une certaine mesure à SUM-102), la cristallinité de NOTT-101 a presque complètement disparu après activation. Schröder *et al.* [13] pour le NOTT-101 et Zhou *et al.* [14] pour le Cu2(TPTC-OMe) ont rapporté une telle dégradation en présence d'eau ou d'humidité.

De manière systématique, les MOF ont été caractérisés par les méthodes usuelles (FT- IR, XRD, TGA, BET) ces résultats sont commentés dans le manuscrit.

Avec la même série de ligand (H4L), des MOF de nickel ont synthétisés et étudiés. Pour tous ces MOF, des cristaux de bonne taille ont été obtenus. Cependant leur faible pouvoir diffractant ne nous a pas permis d'exploiter de manière approfondie ces données de DRX. De plus, un MOF au nickel a été synthétisé avec un ligand modifié par des groupements méthoxy. Ce ligand a été synthétisé auparavant par Zhou *et al.*[11], nous avons pu cependant obtenir un nouveau MOF. Nous avons réussi à résoudre partiellement la DRX monocristalline de ce MOF qui montre qu'il possède une structure identique à celle des analogues à chaîne plus longue. Dans la figure 5, sont reportés la forme des cristaux ainsi qu'une représentation de la structure cristalline montrant la nature poreuse de ce réseau cubique.

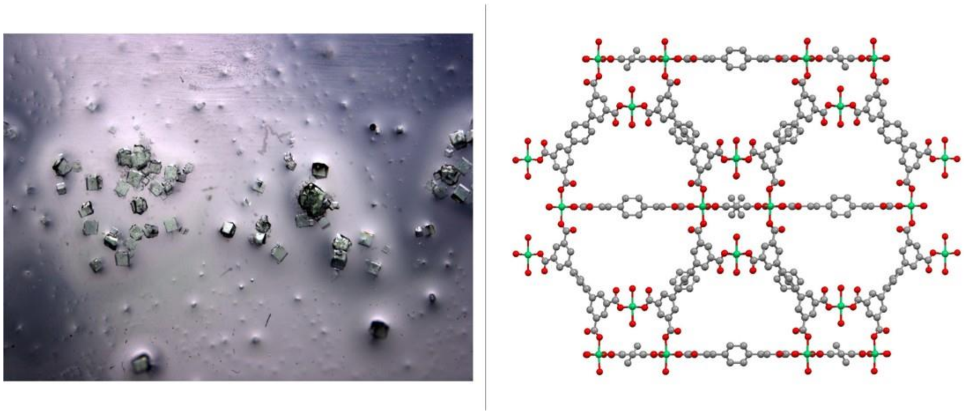

Figure 5. Photo de SUM-203 (Ni@H4L3) et vue de la porosité de SUM-201 (Ni@H4L1). Les groupes latérauxont été éliminés pour une meilleure visualisation.

De plus, nous avons poursuivi nos recherches sur le remplacement des métaux coûteux et toxiques par des métaux moins chers et biocompatibles. Nous avons réussi à synthétiser des MOF de calcium et de magnésium. Dans le cas du calcium, nous avons synthétisé des MOF avec les ligands H4L2, H4L3 et H4L4. Ils ont été nommés respectivement SUM-302, SUM-303 et SUM-304. Comme dans les MOF de nickel, tous les MOF étaient isostructuraux. Malgré l'obtention de cristaux macroscopiquement bien formés, l'analyse par diffraction sur monocristaux ne nous a pas permis en général de résoudre correctement ces structures. Cependant, à partir d'une structure monocristalline, nous pouvons observer que le ligand et le calcium sont connectés.

Dans le cas du magnésium, nous avons obtenu des MOF uniquement avec les ligands H4L1 (le ligand ayant été synthétisé avant nous) et H4L3. Contrairement aux MOF précédents, ils n'étaient pas isostructuraux. Les deux ont été obtenus sous forme de monocristaux et caractérisés. Dans le cas de Mg@H4L1 ou SUM-401, les résultats d'analyse RX sur monocristal ne sont pas d'une qualité suffisante pour être publiables en l'état, mais nous avons cependant quelques informations importantes sur la structure. Nous avons également mis en évidence une nouvelle caractéristique intéressante dans ce cas puisque le DMF est coordonné de manière relativement stable avec des ions métalliques dans le cas de Mg@H4L3 (SUM-403). Dans la figure 6, la vue depuis l'axe b a été donnée pour les deux MOF. Pour une meilleure visualisation des pores, les chaîneslatérales ont été effacées.

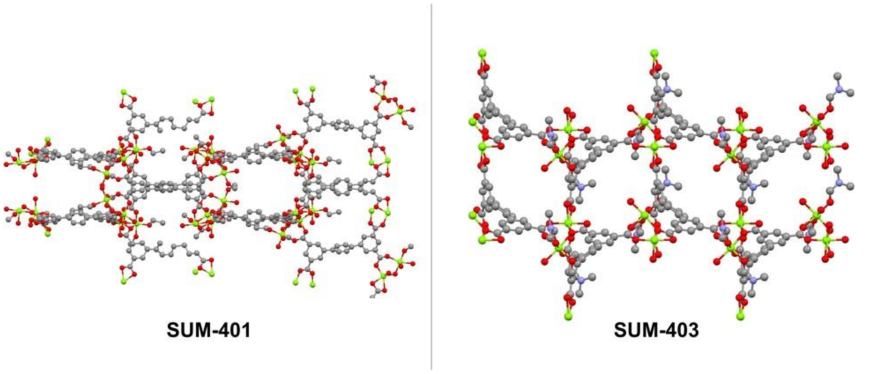

Figure 6. MOF de Mg vue selon l'axe b. Les groupes latéraux ont été éliminés pour une meilleure visualisation.

Des MOF de zinc avec la série H4L ont également été obtenus. Leur structure est identique à celle des MOF au cuivre et mais leurs stabilités réduites nous ont conduit à ne pas poursuivre leurs études.

L'application réussie de ligands tétracarboxyliques avec des fragments de glyme nous a inspiré pour synthétiser leurs homologues dicarboxyliques. De plus, nous avons considérablement simplifié la procédure de synthèse de ces ligands. À partir des 5-6 étapes décrites usuellement avec 2 ou 3 étapes de purification sur colonne, nous avons modifié la synthèse en la réduisant à 3-4 étapes sans nécessité de recours à une purification sur colonne, coûteuse en temps comme en produit.

Pour les ligands de la série H2L, nous avons obtenu quelques MOF. Par exemple, le MOF au zinc du ligand H2L3. La chose intéressante avec ce MOF est qu'il n'est pas isostructural à MOF-5. Ici, la moitié des SBU n'est pas une roue à aubes mais un cluster trinucléaire de zinc.

Nous avons également obtenu un premier MOF à ligands mixtes où deux ligands différents sont associés au même centre métallique. Les éléments constitutifs de ce MOF sont la roue à aubes en zinc, le ligand H2L2 et la 4,4-bipyridine.

Les MOF au zirconium sont généralement peu toxiques et très stables ce qui permet une utilisation dans de larges domaines d'application. Nous avons donc synthétisé à partir du ligand H2L2 un MOF au zirconium L'analyse par diffraction sur monocristaux a permis d'observer qu'il est isostructural à la série UiO et de déterminer les paramètres de maille. Enfin, deux nouveaux ligands tétracarboxyliques ont été synthétisé dans le but de modifier l'environnement de coordination des ligands de type NOTT en ajoutant des groupes méthoxy (H4LOMe) et des fonctions phénols (H4LOH) entre les deux fonctions acides de chaque extrémité. Ils sont représentés sur la figure 3.

Avec les deux ligands, des MOF de cuivre ont été synthétisés. Comme attendu, leurs structures sont complètement différentes de celle de la famille des NOTT. Dans le cas du ligand « méthoxy », l'environnement du cuivre dans la structure est conservé (SBU : roue à aubes SBU) mais la topologie du réseau est différente. Dans le cas du ligand des fonctions phénols nous avons obtenu un nouveau MOF à ligands mixtes, la molécule de pyridine (solvant) étant coordonnée au cuivre.

Nos MOF ont été testés dans différentes applications. L'étude de l'adsorption des colorants est reportée dans notre première publication [12]. La stabilité de SUM-102 et SUM-103 dans l'eau nous a permis de les tester pour l'extraction en solution aqueuse.

Ces matériaux ont adsorbé deux colorants, le bleu de méthylène (cationique) et le jaune d'alizarine R (anionique), le rôle des interactions supramoléculaires lié aux chaînes latérales étant en cours d'étude. La capacité d'adsorption de colorant des deux MOF a été évaluée. Dans le cas du SUM-103, des études d'adsorption isotherme et cinétique ont été réalisées. Les paramètres d'adsorption ont été déterminés dans l'eau (pH neutre) à 30 °C (pour l'isotherme). Une adsorption maximale de Langmuir 194 ± 4 mg g^{-1} a été déterminée.

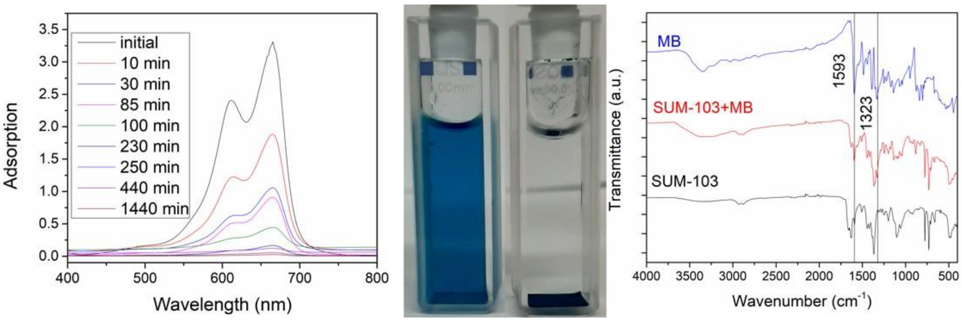

Figure 7. (De gauche à droite, SUM-103) Cinétique d'adsorption, 2.5 mL, 15 mg L^{-1} de solution MB après 24 h à température ambiante, comparaison FT-IR avant et après adsorption.

Une seconde application intéressante de nos MOF, en particulier pour la série H4L3, est leur forte capacité d'adsorption de CO_2. Dans une première expérience, nous avons synthétisé NOTT-101 (Cu@H4L), UTSA-90 (Cu@H4L1), SUM-102 (Cu@H4L2) et SUM-103 (Cu@H4L3) et mesuré leur adsorption de CO_2. Pour pouvoir comparer ces nouveaux MOF aux travaux précédemment décrits, le NOTT-101 qui ne possède pas de chaines latérales, nous a servi de composé de référence. Nous avons observé pour l'échantillon synthétisé, une adsorption de 18 mmol g^{-1} à 0°C et à 10 atm, ce qui était plus élevé que les résultats publiés précédemment pour ce MOF. Nous avons attribué cet écart à un effet de taille, nos cristaux étant significativement plus petits que ceux de l'étude de référence. Nous avons étudié cet effet de taille sur nos nouveaux MOF et constaté une augmentation d'environ 30 à 40 % de l'absorption de CO_2 dans la gamme de taille de 10-15 µm à 1-5 µm, avec un effet plus marquant pour SUM-103, pour lequel l'augmentation est presque triplée de 12 à 38,5 mmol g^{-1}, cette dernière valeur le situant comme un « record mondial » dans sa catégorie pour l'adsorption CO_2. Nous observons cependant une « taille critique », une diminution ultérieure de la taille des cristaux n'augmente plus en effet à partir de ce seuil la valeur de l'adsorption. Nous relevons donc une absorption élevée de CO_2 (au moins 14 mmol g^{-1}) avec tous les MOF composés du ligand H4L3, et ce indépendamment de la topologie ou du centre métallique (cuivre, zinc, calcium, magnésium, lithium).

Le rôle particulier des interactions supramoléculaires avec les molécules de CO_2 est un point à approfondir, des études physicochimiques complémentaires ainsi que des approches de modélisation sont envisagées prochainement.

L'étude du rôle des chaînes latérales a été poursuivie en synthétisant et l'homologue supérieur de la série (SUM-104) où le triglyme se substitue au diglyme. L'adsorption de CO_2 est inférieure à celle du SUM-103, mais reste cependant très élevée autour de 20 mmol g^{-1}. Lors de la mesure de la surface BET avec des gaz inertes tels que l'azote et l'argon, nous avons observé un phénomène intéressant, ce MOF commence à adsorber ces gaz inertes. Cette première observation fera l'objet d'investigations ultérieures.

L'intérêt applicatif de ces matériaux nous a conduit au dépôt d'un Brevet Européen avec l'aide de la SATT-Conectus.

Une autre partie de mon doctorat consistait à synthétiser des matériaux hybrides à macro-, méso- et microporosités. Nous n'avons malheureusement pas pu avoir accès à un support macroporeux adapté pour mener cette étude. Pour la mésoporosité, nous avons sélectionné la silice SBA-15, qui a des pores hexagonaux de 10-15 nm. Nous avons réussi à synthétiser les hybrides SUM (102-103)@SBA-15. Les analyses BET et TEM montrent directement ou indirectement l'incorporation de MOF à l'intérieur de la silice. Dans les mesures BET, nous observons deux types de schémas d'adsorption, l'un lié à la micro et l'autre à la mésoporosité. En outre, le calcul des tailles de pores montre deux types de pores, l'un avec un diamètre de 0,9 nm et un autre de 10 nm, ce qui correspond exactement aux tailles initiales des MOF et du « support » SBA-15. Dans les images TEM (cartographie élémentaire), nous pouvons observer directement la présence des MOF au cœur des cristallites de SBA-15.

L'étude de l'adsorption de CO_2 de SUM-103@SBA-15 a également été réalisée et montre une adsorption de près de 14 mmol g^{-1}, valeur est très cohérente avec un phénomène d'adsorption sur la partie MOF de ce matériau hybride, la taille des pores du SBA-15 étant beaucoup plus grande que le diamètre cinétique des molécules de CO_2.

L'adsorption de formaldéhyde a également fait l'objet d'une étude, reportée dans notre article récemment soumis. Nous montrons à cette occasion la forte adsorption de formaldéhyde sur le MOF SUM-102 qui a une capacité d'adsorption volumétrique de 1007g m^{-3}. C'est près de deux fois plus que HKUST-1, l'un des MOF de référence pour l'adsorption du formaldéhyde.

Conclusion

A la suite de la thèse, 1 article a été publié, 1 article est soumis, 1 brevet a été déposé, 2 articles de conférence et 1 présentation d'affiche ont été présentés. 9 nouveaux ligands et avec ces ligands, des dizaines de nouveaux MOF ont été synthétiséset caractérisés. Ils ont été utilisés dans un large domaine d'applications, comme l'adsorption de COV (Composés Organiques Volatils, dans notre cas le formaldéhyde), l'adsorption de colorants anioniques et cationiques en milieu aqueux et l'adsorption de CO_2. De plus, pour des raisons de confidentialité, nous ne pouvons pas, pour l'instant, publier toutes les applications étudiées. Aujourd'hui, avec l'aide de la SATT-Conectus, nous poursuivons les discussions avec un partenaire industriel local sur des applications complètement différentes de nos MOF.

A travers nos travaux, nous avons prouvé l'efficacité de la modification de ligands avec des chaînes latérales de type glyme. D'un côté, ils ont augmenté la stabilité dans l'eau, les analogues précédemment décrits sans chaînes latérales n'était pas stables dans l'eau. D'un autre côté, les chaînes latérales riches en oxygène ont considérablement modifié l'interaction hôte-invité, à la fois à l'intérieur de la cavité des MOF comme probablement sur la surface externe des microcristaux. Nous avons observé une adsorption de colorants, dont la taille était supérieure à la taille des pores du MOF et une adsorption forte de CO_2 que nous avons commencé à étudier mais pour laquelle nous ne sommes pas en mesurepour l'instant d'expliquer le mécanisme exact d'une telle adsorption de CO_2. La présence des chaînes latérales joue un rôle sans doute clé dans tous ces phénomènes d'adsorption. Aussi, nous avons également synthétisé de nouveaux matériaux hybrides avec de la silice mésoporeuse. L'incorporation de MOF dans la silice (SBA-15) a été prouvée par plusieurs techniques différentes.

Comme mentionné précédemment, nous sommes en discussion avec un partenaireindustriel. Ce travail sera donc poursuivi dans le cadre du programme de prématuration de la SATT-Conectus sous la forme d'un post-doc.

Références

1) S.M. Moosavi, A. Nandy, K.M. Jablonka, D. Ongari, J.P. Janet, P.G. Boyd, Y. Lee, B. Smit, H.J. Kulik, *Nat Commun*, 2020, **11**, 4068.

2) F. Cui, Q. Deng, L. Sun, *RSC Adv.*, 2015, **5**, 98215-98221.

3) M. J. Wyart, *Bulletin de Minéralogie*,1926, **49-7-8**, 148-159.

4) G. Wilkinson, M. Rosenblum, M.C. Whiting, R.B. Woodward, *J. Am. Chem. Soc.*, 1952, **74, 8**, 2125–2126.

5) V.W. Day, M.F. Fredrich, W.G. Klemperer, R.S. Liu, R., *J. Am. Chem. Soc.*, 1979, **101, 2**, 491–492.

6) B.F. Hoskins, R. Robson, *J. Am. Chem. Soc.*, 1990, **112, 4**, 1546–1554.

7) O.M. Yaghi, G. Li, H. Li, *Nature*, 1995, **378**, 703–706.

8) S. Kawata, S. Kitagawa, H. Machida, T. Nakamoto, M. Kondo, M, Katada, K. Kikuchi, I. Ikemoto, *Inorganica Chimica Acta*, 1995, **229**, 211-219.

9) M. Riou-Cavellec, C. Albinet, J.M. Grenècheb, G. Férey, *J. Mater. Chem.*, 2001, **11**,3166–3171.

10) H. Li, M. Eddaoudi, M. O'Keeffe, O.M. Yaghi, *Nature*, 1999, **402**, 276–279.

11) H.-M. Wen, G. Chang, B. Li, R.-B. Lin, T.-L. Hu, W. Zhou and B. Chen, *Crystal Growth & Design*, 2017, **17**, 2172–2177.

12) N. Israfilov, K. Soukup, B. Louis and J.-M. Planeix, *New J. Chem.*, 2022, **46**, 8967–8970.

13) X. Lin, J. Jia, X. Zhao, K. M. Thomas, A. J. Blake, G. S. Walker, N. R. Champness, P. Hubberstey and M. Schröder, *Angew. Chem. Int. Ed.*, 2006, **45**, 7358–7364.

14) T. A. Makal, X. Wang and H.-C. Zhou, *Crystal Growth & Design*, 2013, **13**, 4760 - 4768.

Introduction

I. What is MOF?

MOFs or Metal-Organic Frameworks are subclasses of coordination polymers, composed of two building units, metal ions or clusters and organic linkers named tectons in the molecular tectonics field. Due to the versatility of the coordination mode of metal ions or clusters and the number, spatial distribution and orientation of the coordinating sites of organic ligands, the interactions between these units lead to 0, 1, 2, or 3D structures with various geometry. A simplified version of this is given in figure 1. Millions of MOF structures can be considered and up to today, more than 90.000 MOFs were synthesized [1].

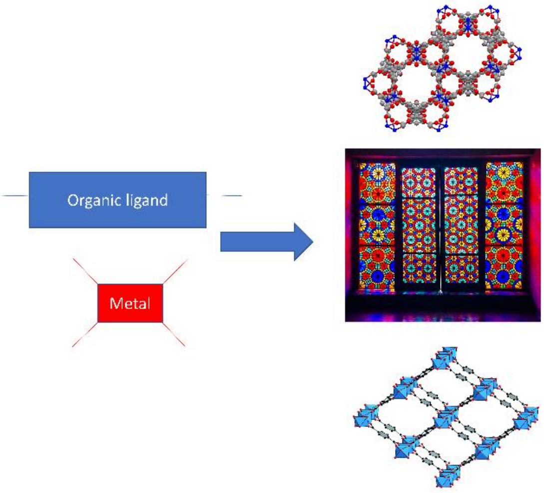

Figure1. Simplified scheme of 3D network formation.

If we create an evolutional chart of MOF (fig. 2), it began from the works of Alfred Werner by identifying and studying coordination bonds. The differentiation of coordination bonds from covalent ones allowed for a better understanding of the inorganic chemistry as structures and properties of numerous complexes and pushed its further development. From the 18th century, Prussian blue, composed of iron and cyanide ions, was known and described as coordination polymers. Even today Prussian blue and its analogs are widely used from catalysis, and gas storage to molecular magnets [3,4,5]. From that time different coordination and organometallic compounds were synthesized, such as basic zinc acetate [6], ferrocene [7], polyoxometalates [8], etc… All of this experimental and theoretical information was the basis for using coordination chemistry to develop new methods of making materials whose properties could be selected from their molecular constituents. In the 1990s, several groups designed, obtained and characterized crystalline solids from metal salts and organic ligands chosen or designed to self-assemble into solid state coordination polymers. [9].

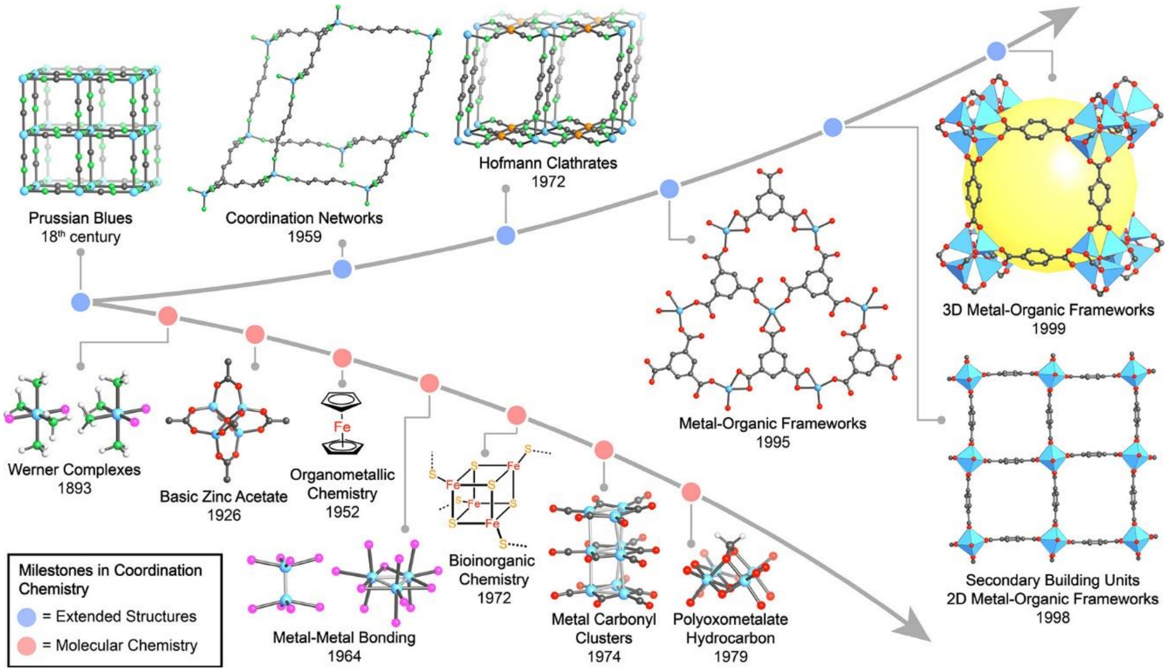

Figure 2. Evolution of coordination polymers [2].

The first scientific approach to creating synthetic 3D coordination polymers was pioneered by R. Robson and B.F. Hoskins in the 1990s [10]. They synthesized copper and zinc coordination polymers. The resulted coordination polymers had adamantane and iceane-like cavities. Upon removal of the solvents, these coordination polymers loosed their properties. Besides, they predicted the possible future improvements and applications of these materials. Below one of the interesting conclusions is given from their original paper:

"Despite Nature's abhorrence of a vacuum it may be possible to devise rods with sufficient rigidity to support the existence of solids with relatively huge empty cavities. Materials combining good or even high thermal, chemical, and mechanical stability with unusually low density may thereby be afforded"

Beginning in the mid-90, to obtain new porous solids, many teams embarked on the synthesis of a new class of materials called MOFs for the first time, the "framework" term being the subject of rich and lively discussions between solid state or materials chemists. O. Yaghi [11], S. Kitagawa [12], and G. Férey [13] showed that it was possible to obtain MOFs having a high surface area, sometimes exceeding well-known adsorbents such as zeolites, activated carbon, etc… First "MOF" was synthesized by Yaghi using Co^{2+} and trimesic acid in 1995 [11]. The composition of the obtained solid show that two pyridine and one trimesic molecule are coordinated to Cobalt into 2 dimensional coordination polymer, π-π stacking between pyridine moieties gives a 3D framework that is stable upon solvent removal and also up to 300°C. (fig. 3A) Later in 1999 Yaghi *et al.* synthetized the 3D MOF which consisted only of coordination bonds and had a huge surface area- MOF-5 [14] (fig. 3B). Even today it's one of the benchmark MOFs. As mentioned before construction units of the MOFs are organic ligand and metal ions (or clusters). In MOF terminology the latter is called SBU-Secondary Building Unit. The SBU of the MOF-5 composed from cluster of [ZnO4] and the organic ligand is the terephthalic acid. In general, Zinc and Copper are some of the commonly used metals in MOF synthesis. As usual, they gave paddlewheel SBU, but they can give also other structural types of SBUs [15].

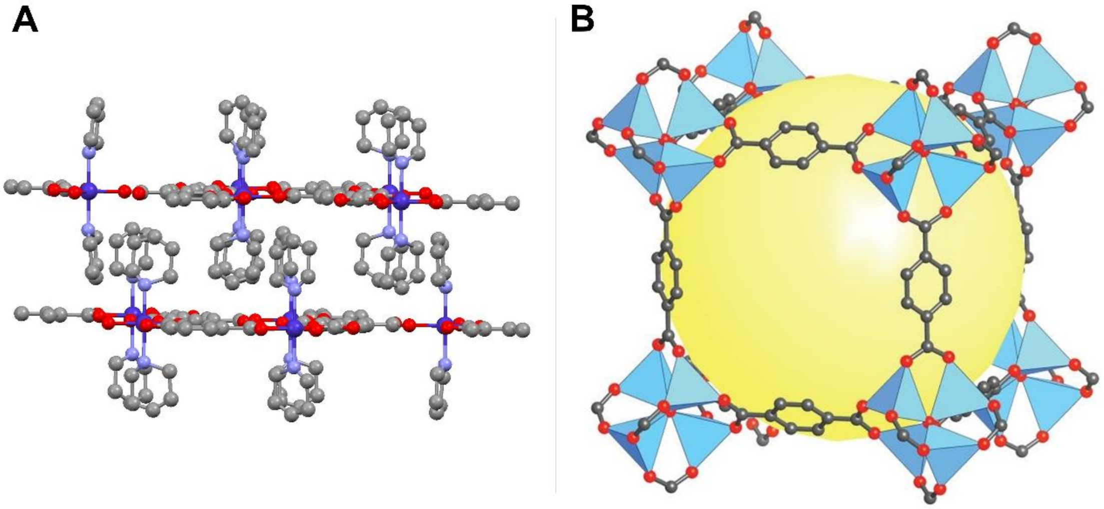

Figure 3. A- 2D Cobalt MOF; B- 3D Zinc MOF (MOF-5).

During the mid-90s and by the end of millennia, other groups also began to develop MOFs. In France, the pioneer of this domain was Gerard Férey, Christian Serres et *al.* from Versailles Saint-Quentin University. Their results also opened a new pathway in MOF synthesis. Also, most MIL (Materials Institut Lavoisier) series MOFs are stable in the aqueous environment [16]. The main reason for their stability is based on their SBUs. Fe and Cr ions create a cluster with oxygen atoms, which stabilizes these MOFs.

However, the first three-dimensional coordination compounds of Férey's group were reported as early as 1992-93 when he worked at the University of Maine (currently Le Mans). [13]. The compound was called ULM-5 and was obtained by heating the mixture of the Ga_2O, P_2O_5, HF, and 1,6-diaminohexane in an aqueous solution. In this pioneering work, the ligand used was a flexible one, 1,6-diaminohexane as a ditopic organic ligand.

The first work of the Férey group which employed "modern ligands" (rigid) was the hydrothermal synthesis of Fe@BTC (1,3,5-benzene tricarboxylic acid or trimesic acid). As Férey mentioned in his paper "However, it seems that rigid species lead to more original open structures". The heating of Fe(II) with trimesic acid in an aqueous medium yielded to 2 crystalline materials [17].

Later, Férey *et al.* synthesized lots of new interesting, stable structures, especially with iron and aluminum which have applications in several domains: from adsorption to drug delivery. Some examples are MIL-53 and MIL-126 [18, 19] (fig. 4). The metal centers could be Iron, Aluminium, or Chromium.

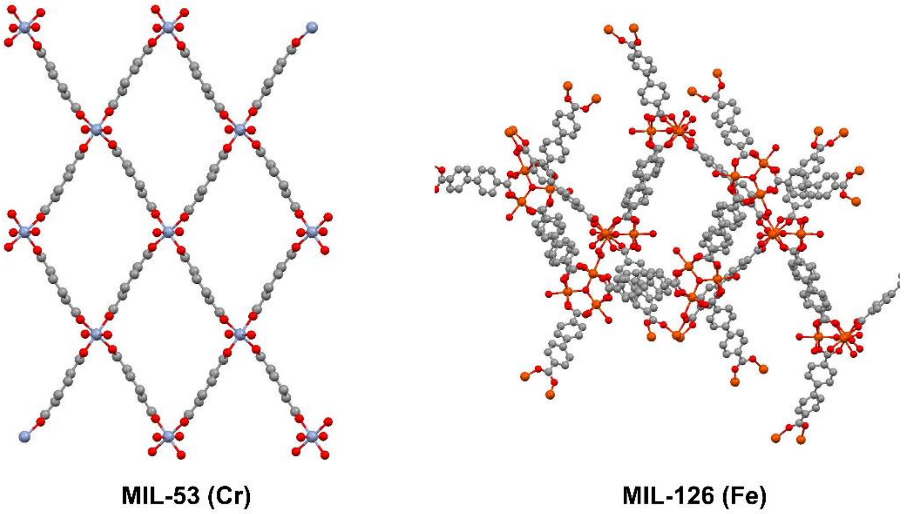

Figure 4. MIL-53 (Cr) and MIL-126 (Fe). View from b axis.

We began our thesis with the evolution of the coordination compounds to the MOFs. However, from the point of view of porosity and applications, we can compare the MOFs to the zeolites. and MOF can behave like zeolite, but zeolite cannot behave like MOF.

To deepen this comparison, it is first useful to recall the main characteristics and interests of zeolites. In 1756, the Swede Axel Fredrick Crönstedt made a curious discovery. He directs the flame of his blowtorch on a piece of stilbite, a natural mineral, when, at around 150°C, the stone is covered with bubbles as if it were starting to boil.

Two years later, he created in his Mineralogy System a separate order for these minerals with unique properties: Zeolites, zein: “boil” and lithos: “stone”.

He then had no idea that his obscure discovery would give birth to a family of materials, porous solids, which, two and a half centuries later, played a strategic economic role. Some sources do not hesitate to affirm that what was only a laboratory curiosity would contribute through its applications, directly or indirectly, to 25% of the gross national product of the major industrialized countries!

The zeolites are microporous, mainly naturally occurring aluminosilicate materials (fig. 5).

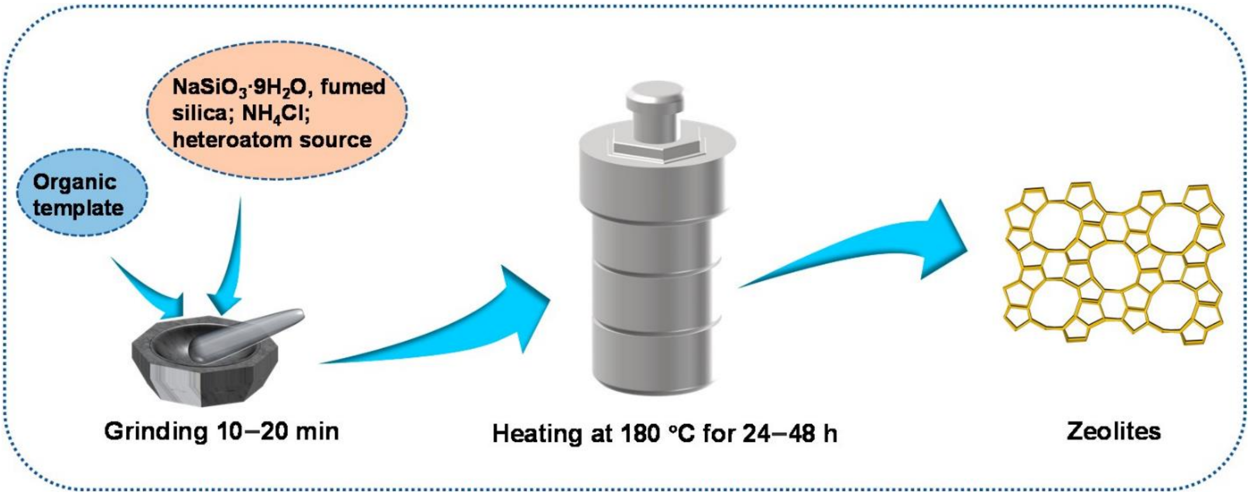

Figure 5. Example of Zeolite synthesis.

They have a general formula $M_xAl_xSi_{1-x}O_2·yH_2O$, where M could be a metal ion or a proton. As mentioned above zeolites are used a lot in industrial processes as adsorbents or catalyzers.

If we now focus on MOFs, the first simple question concerns the value of studying them. Why today synthesize new MOFs? Indeed zeolites are cheaper, more stable under humidity conditions, and thermostable. We can also synthesize today zeolites with hierarchical pores. First of all, the MOFs and zeolites don’t have the same degree of maturity. From the history described above, we know that the beginning of the MOFs is considered the mid-90s. However, the first zeolite was discovered in 1756. That’s why within time most probably MOFs will develop. Already from the last 20-25 years, we know that there are a lot of developments in the field of MOFs studies. In figure 6 we can see MOF papers that were published from 2007 to 2021. Moreover, more and more start-ups with MOFs are appearing with solutions in different fields.

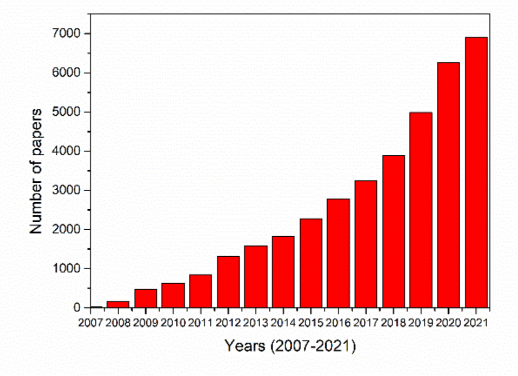

Figure 6. The number of MOF papers. The keyword "Metal-Organic Framework" was used for the search.

The most important advantage of MOFs is the possibility of precisely tuning the size of the pores and modifying the nature of the tectons, which will lead to rationally designed porous materials, which is nearly impossible to do with zeolites. The modification of the nature of the zeolites is very limited, one of the possibilities is cation exchange. The ability to tailor the structure and properties of these materials through the choice of their structural units is undoubtedly an important advantage over zeolites. On the negative side, many MOFs are more difficult to obtain than zeolites without the solvents and by-products of synthesis.

II. The application of MOFs

Due to their tunable pore size and nature, MOFs have potential application in wide areas (fig. 7). As the MOFs were the analogs of the zeolites the first application was mainly based on adsorption (especially gas phase), which is even today stays as one of the main domains of application. Although we are talking about the application of MOFs, it should be noted that nowadays MOFs are not used in industry. Despite their outstanding performances, the price of the MOFs and also the sometimes stability poses problems for widescale application. Therefore, one of the promising uses of the MOFs is their capacity to adsorb gases, such as CH_4, H_2, CO_2, and also toxic gases such as NO_X, SO_X, H_2S, and VOC (volatile organic compounds) [20,21]. Among these gases, CO_2 is attracted considerable attention. As it is well known CO_2 emissions increased dramatically since the industrial revolution from 280 to nearly 400 ppm. As our planet is a fragile system, increasing carbon dioxide concentration creates huge problems such as acidification of oceans, an increase in global temperature, etc…

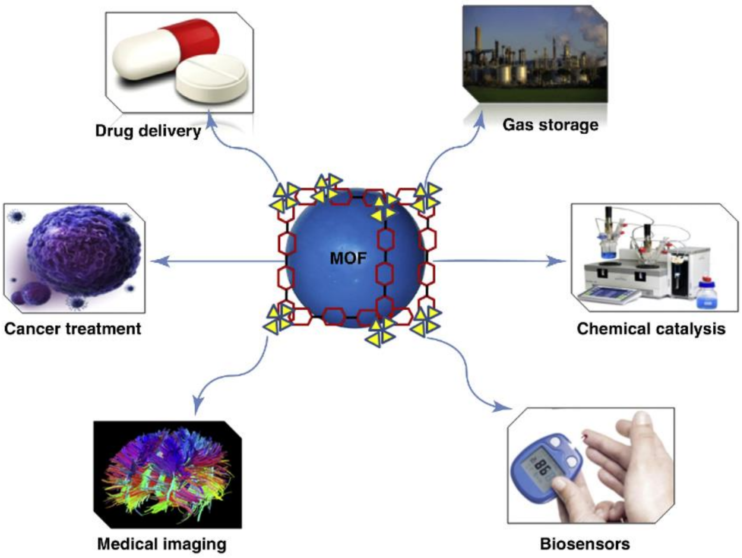

Figure 7. The fields of application of MOFs.

Thus, there is a primordial necessity to decrease this pollution. CO_2 adsorption by MOFs could be realized as a direct capture from the air (DAC) or capture from CO_2-rich sources (power plants, cement plants, etc.). In general, these capture processes are categorized under CCS (Carbon Capture and Storage) technologies.

Currently, there is not any DAC of CO_2. In industry, carbon dioxide is captured by liquid amines, mainly MEA (monoethanolamine) based liquids. They have high binding energy, therefore their desorption demands high energy. As the direct air capture demands high binding affinity, in general for this purpose MOFs are modified with amine groups, either pre or post-synthetically. One example is the modified MOF-74 analogs [22]. MOF-74 itself is one of the best MOFs for CO_2 capture. The building units of the MOF-74 in this study are 4,4′-dioxido-3,3′-biphenyldicarboxylate as a ligand and Mg^{2+} or Zn^{2+} ions as a metal center. Later, the Mg-MOF was post-synthetically modified with N,N′-dimethylethylenediamine (fig. 8). Final MOF showed 2.0 mmol/g (8.1 wt %) at 0.39 mbar and 25 °C, conditions similar to the removal of CO_2 from the air, and 3.14 mmol/g (12.1 wt %) at 0.15 bar and 40 °C, conditions comparable capture from flue gas.

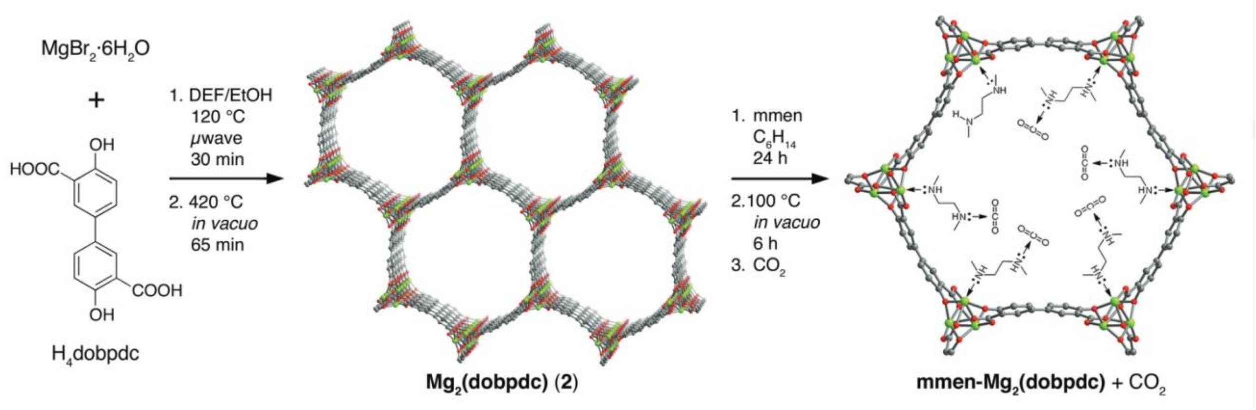

Figure 8. Synthesis of Mg@dobpdc grafted with DEA. [22]

The design of MOFs for pure or rich CO_2 adsorption is a little bit different from than DAC design. In this case, the major rule is to have as much as possible surface area. In table 1, you can see some high surface area MOFs and their CO_2 adsorptions under given conditions.

Table 1. High surface area MOFs and their CO_2 adsorptions.

MOF	BET surface area (m^2/g)	Temperature (K)	Pressure (bar)	CO_2 uptake (mmol/g)
MOF-177 [23]	4500	298	35	33.50
NU-100 [24]	6143	298	40	46.40
MOF-210 [25]	6240	298	50	16.86

Despite high surface area and functional groups, there are other important factors in CO_2 adsorption such as available Open Metal Sites (OMS). In the literature, there is also another name for these sites: Coordinatively Unsaturated Sites (CUS) or Open Coordination Sites (OCS). As can be seen from the name, the coordination sites are unsaturated and that can influence the adsorption characteristics of the MOFs. They can increase adsorption by strong interaction, also they can have catalytic activity [26]. Even in nature most enzymes and metalloproteins contain OMS. An example is the iron ion in hemoglobin, which is fivefold coordinated before the dioxygen coordination.

One of the most used SBU in MOF chemistry is the copper paddlewheel, where two water molecules coordinated to copper in an axial position. During the activation process, those molecules are removed, which creates an OMS. Activation is a widely used term in this field. It means the elimination of solvent (water) guest molecules from the network by the means of vacuum and/or temperature. In general, before the measurements (especially adsorption) the activation process is applied.

The most famous MOF with this SBU is the HKUST-1. HKUST stands for Hong Kong University of Science and Technology. The building blocks of this MOF are copper paddlewheel and trimesic acid. Despite the small ligand size, the unique topology gives this MOF a high porosity with up to 14 Å diameter pores. Wu *et al.* [27] showed that, at low pressure and low temperature (20K), CO_2 binds only to metal centers at a 1:1 CO_2:Cu ratio.

While on the subject, one of our best performing MOFs for CO_2 adsorption is based on a copper paddlewheel unit.

As we know, metal-organic frameworks are porous solids. Another use of these pores is their application for the adsorption of contaminants [28,29,30]. It is especially important to make a decontamination process in an aqueous environment. Therefore, MOFs should be stable in water. Despite a tremendous amount of MOFs, only a few parts of them are stable in water and widely used, such as most MIL series, UiO series (Zr-based MOFs), etc… It is worth underlining that some of our MOFs showed high stability in water.

Again, there are much cheaper adsorbents than MOFs, however, the possibility of the modification of the pores (via various ways) allows for to design of more specific materials. Which is needed to adsorb the various types of contaminants: pesticides/herbicides, dyes, radioactive ions, detergents, etc… Here is an example, we will discuss dye adsorption. As it is well known one of the big consumers of dyes is the textile industry and with the new consuming habits like “fast fashion” the use of the dyes increase dramatically [31]. This industry is responsible for nearly 10% of global greenhouse gas emissions. Therefore, there is tremendous importance to clean the dyes from the water. We will discuss only the adsorption of dyes, however, it is worth noting that there are also other ways to clean the dyes, such as photodegradation [31], oxidation [32], flocculation [33], filtration [34], etc.

As mentioned before, MOFs are designed rationally to adsorb one or another compound. Hence, there are plenty of MOFs for the adsorption of plenty of things. Therefore, we will talk here about only one example, MIL-101(Al), the well-known MOF. It is based on the self-assembly of terephthalic acid and Al^{3+}. The amine-modified version of this MOF was used for the adsorption of 2 types of dyes: Methylene blue (cationic) and methyl orange (anionic)[35]. Logically, grafting electron-rich amine group should increase the adsorption of cationic dye and this is observed in experiments. As a result, at 30°C in an aqueous environment, the maximum Langmuir adsorption for methylene blue is 762 ± 12 mg/g and for methyl orange 188 ± 9 mg/g was observed. For example, for non-amine modified MOF, the MB adsorption was 195 mg/g.

III. Importance of the new MOF synthesis

Despite a huge amount of existing MOFs, there are only a few series that have potential applications. Therefore, this huge number of MOFs is not a reason to stop looking for new MOFs. One of the main reasons for the non-applicability of MOFs is their reactivity to solvolysis of complexes in different solvents, especially in water and also their non-stability after activation. Activation is the elimination of solvent molecules from the pores via the help of temperature and/or pressure swing. A lot of MOFs, such as NOTT-101 [36] are destroyed in contact with air after activation, because of the humidity of the air. Another limitation of the appliance of MOFs is the use of toxic metals as SBU. Thus, metals that are biocompatible and less expensive like Ca^{2+}, and Mg^{2+} should be privileged. Also, to answer to stability challenge, high valence metal ions such as Zr^{4+}, and Fe^{3+} could be used as an alternative. Especially, Zr^{4+} attracts much attention of its very stable nature and low toxicity. Just to imagine, UiO-66 (fig. 9) based on $Zr_6O_4(OH)_4^{12+}$ SBU and terephthalic acid is stable in pure (37%) hydrochloric acid and up to pH 12 [37]. But the choice of metal is not the only thing that influences stability.

Another important factor that should be given attention in the MOF synthesis is the right choice of the ligand to design optimal topology. In this way, the number of coordination sites and the distance between two opposite coordination sites of SBU or organic ligand are key factors to analyse the MOFs structure and internal porous volumes.

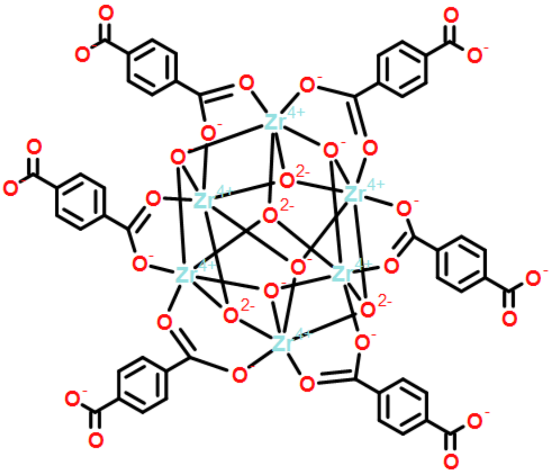

Figure 9. Building blocks of UiO-66 and their connection.

As an example of the importance of the topology, we can compare two well-known MOFs: one hand NOTT-101 and the other HKUST-1. In both MOFs, the SBU is the copper atoms in the paddlewheel configuration. For NOTT-101 the size of the terphenyl ligand is much higher than those of benzene tricarboxylic acid (BTC) for HKUST-1. Related size of SBU compared to Cu ion shows that size of this second building block is in inverted order and analysis of properties reported in the literature shows us that NOTT-101 and HKUST-1 have the nearly same surface area and pore sizes (fig. 10).

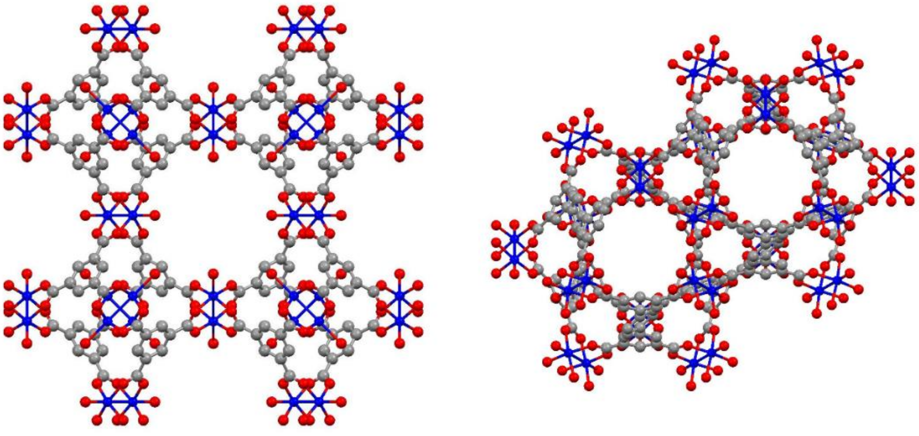

HKUST-1

NOTT-101

Figure 10. The porosity of HKUST-1 and NOTT-101. View from c axis.

There exists another way to synthesize stable MOFs based on the "hard and soft acids and bases" theory. According which hard acids like Zr^{4+} will create stable MOFs with hard bases like carboxylates and vice-versa, soft acids like Zn^{2+} will make stable MOFs with soft bases like imidazole. The best example of these “soft acid-soft base” MOFs are ZIFs or Zeolitic Imidazolate Frameworks. The reason for such nomenclature lies in their isomorph structure with zeolites. The most known member of the ZIF family is ZIF-8 (fig. 11).

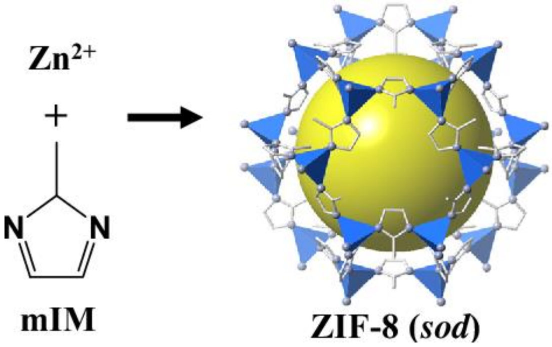

Figure 11. ZIF-8.

Another interesting approach is to modify the existing ligands. In the work of Zhou *et al.* [38], the same ligand for NOTT-101 was used as a departing ligand and it is modified with different length alkoxy chains. With the increasing size of chains, the stability of the MOFs against humidity was also increased. This is explained by the hydrophobic nature of the MOFs (fig. 12).

The long chains were hydrophobic and repelled water molecules. However, in our work [39] we obtained stability, not with hydrophilic, but amphiphilic side chains.

There are also, some less known and less used techniques to obtain stable MOFs. For example, PCN-921 which is Zinc based on MOF transformed to PCN-922 which is Copper-based MOF via simple metal exchange [40].

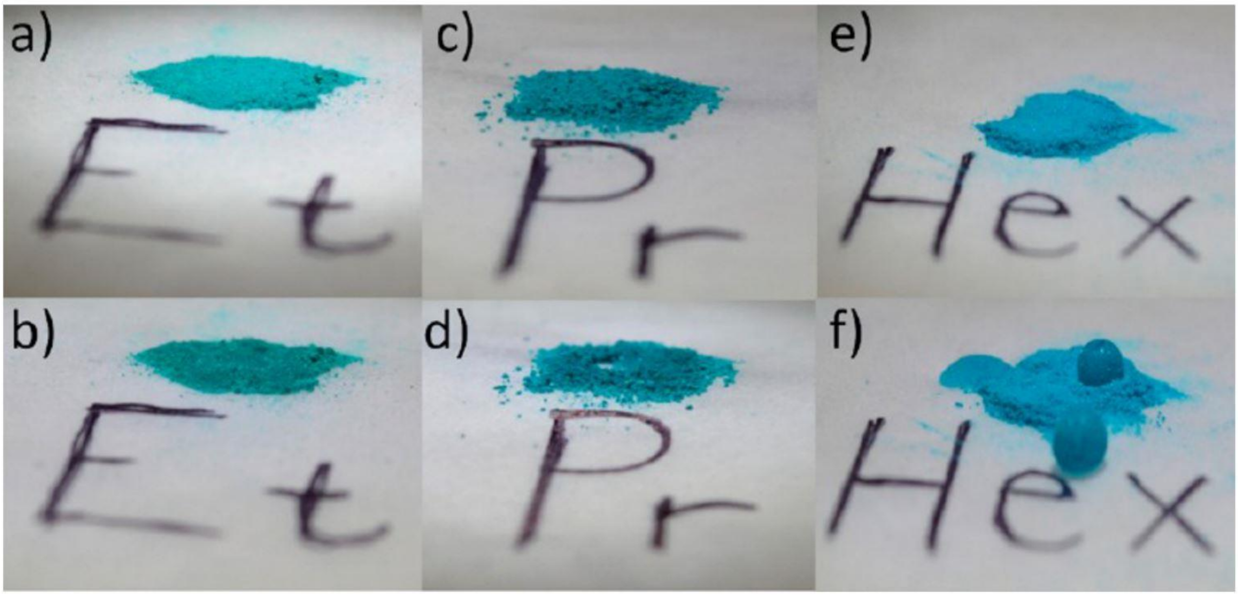

Figure 12. Dry (a, c, e) and wet (b, d, f) powder samples of Cu2TPTCOEt, −OnPr, and −OnHex, respectively. After additions of a single drop of water the −OEt and −OnPr frameworks readily absorb the water drop, while the −OnHex framework acts as a superhydrophobic surface [38].

IV. The reason for choosing tetracarboxylic ligands

We can theoretically classify the ligands synthesized in this work into 3 classes: tetracarboxylic, dicarboxylic, and "others".

Firstly, we begin with the synthesis of tetracarboxylic ligand. Seeking to obtain stable and chemically inert MOFs in water, we chose tetratopic systems which are also compounds resistant to many of the conditions in which conventional MOFs degrade in the air or the presence of moisture. Because our laboratory had an experience in the synthesis of these types of ligands. Chiral functionalized TPTC(Terphenyl tetracarboxylic) ligand based MOF was synthesized by Hosseini *et al.*[41]. In their study, two homochiral porous coordination polymers (copper MOFs) were prepared, combining porosity and chirality. Their gas sorption properties and enantioselective adsorption of tryptophan in the solid state were also studied which demonstrated well chiral separation for (L) and (D) tryptophan. This work appears as a proof of concept that interactions of a substrate with suitable functionalized MOFs could be used for supramolecular host-guest recognition.

Another reason for the selection is the optimal combination of porosity/stability. As a rule of thumb, increased porosity decreases the stability.

The simplest version of the TPTC ligand firstly was studied by Schroder *et al.* [36] in 2006 (fig. 10, NOTT-101). They synthesized terphenyl-3,3',5,5'-tetracarboxylic acid, without any functionalization. Moreover, they did this study comparatively with biphenyl and tetraphenyl versions of the ligand. The terphenyl ligand (respective copper MOF) showed a high surface area (2247 m^2 g^{-1}) and its hydrogen adsorption was significantly high (6.06 wt%/20 bar).

Later, these ligands were developed by Zhou *et al.* [38] They added pendant alkoxy groups to the central phenyl ring, such as -OMe, –OEt, -OPr, and –OHex, to increase the water stability of these materials (fig. 12).

In another study, the TPTC ligand was functionalized with pendant -OMe groups [42]. For example, Cu@TPTC-OMe (or UTSA-90) exhibited good CO_2 adsorption properties (214 cm^3 g^{-1}), as well as C_2H_2 (184 cm^3 g^{-1}) when compared to Cu@TPTC (or NOTT-101a) (125 and 83 cm^3 g^{-1}, respectively) despite a lower surface area (at 295K and 1 bar). This highlights the importance of the side-chain "decoration" of MOFs.

Later, as we have seen good results with modified tetracarboxylic ligands, we decided to synthesize dicarboxylic ligands with the same functionalization. As described before, ditopic ligands such as dicarboxylic ligands are the simplest ones to make 3D networks. The famous MOF-5, which we can call the first MOF, was built with terephthalic acid and [ZnO4] SBU. However, the drawback of dicarboxylic systems is their weak stability (not considering high valence metal ions). Especially, with increasing ligand length the stability decreases even more. Therefore, for dicarboxylic ligands, it's more interesting to synthesize MOFs with high valence metal ions. Such as MIL-53 (Cr) prepared by the group of G. Férey [43]. It is worth mentioning that some MIL series MOFs are prepared at 200-300°C in water, which indicates their chemical inertness in water.

Another example of stable MOFs is the Zirconium-based UiO series. In figure 13 the members of this series were with corresponding ligands. As mentioned before, the increasing ligand length decreases the stability, however, UiO-68 (with terphenyl backbone) is still quite stable. At least, it is stable thermally up to 400°C and also stable in water [44,45]. Like, tetracarboxylic ligands in our work we functionalized the terphenyl backbone.

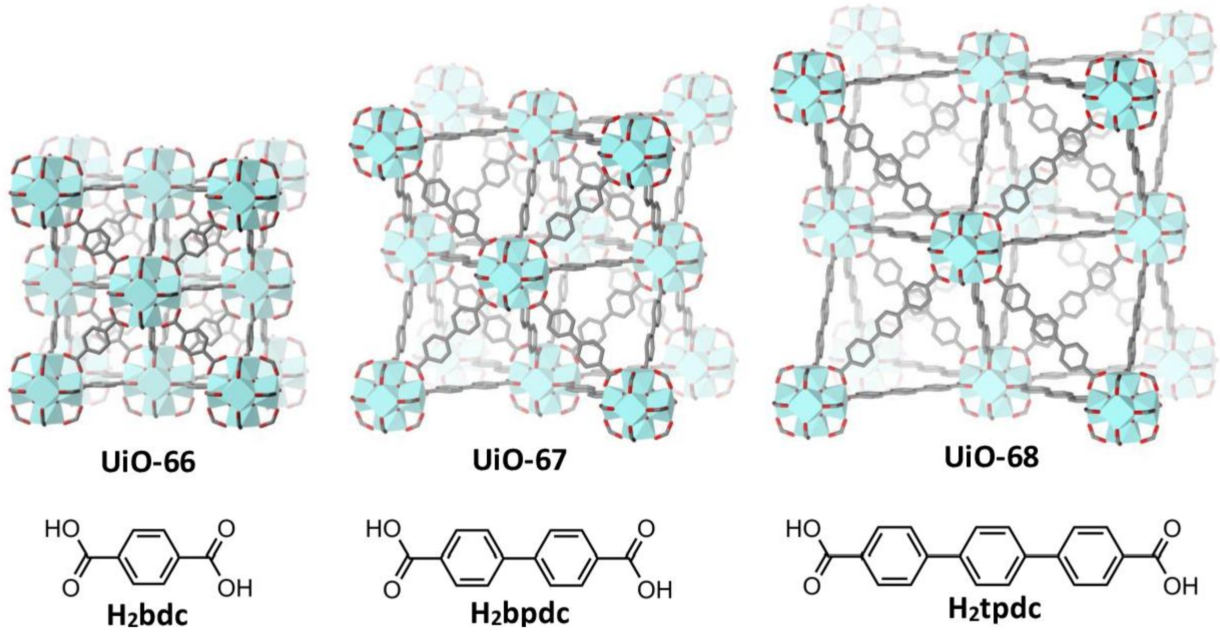

Figure 13. Zirconium-based MOFs: UiO-66, 67, and 68.

Also, during the thesis, a new kind of ligand was synthesized. Unfortunately (or fortunately), there is not any comparable ligand in the literature to compare with them. For their synthesis we used again the terphenyl backbone, however, instead of modifying the middle phenyl ring, we modified the phenyl ring at the sides. We added hydroxy and methoxy groups between acid groups. We will talk about them in detail in chapter III.

V. The reason for choosing glyme chains

Why do we functionalize our ligands, therefore our MOFs? As mentioned earlier [38] one of the methods of the increase of stability is the tuning of the ligand. It could be done in two ways: synthetically or post-synthetically. As is clear from the nomenclature, in the first method ligand was functionalized before the synthesis of the MOF. In the second case, the ligand (in this case as a part of a MOF) was modified after the synthesis of the MOF. Both methods have their advantages and disadvantages. In our case for all the MOFs modification was synthetical.

Except for the ligands from the "new model ligands" (details are given in chapter I), the rest of the ligands were modified with the same groups. We chose the glyme or ethyleneoxy groups for the modification of our ligands. The ligands were tuned with different size groups. The main driving inspiration for choosing this side chain was the works of Cram, Pedersen, and Lehn [46-48]. The oxygen rich cyclic compounds (crown ethers, cryptands) showed the capture of ions with a high binding constant. Supramolecular chemistry was founded by Prof. Jean-Marie Lehn in Strasbourg, this inspiring contribution, its openings and its many significant contributions are opening up and will continue to open up significant advances.

In the same vein, the MOF synthesis method is an application of the more general approach of molecular tectonics. We propose to involve here molecular recognition mechanisms at two levels: firstly as a driving force for the formation of MOFs and secondly to give these porous materials selective recognition properties.

Thus, we decided to choose ethyleneoxy side chains, because those oxygen-rich chains could create a strong host-guest interaction within the cavity of the MOFs. Also, we wanted somehow assemble supramolecular moieties and MOFs into the same platform. So, the MOF adsorbing guest molecule will be a self-assembled structure, that creates self-assembly inside itself. The poly(ethyleneoxy) chains present in both crown ethers and cryptands have also been used to design various “open” versions of these compounds called podands [49](ex. Tripod) displaying good selectivity and phase transfer properties. Their ability to solubilize in water as well as in numerous organic solvents is one of their interesting characteristics.

Also, the importance of side chains bearing oxygens was proved by several other scholars [50-53]. For example, in their work Choi *et al.* [50], added alkoxy chains (only one oxygen atom, the rest are carbons) to terephthalic acid (fig. 14). They prepared MOF (MBCn) as a mixed ligand in the presence of simple terephthalic acid at different ratios. Besides, being isostructural to MOF-5 they showed up to 3 times higher gas sorption and more stability against humidity. Interestingly, the surface areas do not decrease, contrary for some MOF surface area is increased nearly twice. But in the paper, there is no detailed explanation for this phenomenon.

The effectiveness of ethylene glycol groups is not limited only to adsorption. It is also used in a vast domain from catalysis [51] and dye removal [52] to drug delivery [53].
In another work [52], MOF was modified with poly(ethylene glycol) diglycidyl ether (PEGDGE) post synthetically for separation of CO_2. Firstly, NH2-MIL-101 Cr was synthesized. Later, PEGDGE reacted with the amine group of the MOF (fig. 15). Based on modified MOF, Mixed Matrix Membrane (MMM) was prepared. Nowadays, MMM is very popular [55]

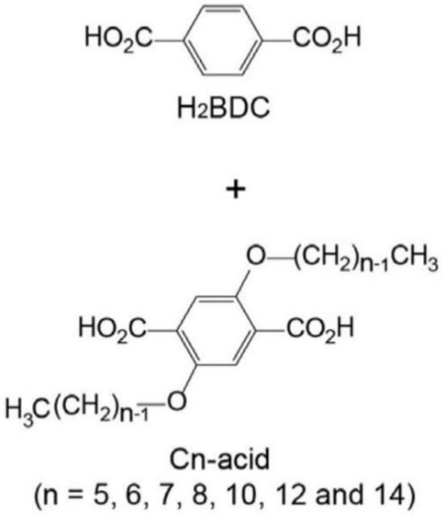

Figure 14. Ligands for preparation MBCn MOFs.

It is a dispersion of inorganic compounds inside the polymer. The most popular polymer for CO_2 separation is polyether block amide (Pebax), which is consisted rigid polyamide chain and a flexible polyether chain.

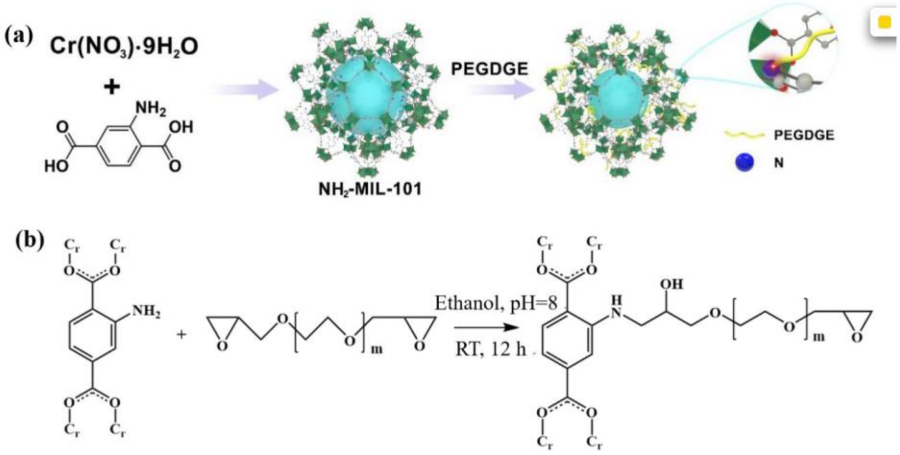

Figure 15. (a) Schematic Diagram of PEGDGE grafting into the Cage of NMIL-101, (b) Molecular Reaction Process between NMIL-101 and PEGDGE [52].

In the study of Forgan *et al.* UiO-66 is post synthetically modified with PEG for drug delivery. Another reason for using the PEG chain in drug-related studies is its biocompatibility [53]. Again, in this work also, PEG contributed to increased stability of the MOF.

High stability given by PEG moieties, allowed the use of MOFs in catalysis. Yang *et al*. [51] used PEG-modified HKUST-1 for the conversion of benzyl alcohol to aldehyde.

MOF was synthesized in the presence of the PEG, and some of the PEG chains were trapped inside the pores, creating a mesoporosity.

But in all preceding works, the modification was post-synthetic. One of the disadvantages of post-synthetic modification is a non-homogenous functionalization. Thus, all of these aforementioned points motivated us to graft similar side chains to the ligand to observe the behavior of those groups inside the pores of MOF and test their potential applications.

VI. Introduction to thesis

This manuscript consists of three parts (chapters) and an experimental part. We will begin chapter I by describing the synthesis and improvement of the ligands. The exact details will be given in the experimental part. Furthermore, the choice of the metal centers also will be discussed in this chapter. Chapter II will be about the synthesis and characterization of MOFs. The applications are given in Chapter III, where different uses of MOFs in different environments, towards different host molecules were analyzed. Especially, with CO_2 adsorption some interesting results were obtained. Later we will finish with a general conclusion.

REFERENCES

1. S. M. Moosavi, A. Nandy, K. M. Jablonka, D. Ongari, J. P. Janet, P. G. Boyd, Y. Lee, B. Smit and H. J. Kulik, *Nat Commun*, 2020, **11**, 4068.
2. C. S. Diercks, M. J. Kalmutzki, N. J. Diercks and O. M. Yaghi, *ACS Cent. Sci.*, 2018, **4**, 1457–1464.
3. F. Cui, Q. Deng and L. Sun, *RSC Adv.*, 2015, **5**, 98215–98221.
4. D. M. Pajerowski, J. E. Gardner, F. A. Frye, M. J. Andrus, M. F. Dumont, E. S. Knowles, M. W. Meisel and D. R. Talham, *Chem. Mater.*, 2011, **23**, 3045–3053.
5. N. R. de Tacconi, K. Rajeshwar and R. O. Lezna, *Chem. Mater.*, 2003, **15**, 3046–3062.
6. J. Wyart, *bulmi*, 1926, **49**, 148–159.
7. G. Wilkinson, M. Rosenblum, M. C. Whiting and R. B. Woodward, *J. Am. Chem. Soc.*, 1952, **74**, 2125–2126.
8. V. W. Day, M. F. Fredrich, W. G. Klemperer and R. S. Liu, *J. Am. Chem. Soc.*, 1979, **101**, 491–492.
9. G. Brand, M. W. Hosseini, O. Félix, P. Schaeffer and R. Ruppert, in *Magnetism: A Supramolecular Function*, ed. O. Kahn, Springer Netherlands, Dordrecht, 1996, pp. 129–142.
10. B. F. Hoskins and R. Robson, *J. Am. Chem. Soc.*, 1990, **112**, 1546–1554.
11. O. M. Yaghi, G. Li and H. Li, *Nature*, 1995, **378**, 703–706.
12. M. Kondo, T. Yoshitomi, H. Matsuzaka, S. Kitagawa and K. Seki, *Angew. Chem. Int. Ed. Engl.*, 1997, **36**, 1725–1727.
13. T. Loiseau and G. Férey, *J. Chem. Soc., Chem. Commun.,* 1992, 1197-1198.
14. H. Li, M. Eddaoudi, M. O'Keeffe and O. M. Yaghi, *Nature*, 1999, **402**, 276–279.
15. M. J. Kalmutzki, N. Hanikel and O. M. Yaghi, *Science Advances*, 2018, **4**, eaat9180.
16. A. Permyakova, S. Wang, E. Courbon, F. Nouar, N. Heymans, P. D'Ans, N. Barrier, P. Billemont, G. De Weireld, N. Steunou, M. Frère and C. Serre, *J. Mater. Chem. A*, 2017, **5**, 12889–12898.
17. M. Riou-Cavellec, C. Albinet, J.-M. Grenèche and G. Férey, *J. Mater. Chem.*, 2001, **11**, 3166–3171.
18. F. Millange, C. Serre and G. Férey, *Chem. Commun.*, 2002, 822–823.

19. M. Dan-Hardi, H. Chevreau, T. Devic, P. Horcajada, G. Maurin, G. Férey, D. Popov, C. Riekel, S. Wuttke, J.-C. Lavalley, A. Vimont, T. Boudewijns, D. de Vos and C. Serre, *Chem. Mater.*, 2012, **24**, 2486–2492.
20. Y.-Z. Li, G.-D. Wang, W.-J. Shi, L. Hou, Y.-Y. Wang and Z. Zhu, *ACS Appl. Mater. Interfaces*, 2020, **12**, 41785–41793.
21. E. Barea, C. Montoro and J. A. R. Navarro, *Chem. Soc. Rev.*, 2014, **43**, 5419–5430.
22. T. M. McDonald, W. R. Lee, J. A. Mason, B. M. Wiers, C. S. Hong and J. R. Long, *J. Am. Chem. Soc.*, 2012, **134**, 7056–7065.
23. A. R. Millward and O. M. Yaghi, *J. Am. Chem. Soc.*, 2005, **127**, 17998–17999.
24. O. K. Farha, A. Özgür Yazaydın, I. Eryazici, C. D. Malliakas, B. G. Hauser, M. G. Kanatzidis, S. T. Nguyen, R. Q. Snurr and J. T. Hupp, *Nature Chemistry*, 2010, **2**, 944–948.
25. Furukawa Hiroyasu, Ko Nakeun, Go Yong Bok, Aratani Naoki, Choi Sang Beom, Choi Eunwoo, Yazaydin A. Özgür, Snurr Randall Q., O'Keeffe Michael, Kim Jaheon, and Yaghi Omar M., *Science*, 2010, **329**, 424–428.
26. Ü. Kökçam-Demir, A. Goldman, L. Esrafili, M. Gharib, A. Morsali, O. Weingart and C. Janiak, *Chem. Soc. Rev.*, 2020, **49**, 2751–2798.
27. H. Wu, J. M. Simmons, G. Srinivas, W. Zhou and T. Yildirim, *J. Phys. Chem. Lett.*, 2010, **1**, 1946–1951.
28. R. M. Rego, G. Kuriya, M. D. Kurkuri and M. Kigga, *Journal of Hazardous Materials*, 2021, **403**, 123605.
29. S. Rojas, J. A. R. Navarro and P. Horcajada, *Dalton Trans.*, 2021, **50**, 2493–2500.
30. L. Joseph, B.-M. Jun, M. Jang, C. M. Park, J. C. Muñoz-Senmache, A. J. Hernández-Maldonado, A. Heyden, M. Yu and Y. Yoon, *Chemical Engineering Journal*, 2019, **369**, 928–946.
31. N. K. Gupta, Y. Ghaffari, S. Kim, J. Bae, K. S. Kim and M. Saifuddin, Sci. Rep., 2020, 10, 4942.
32. 1C. Zhang, H. Li, C. Li and Z. Li, Molecules, DOI:10.3390/molecules25010168.
33. E. F. D. Januário, T. B. Vidovix, R. Bergamasco and A. M. S. Vieira, *Chemical Engineering and Processing - Process Intensification*, 2021, **168**, 108577.
34. N. Nikooe and E. Saljoughi, *Applied Surface Science*, 2017, **413**, 41-49.
35. E. Haque, V. Lo, A. I. Minett, A. T. Harris and T. L. Church, J. Mater. Chem. A, 2014, 2, 193.
36. X. Lin, J. Jia, X. Zhao, K. M. Thomas, A. J. Blake, G. S. Walker, N. R. Champness, P. Hubberstey and M. Schröder, *Angew. Chem. Int. Ed.*, 2006, **45**, 7358–7364.

37. G. Cai and H.-L. Jiang, *Angewandte Chemie International Edition*, 2017, **56**, 563–567.
38. T. A. Makal, X. Wang and H.-C. Zhou, *Crystal Growth & Design*, 2013, **13**, 4760–4768.
39. N. Israfilov, K. Soukup, B. Louis and J.-M. Planeix, *New J. Chem.*, 2022, **46**, 8967–8970.
40. M. Bosch, M. Zhang and H.-C. Zhou, *Advances in Chemistry*, 2014, **2014**, 1–8.
41. D. Asnaghi, R. Corso, P. Larpent, I. Bassanetti, A. Jouaiti, N. Kyritsakas, A. Comotti, P. Sozzani and M. W. Hosseini, *Chem. Commun.*, 2017, **53**, 5740–5743.
42. H.-M. Wen, G. Chang, B. Li, R.-B. Lin, T.-L. Hu, W. Zhou and B. Chen, *Crystal Growth & Design*, 2017, **17**, 2172–2177.
43. C. Serre, F. Millange, C. Thouvenot, M. Noguès, G. Marsolier, D. Louër and G. Férey, *J. Am. Chem. Soc.*, 2002, **124**, 13519–13526.
44. D. Bůžek, S. Adamec, K. Lang and J. Demel, *Inorg. Chem. Front.*, 2021, **8**, 720–734.
45. X. Ye and D. Liu, *Crystal Growth & Design*, 2021, **21**, 4780–4804.
46. J. M. Timko, R. G. Helgeson, M. Newcomb, G. W. Gokel and D. J. Cram, *JACS*, 1974, **96(22)**, 7097–7099.
47. J.-M. Lehn, *Pure Appl. Chem.*, 1980, **52(11)**, 2441–2459.
48. C. J. Pedersen, *JACS*, 1967, **89(26)**, 7017–7036.
49. A. Perrin, D. Myers, K. Fucke, O. M. Musa and J. W. Steed, *Dalton Trans.*, 2014, **43**, 3153–3161.
50. J.-Y. Jung, S.-H. Ko, S.-L. Park, H.-H. Shin, H.-C. Oh, J.-W. Ryu, S.-C. Lee, O.-P. Kwon and E.-Y. Choi, *Macromol. Res.*, 2017, **25**, 1100–1104.
51. Z. Xue, J. Zhang, L. Peng, B. Han, T. Mu, J. Li and G. Yang, *ChemPhysChem*, 2014, **15**, 85–89.
52. B. Tsai, O. Garcia-Valdez, P. Champagne and M. Cunningham, *Processes*, 2017, **5**, 12.
53. I. Abánades Lázaro, S. Haddad, S. Sacca, C. Orellana-Tavra, D. Fairen-Jimenez and R. S. Forgan, *Chem*, 2017, **2**, 561–578.
54. D. Wang, Q. Wang, W. Zheng, Y. Dai, X. Ruan, X. Li and G. He, *Ind. Eng. Chem. Res.*, 2022, **61**, 6650–6661.
55. V. Muthukumaraswamy Rangaraj, M. A. Wahab, K. S. K. Reddy, G. Kakosimos, O. Abdalla, E. P. Favvas, D. Reinalda, F. Geuzebroek, A. Abdala and G. N. Karanikolos, *Front. Chem.*, 2020, **8**, 534.

CHAPTER 1. Synthesis of the ligands.

I. Introduction

The novelty of this work is to design, prepare and use new ligands allowing to obtain MOFs with structural properties close to those obtained from model ligands while bringing new recognition properties allowing new applications to these materials.
The challenge of the synthesis of these new ligands is therefore to find synthesis schemes for these functionalized ligands that are sufficiently efficient to consider applications in trapping or separation.
As our choice of functionalization was based on polyoxyethylene chains, we had to adapt these syntheses to the specificity of these fragments.

II. Tetracarboxylic ligands

In this chapter, we will describe the grafting of polyoxyethylene chains to ligands. During the synthesis processes, different reactions were used. Such as Williamson ether synthesis, Suzuki-Miyaura coupling, etc. It is worth mentioning that the synthesis and purification methods are nearly the same for different size glyme chains for the same class of ligands. For example, there are no fundamental differences in the synthesis of the H4L2 and H4L4. The structure of the ligands is given in figure 16. Just to mention that the nomenclature of the ligands is based on oxygen numbers in the chain rather than the n. For example, H4L2 is the ligand where n=1. As a rule of thumb, the ligand name is equal to n+1. The first tetracarboxylic ligand with a terphenyl backbone was synthesized by Schröder and al. [1]. As the central phenyl ring was without functionalization, there was only a Suzuki coupling reaction followed by saponification (fig.17a). Later, some functionalized versions were synthetized by Zhou and al. [2]. They added different-sized alkoxy chains. One of the examples is given in figure 17b. As the middle phenyl ring bears alkoxy groups, several additional steps are added to the synthesis. However, as usual, it finishes with saponification of the tetraester. In our case (fig.17c), firstly we synthesized as other scholars, however, the process was time-consuming, the solvents were toxic and the prices were relatively high. Therefore, we decided to improve the synthesis.

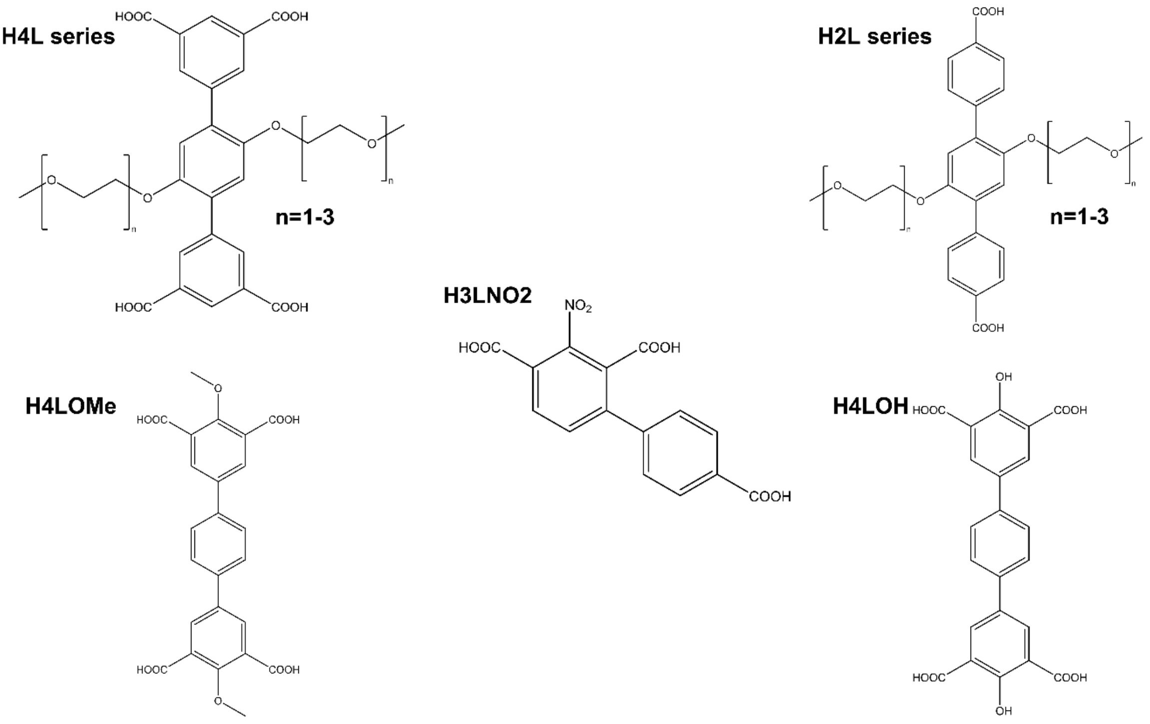

Figure 16. Synthetized ligands during the thesis.

The details are given during the chapter. One example of simplification is the direct synthesis of the ligand with acid-bearing groups, rather than an ester.

Also, schematized version of our synthesis with yields is given in figure 18. However, all the details (reactions, quantities, yields, analyses, etc.) are given in the experimental section.

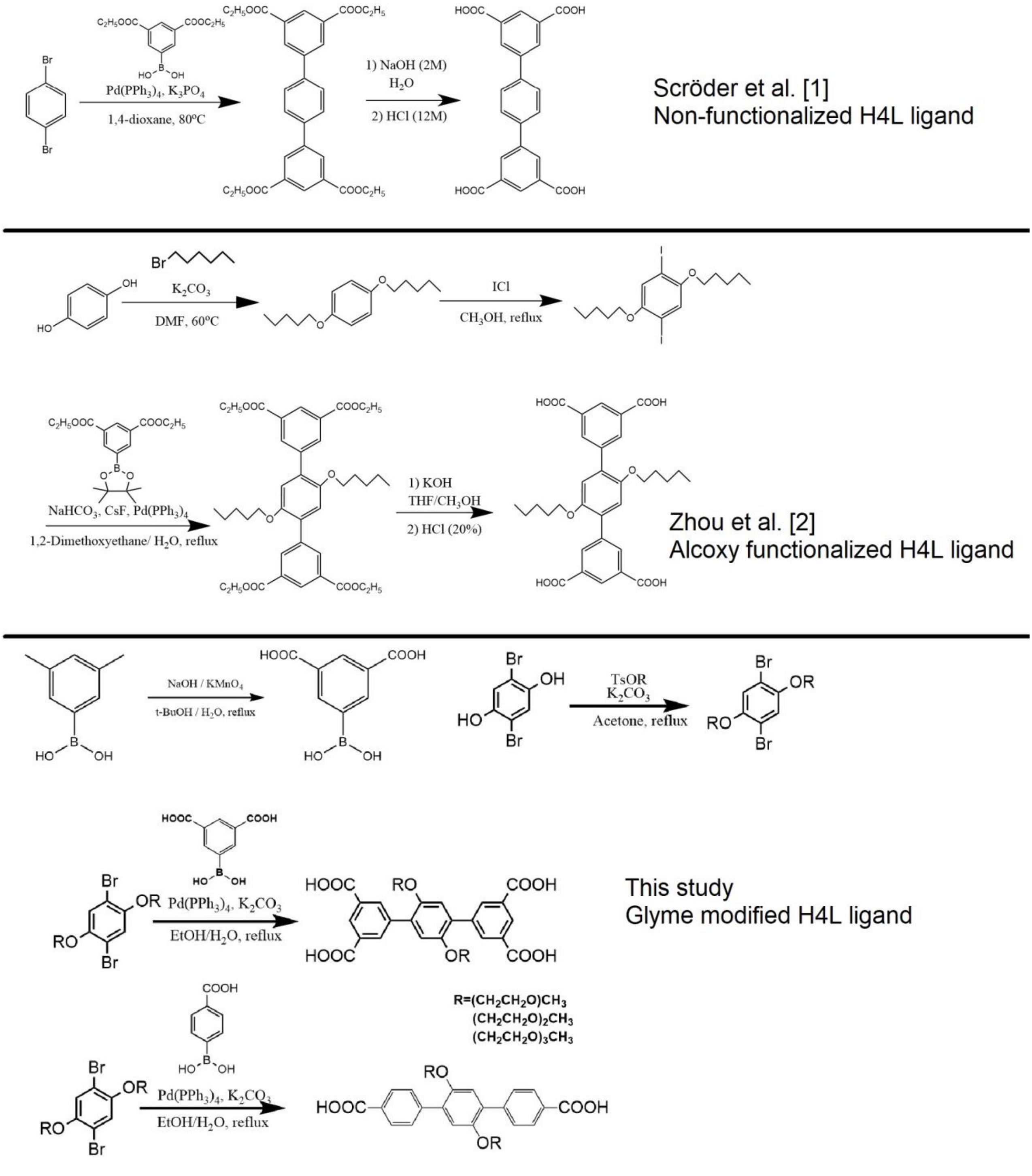

Figure 17. Synthesis of various H4L ligands. A-non-functionalized; B-alkoxy functionalized; C-glyme functionalized.

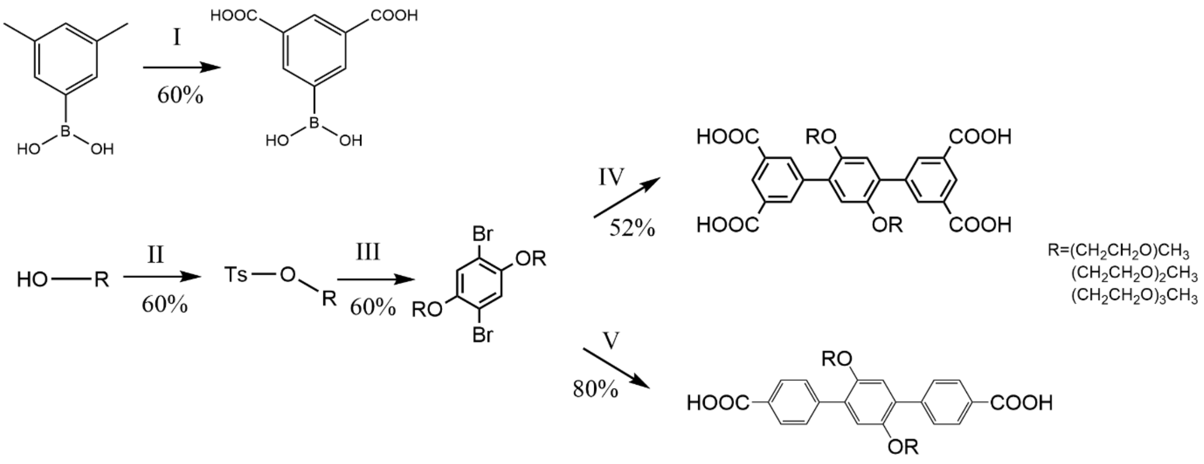

Figure 18. Schematic illustration of the synthesis with an average yield.

The synthesis of H4L series ligands began with the modification of the 5-bromo derivative of isophthalic acid (5-bromo benzene 1,3 dicarboxylic acid) to the boronic ester group, despite boronic ester being commercially available but very expensive…

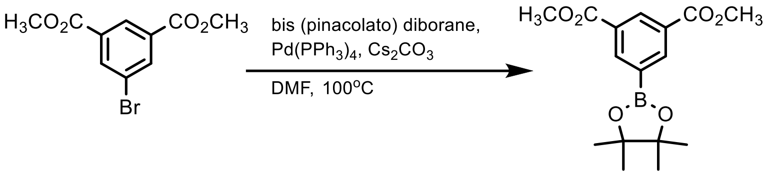

Reaction 1. Boronic ester synthesis. [3]

For this reaction, palladium catalyst and DMF were used and the product isolation require column chromatography purification. All of these made a reaction expensive, toxic, and time-consuming. We improve the synthesis with the following reaction and procedures [4]:

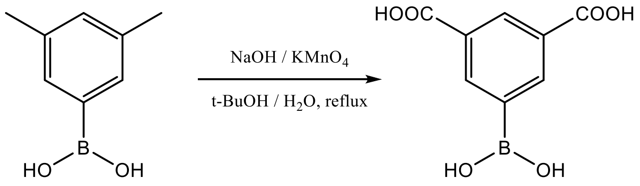

Reaction 2. Boronic acid synthesis.

First, departing compound costs less than in the first reaction. Later, we get rid of palladium catalyst (expensive), DMF (toxic and difficult to eliminate), Cs2CO3 (expensive), high temperature (energy efficient), and finally column purification (use of toxic solvents, expensive, time-consuming). We indeed lose a little bit on yield (around 80 to 65%), but all the aforementioned advantages make the process effective.

As a next step, we prepared the "middle" part of the ligands, which includes 2 steps: Grafting glycol ether to the tosyl group and Williamson ether synthesis. The tosylation reaction is given below:

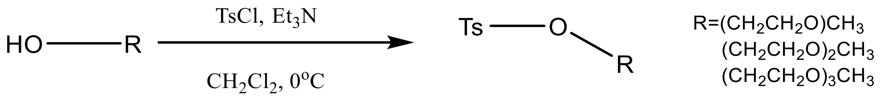

Reaction 3. Adding tosyl group to glycol ether [5].

In this reaction, a toxic solvent (dichloromethane) was used. Also, after the reaction column purification is applied to extract the product (some scholars do not use the column). Therefore, we decided to use another known method [6].

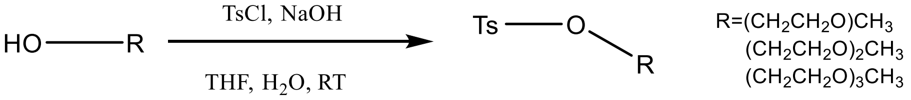

Reaction 4. Adding tosyl group to glycol ether.

We replaced triethylamine with NaOH and despite the miscibility of THF/water, in this reaction, they created separate layers. Those layers on the one hand facilitated separation, and on the other hand, obtained organic product dissolved in THF. Thus, without column purification only with a few sample washings with water, dichloromethane, and diethyl ether products were obtained with around 60% yields.

In the next step, tosylated glycol ether reacted with 2,5-dibromohydroquinone to obtain dibromo ether [6].

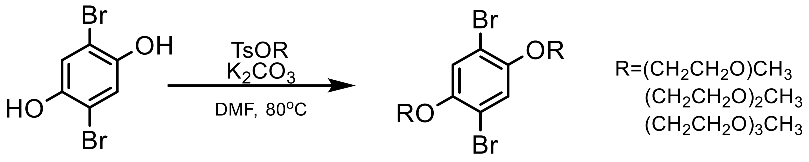

Reaction 5. Williamson ether synthesis.

In this step, there are also several synthetic constraints that we wanted to optimize. Some of them are the same that the previous ones. Such as using high boiling point toxic solvent and column purification. The main difficulty was the formation of dibromobenzoquinone. First of all, it is a side product of oxidation, and secondly, even a trace amount of it gives a red color to the final product. After tens of attempts, we changed again the reaction and found how to avoid dibromobenzoquinone. The new reaction is given below [7]:

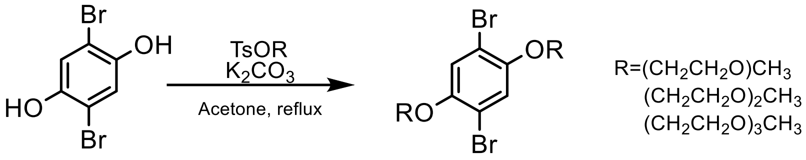

Reaction 6. Williamson ether synthesis.

Again, DMF is replaced with acetone: less toxic, cheap, low boiling point. Also, column purification is avoided. However, to increase the purity of the product we added an easy step. As the obtained product is ether and it is very stable after the reaction solvent evaporated. Some methanol, water, and NaOH are added to the mixture and it is heated to 50°C, mixed for about 5 min. Later organic phase evaporated and depending on the length of the chain, the aqueous phase was washed with diethyl ether or dichloromethane.

In order to avoid dibromobenzoquinone formation oxygen should be eliminated at maximum. Therefore, the reaction mixture was evacuated and filled with nitrogen 5-6 times.

The next step was the bridging "middle part" with other terminal parts. Suzuki-Miyaura coupling was performed. The saponification reaction followed the coupling yielding to our ligands. It is worth mentioning that after coupling column purification was used.

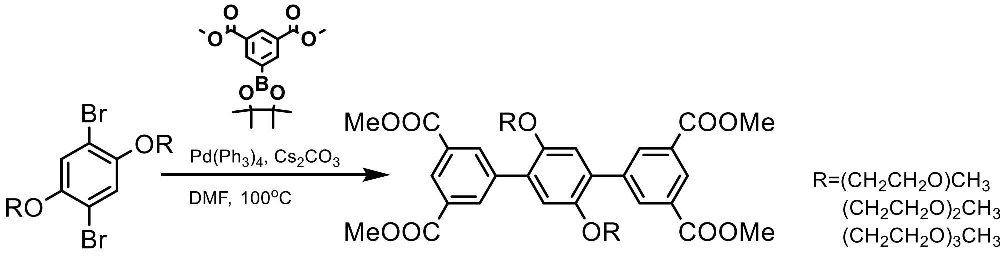

Reaction 7. Suzuki coupling.

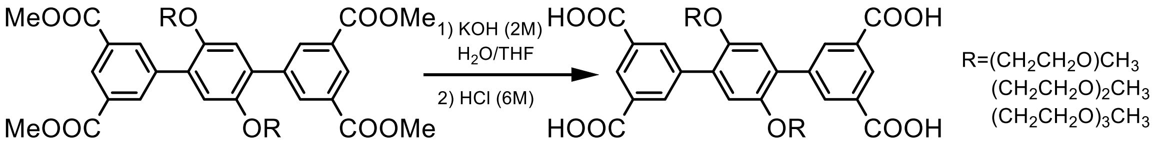

Reaction 8. Saponification.

Again, we tried to simplify our work as suggested by Leonardo Da Vinci "The simplicity is the ultimate sophistication". At reaction 2, we obtained boronic acid by the mean of oxidation. We decided to do coupling directly with carboxylic acid-bearing boronic acid and dibromo ether, without passing through the 'protected' forms of the four acid functions, i.e. the four isophthalate ends of the initial synthesis.

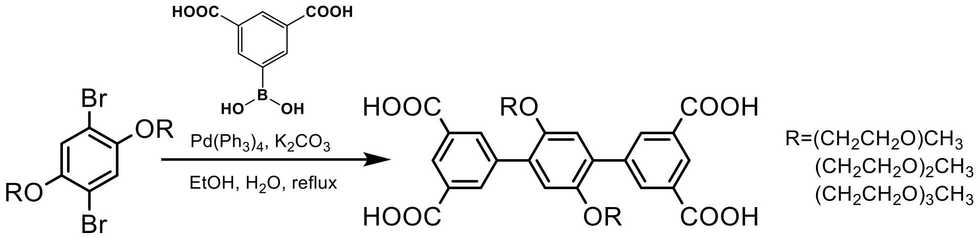

Reaction 9. Direct coupling 2,5 carboxyphenyl boronic acid with dibromo ether.

This time we avoided 1 step with column purification. Also, we replaced Cs_2CO_3 with K_2CO_3, which is much cheaper.

The detailed synthesis procedure and all analyses are given in supplementary information. Just to mention that, we observed K^+ or Na^+ ions in elementary analysis and/or LR-MS for some long-chain acids and/or esters. Despite several purifications, we could not get rid of them. This could be considered a fraction of residual carboxylates salts or also as a high affinity of glyme side chains for cations.

III. Dicarboxylic ligands

The success of MOFs with tetracarboxylic ligands motivated us to make its dicarboxylic analogs. As we have improved synthesis methods for tetracarboxylic ligands, we have in the same way adapted for “H2L” series ligands which were obtained in 3 steps without column purification. The advantage of synthesis compared to its tetracarboxylic analogs is that carboxyphenyl boronic acid is commercially available for an affordable price. Therefore, only 3 steps are required for obtaining ligands. Moreover, as the “middle parts” of both ligands are the same, reactions 4 and 6 are repeated for the synthesis. In the last step carboxyphenyl boronic acid coupled with dibromo ether.

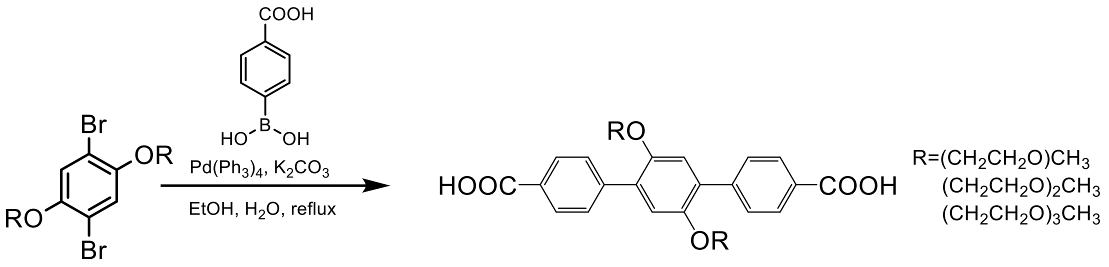

Reaction 10. The final step of H2L synthesis.

IV.New model ligands

A complementary approach to our study concerning the development of new ligands to obtain MOFs with different structural or chemical properties consisted in imagining alternative coordination modes to those previously described. In this respect, two avenues were considered.

The first is to modify the coordination modes of the target tetracarboxylic ligands either by introducing a functional group likely to participate in the coordination of metals or by blocking the possibility of coordination of two adjacent carboxylate groups. The second is to introduce a functional group that can modify the electronic properties of the aromatic rings involved in the coordination. The literature review led us to prepare aromatic rings with nitro groups between the two acid functions. The prepared ligands were used as model ligands to study the coordination mode of the target metals. In this category, there are 3 ligands, 2 of which are similar and one is completely different. Even in literature, there are not any comparable ligands. The main motivations for the synthesis were the novelty of the ligand and the change of coordination properties of the ligands. For example in the case of H4LOH, there are 3 coordinating groups on each side of the ligand. Also, adding a hydroxy group between acid groups will significantly change their pKa, which will change the nature of the ligand. The steps of the synthesis of H4LOMe and H4LOH is given in reaction 11 and 12.

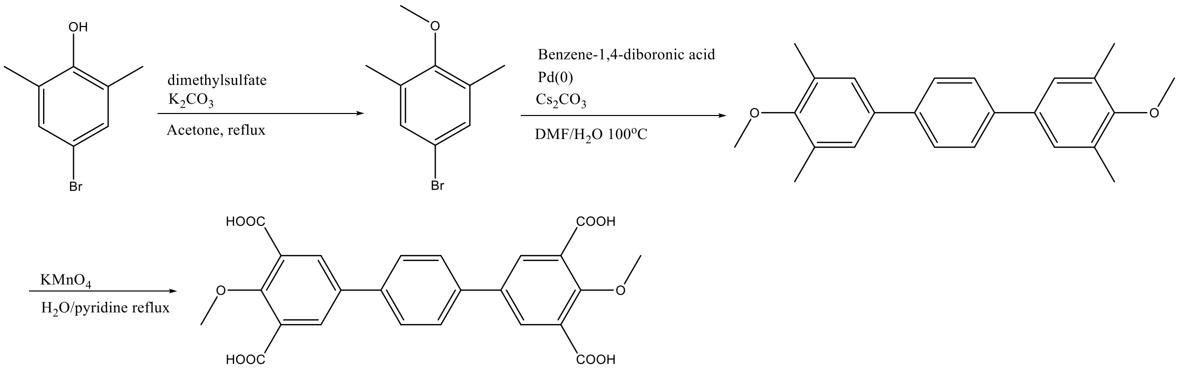

Reaction 11. Synthesis of H4LOMe.

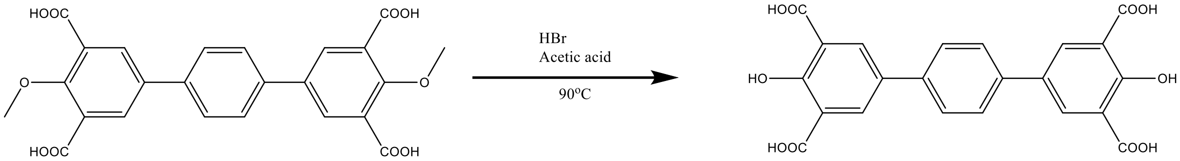

Reaction 12. Synthesis of H4LOH.

It is worth mentioning that in none of the steps column purification was not used. The MOFs with small ligands, which have high porosity and stability motivated us to synthesize the H3LNO2 ligand. The unique topology of HKUST-1, UiO-66, and some MIL series MOFs made them a strong candidate for different applications. Furthermore, the nitro group has several impacts. Firstly, it is a polar molecule that can make good interaction with guest species. In the paper of Schröder et al. [8] tetraphenyl tetracarboxylic ligand was modified with different groups, including amino, and nitro, and by surprise, the best adsorption was observed not with amino but nitro decorated MOFs. They explain this firstly by direct interaction of nitro groups with CO2 and binding of CO_2 to –CH hydrogen bond donors that is augmented by the electron withdrawing effects of the $–NO_2$ groups. These were observed by INS (Inelastic neutron scattering), NPD (Neutron powder diffraction) and FT-IR analyses. The structure of the ligands is given in figure 19.

Another impact that may be negative is that the nitro group decreases the pKa of the ligand, especially when it is situated between two acid groups. As a rule of thumb, the stability of the MOF decreases with decreasing pKa of the ligand.

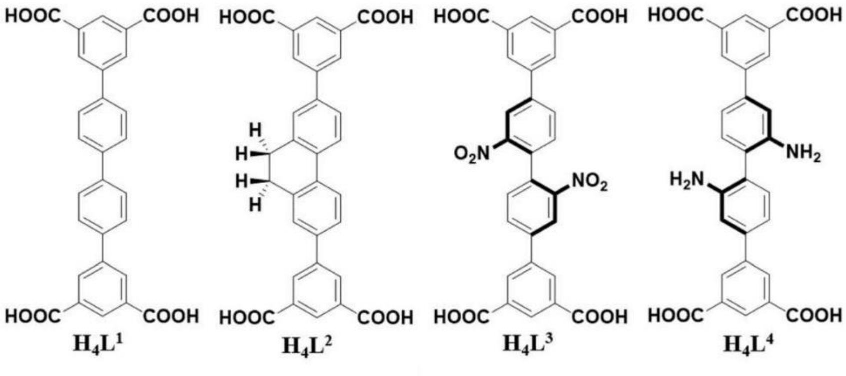

Figure 19. Ligands of the MOFs for CO_2 adsorption [8].

Therefore, we decided to create some small ligands with unusual coordination abilities. It is difficult (nearly impossible) to predict the exact topology of the MOFs, but it is interesting to design new tectons and observe their self-assembly even if there are no tetratopic ligands to be compared with the previous one. Synthesis of the H3LNO2 is given in reaction 13.

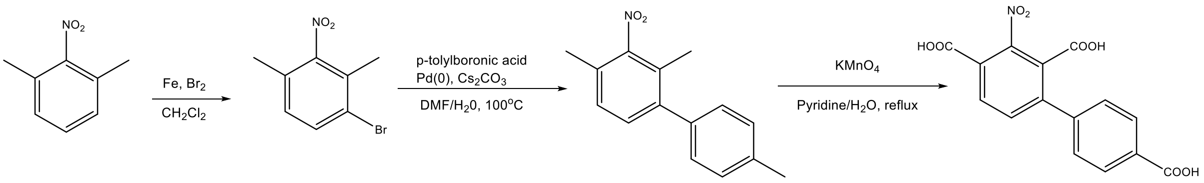

Reaction 13. Synthesis of the H3LNO2.

Unfortunately, we could not obtain any structure with this ligand. Two crystals, one with copper and another with zirconium were synthesized, but unfortunately, the quality of the crystals was not good. The photo of the crystals is given in figure18.

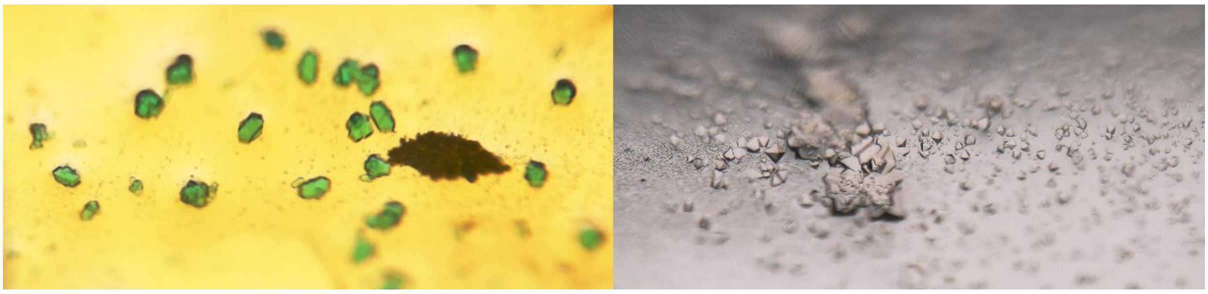

Figure 20. Left-crystals of Cu@H3LNO2; Right-crystals of Zr@H3LNO2.

V. Choice of Metal centers

Generally, the first things that come into the head as metals in the MOF synthesis are copper and zinc. Therefore, for most of the ligands, we have copper and zinc MOFs. As the synthesized MOFs are a lot, in table 2 we gave MOFs that were obtained as a single crystal and/or structure proved by powder XRD technique using known isostructural MOFs. Also, it is worth underlining that we could synthesize some MOFs, but due to weak attractiveness for applications, they are not synthesized. We gave the latter in the red color.

Table 2. The ligands and MOFs are synthetized.

Ligands	H4L2	H4L3	H4L4	H2L2*	H2L3	H2L4	H4LOMe	H4LOH	H3LNO2
MOFs	Cu Ni Ca	Cu Ni Zn Ca Mg	Cu Ni Ca	Zn	Zn	Zn Zr	Cu Zn Ca	Cu Ca	

*Mixed ligand MOF with 4,4’-bipyridine with Zn also synthetized

Moreover, new MOFs with known ligands also was synthesized. Such as Mg@H4L1 and Ni@H4L1. In the next chapter, we will see the characterization of the obtained MOFs.

VI.Conclusion

9 new ligands were synthesized and completely characterized (H-NMR, C-NMR, LR-MS, elemental analysis). The results of these analyses are given in experimental part. Besides synthesis, the synthetic protocols also improved significantly. We succeeded to decrease the number of steps from 5 with 4 chromatographic purifications for the H4L series to 4 steps without any chromatography. For the H2L series, we decreased the steps to 3 without any column purification. Overall, we used less toxic solvents, and cheaper compounds, and all of these performed in much less time. For example, for H2L series ligands, we can synthesize up to 5 grams per week (1 batch) in the laboratory, and this is at a normal pace.

Our new model ligands are completely new in their class. Despite most of the obtained MOFs with them being in presence of solvents (coordinated) or they are 1 or 2D and it makes them less stable and diminishes the field of application. However, we strongly believe that the MOFs with high oxidation numbers ($Al^{3+,}$ Zr^{4+}, etc.), especially with H4LOH will lead to high surface area and stable MOFs with interesting topology. We already obtained Zr@H4LOH but crystals are small for single crystal analysis. It is worth mentioning that, the price of this ligand is not high as the H4L series. Also, we use simplified synthesis without column purification.

The last ligand- H3LNO2 was also synthesized in a few easy steps. Further improvements could be applied, such as replacing DMF, pyridine, or Cs_2CO_3. However, as we did not obtain any crystal with the ligand further studies stopped. Despite a small pKa, its MOFs with high valence metals seem interesting to obtain. Because their topology is unpredictable and interesting.

References

1. X. Lin, I. Telepeni, A. J. Blake, A. Dailly, C. M. Brown, J. M. Simmons, M. Zoppi, G. S. Walker, K. M. Thomas, T. J. Mays, P. Hubberstey, N. R. Champness and M. Schröder, *J. Am. Chem. Soc.*, 2009, **131**, 2159–2171. 1
2. T. A. Makal, X. Wang and H.-C. Zhou, *Crystal Growth & Design*, 2013, **13**, 4760–4768.
3. X. Duan, J. Yu, J. Cai, Y. He, C. Wu, W. Zhou, T. Yildirim, Z. Zhang, S. Xiang, M. O'Keeffe, B. Chen and G. Qian, *Chem. Commun.*, 2013, **49**, 2043–2045.
4. Y. Zhou, L. Kan, J. F. Eubank, G. Li, L. Zhang and Y. Liu, *Chem. Sci.*, 2019, **10**, 6565–6571.
5. Thesis of R.Corso, Conception et étude des propriétés physico-chimiques de réseaux de coordination, 2018, University of Strasbourg.
6. D. A. Vazquez-Molina, G. M. Pope, A. A. Ezazi, J. L. Mendoza-Cortes, J. K. Harper and F. J. Uribe-Romo, *Chem. Commun.*, 2018, **54**, 6947–6950.
7. Z. Zhang, Z. Zhao, Y. Hou, H. Wang, X. Li, G. He and M. Zhang, *Angewandte Chemie International Edition*, 2019, **58**, 8862–8866.
8. T. D. Duong, S. A. Sapchenko, I. da Silva, H. G. W. Godfrey, Y. Cheng, L. L. Daemen, P. Manuel, M. D. Frogley, G. Cinque, A. J. Ramirez-Cuesta, S. Yang and M. Schröder, *Chem. Sci.*, 2020, **11**, 5339–5346.

Chapter II: Synthesis and characterization of the MOFs

Schematic of nomenclature of MOFs

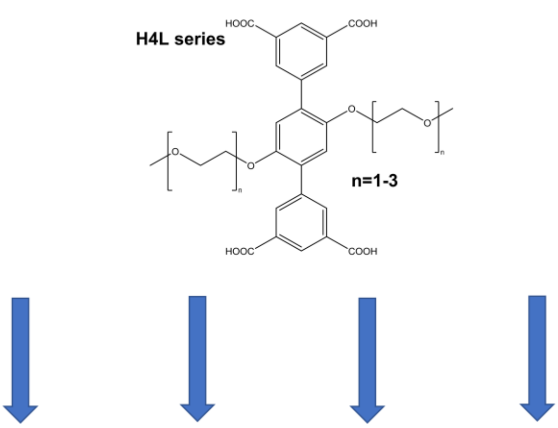

Cu^{2+}
SUM-100
series
n=1 SUM-102
n=2 SUM-103
n=3 SUM-104

Ni^{2+}
SUM-200
series
n=1 SUM-202
n=2 SUM-203
n=3 SUM-204

Ca^{2+}
SUM-300
series
n=1 SUM-302
n=2 SUM-303
n=3 SUM-104

Mg^{2+}
SUM-400
series
n=0 SUM-401
n=2 SUM-403
(with DMF)

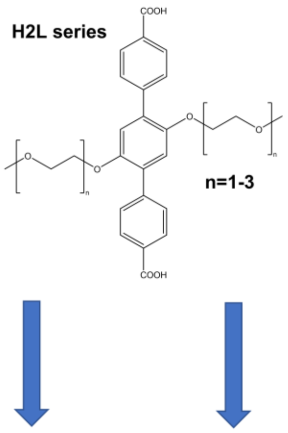

Zn^{2+}
SUM-500 series
n=1 SUM-552 (with
4,4' bipyridyl)
n=2 SUM-503

Zr^{2+}
SUM-600 series
n=2 SUM-603

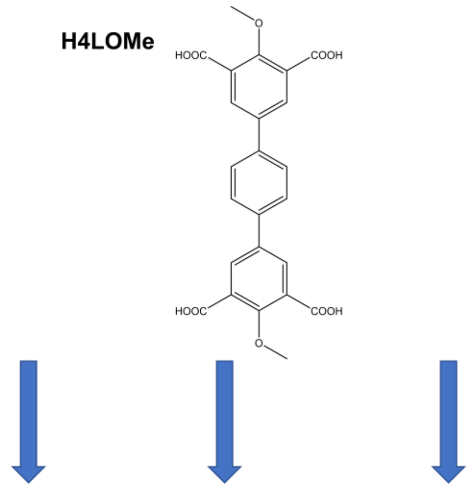

Cu^{2+}
LBM-10

Ca^{2+}
LBM-30

Zn^{2+}
LBM-50
with methyl imidazole

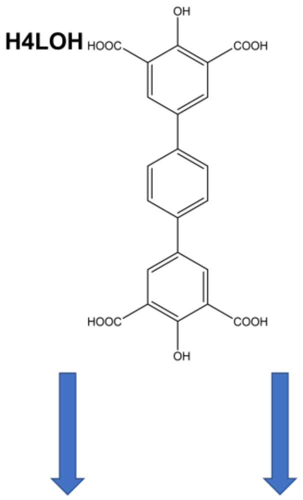

Cu^{2+}
LBM-20
with pyridine

Ca^{2+}
LBM-40
with DMF

I. Synthesis and characterization methods

All of our MOFs were synthetized under solvothermal conditions, except Cu@H4LOMe@pyridine, which was obtained by the liquid-to-liquid diffusion method. The temperature range was 80-120°C and the main solvent was DMF. After the synthesis, most of the MOFs were characterized by powder XRD (PXRD), FT-IR, TGA, SEM and N_2 adsorption-desorption isotherms. When the size of the crystals allowed it, single crystal XRD (SCXRD) was also performed to solve the MOFs topology.

After their synthesis, MOFs were filtered, rinsed with the solvents used in the preparation and dried under air. After, to ascertain the formation of the right phase, samples were analyzed by PXRD. Besides, FT-IR spectroscopy was also performed to investigate the structural vibrations created between the ligand and the metallic nodes (coordination of carboxylic groups). Thermogravimetric analysis (TGA) was done to determine the thermal stability of the materials, thus getting insights into the activation conditions of the MOFs for N_2 sorption analyses. BET (Brunauer–Emmett–Teller) surface analysis model was used to determine the specific surface area of the MOFs. However, before this analysis, the solvent molecules present inside the pores of the MOF need to be eliminated. This implies setting a suitable pre-treatment before the analysis. Sometimes, to ease the removal of the solvent molecules, they were replaced with low boiling point solvents. This is called the solvent exchange method. Also, there is another activation method with supercritical CO_2. This milder method is used when the MOFs are sensible to “classical” activation, as the supercritical liquids do not show the capillary effect [1]. In our experiments, the standard activation procedure was set to 150-160°C for 8 hours in a vacuum, without solvent exchange. These conditions was established after TGA and PXRD tests. Also, some visual changes were observed for some MOFs. For example, for SUM-103 upon complete activation MOF became very dark blue. However if not properly activated color stays pale blue (little but greenish).

The aforementioned analyses correspond to the minimum done for MOFs characterization. For selected “promising” materials, SEM and TEM analyses were also performed. The technical parameters of the analysis are given in the annex.

II. Tetracarboxylic acids

1) Synthesis and characterization of SUM-100 (Cu@H4L) series

During this work, H4L and H4L1 ligands were synthesized for comparison reasons with other MOFs. We will discuss their behavior later on in the CO_2 adsorption part.

As discussed before the first metals that came into our mind after the synthesis of the ligand were copper and zinc. It is important to mention that the same topology was obtained with both metals. However, increased stability usually exhibited by copper MOFs made them more interesting to study. In contrast, Zn MOFs were formed solely at 100°C in DMF with H4L and H4L3.

For copper, we obtained the whole series from H4L2, H4L3 and H4L4. The corresponding MOFs are called SUM- Strasbourg University Materials and some of them are published [1,2]. For the synthesis of these MOFs two methods were used, depending on the final size of the crystals. For SUM-102 (Cu@H4L2) we obtained good size crystals for SCXRD. For SUM-103 (Cu@H4L3) microcrystalline powder (crystals can be observed under an optical microscope but were small for SCXRD) and for SUM-104 (Cu@H4L4) powder were obtained. They all showed the same topology as parent NOTT-101 [3,4]. Despite an SCXRD of SUM-102, the flexibility of the side chains made them impossible to observe, many sites for each atom of this side chain are probably randomly occupied.

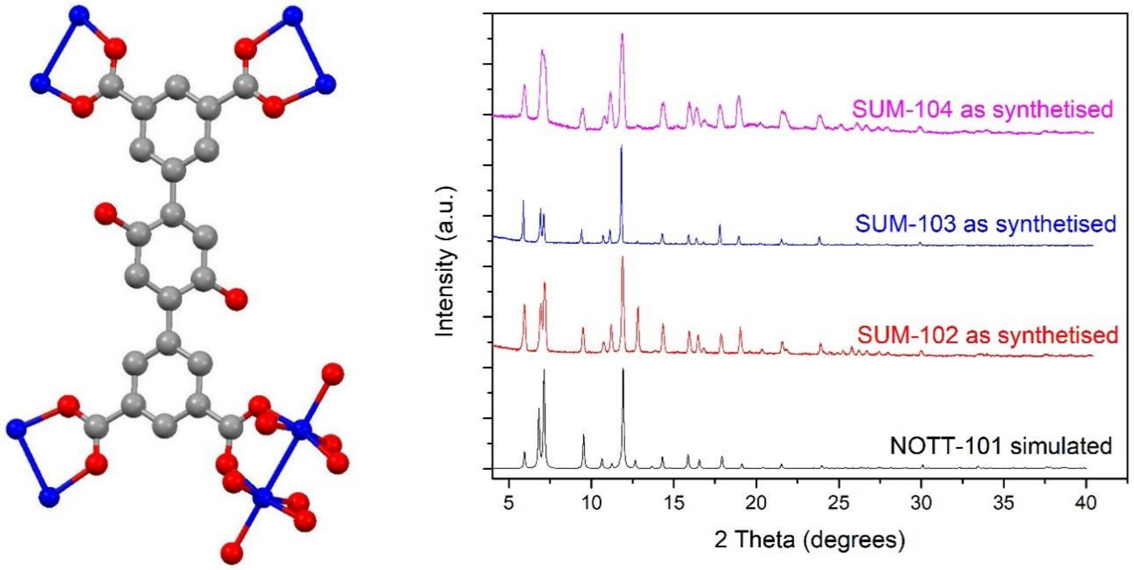

Figure 21. Left- Structure of SUM-102; Right- PXRD of SUM series MOFs.

The SBU (Secondary Building Unit) of the copper is a paddlewheel, where at axial positions water molecules are coordinated. The MOF with formula $C_{14}H_{15}CuO_7$, crystallized in a trigonal system with an R3-m space group. SUMs have 2 kinds of cylindric pores with the largest one approximately 9Å.

An important parameter has also been evaluated, namely the stability of the SUMs determined by PXRD, after activation and/or exposure to water. Schröder [5] and Zhou [6] showed extensive destruction of the NOTT-101 structure after activation and UTSA-90 after contact with water. The reason for the NOTT-101s collapse was the contact with humidity from the air after activation. However, the SUMs remained stable in water. The detailed study was done with SUM-103 (Figure 22).

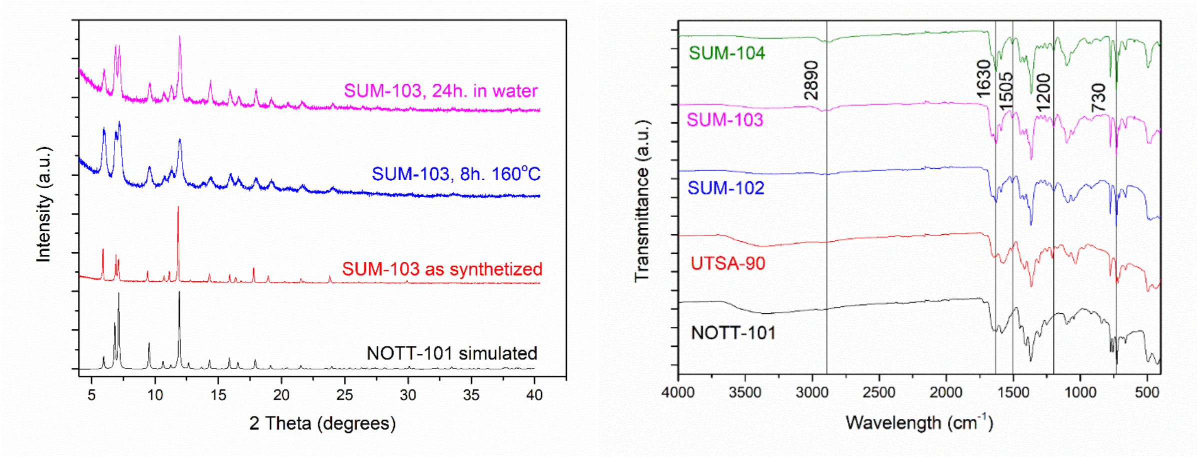

Figure 22. Stability study of SUM-103 (left) and FT-IR spectra of MOFs.

The reason for grafting glyme side chains was to create supramolecular interactions with guest molecules in the pore of the MOFs. However, unexpectedly they conferred high stability to the MOFs. The stability of the MOFs in water or toward humidity broadens their field of applications.

The FT-IR analysis realized also on NOTT-101 and UTSA-90 allows for making a comparative study (Figure 22). From this analysis, C-H stretching vibrations (2890 cm^{-1}) and skeletal vibrations of aromatic rings or C-C-O chains (1200 and 1505 cm^{-1}) demonstrate the presence of backbone and side chains. The latter could not be detected in NOTT-101.

The formation of SUM MOFs can also be deduced from the C=O stretching band shifted to lower energies due to the coordination of carboxylate groups to Cu (1630 cm^{-1}). Likewise, the Cu-O bond elongation band could be observed at 730 cm^{-1}.

After assessing the structure of the MOFs and their stability in water, the next step was the determination of their thermostability by TGA. For that reason SUMs were heated up to 450°C, at a 5°C min^{-1} rate. TGA analysis up to 450 °C under nitrogen of SUM-102, SUM-103 and SUM-104 are characterized by nearly the same profile (Figure 23). The first weight loss occurs in two waves and corresponds to solvents evaporation: one below 50 °C for most volatile ones and a second one between 70 °C and 240 °C for less volatile ones.

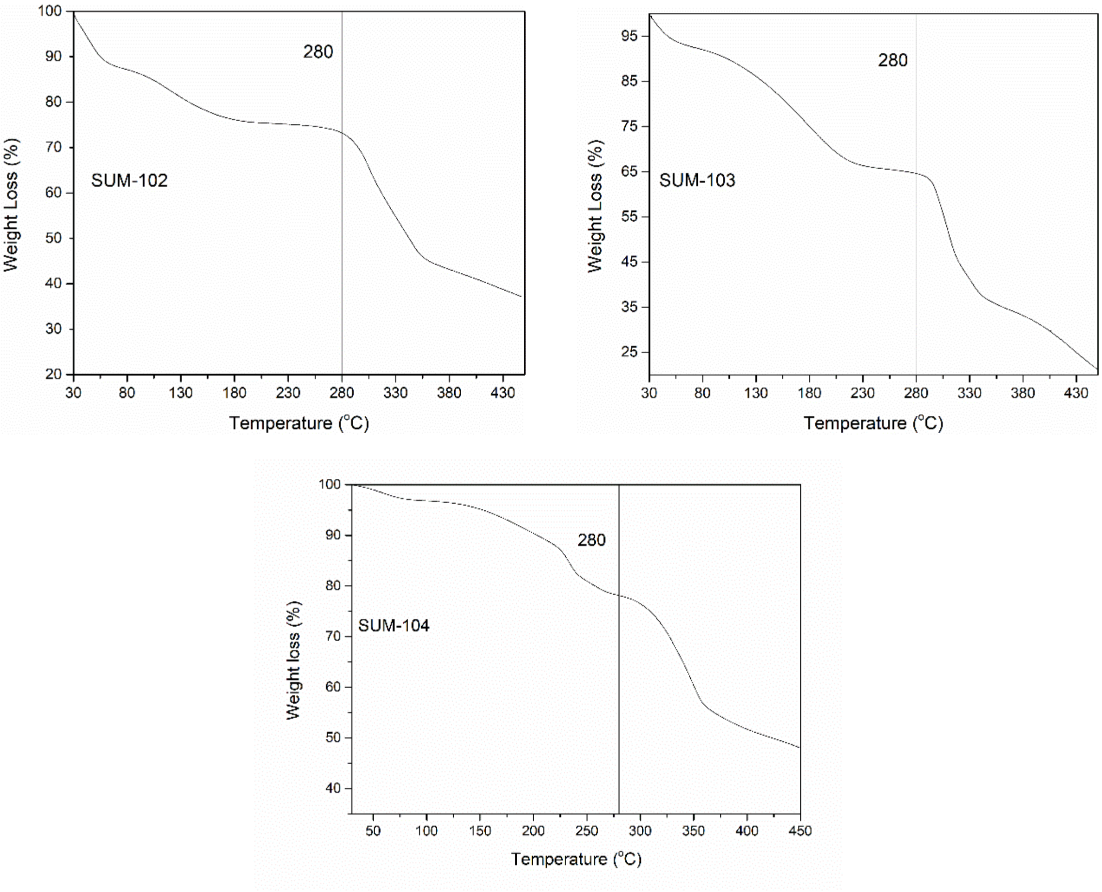

Figure 23. TGA of SUM-102, SUM-103 and SUM-104 materials

The decomposition of the MOFs started around 300°C, similarly to parent NOTT-101. Therefore, the addition of oxygen-rich side chains did not influence the thermal stability of the MOFs. An in-depth analysis of the thermograms indicates that the loss of solvent molecules occurs at higher temperatures while increasing the side chain length. For SUM-102 the end of the solvent loss is around 200°C, at 240°C for SUM-103 and nearly the same temperature as the beginning of the decomposition for SUM-104. This behaviour could be taken as an indicator of the occurrence of supramolecular interactions between side chains and solvent molecules (mainly DMF).

The morphologies of SUM-102 and SUM-103 crystals were investigated by SEM. The crystals exhibit nearly the same size, around 10-20 μm and an octahedral shape (figure 24).

An important descriptor of the MOFs textural properties is their *'a priori'* high surface area. The surface areas of the MOFs were measured with nitrogen and argon.

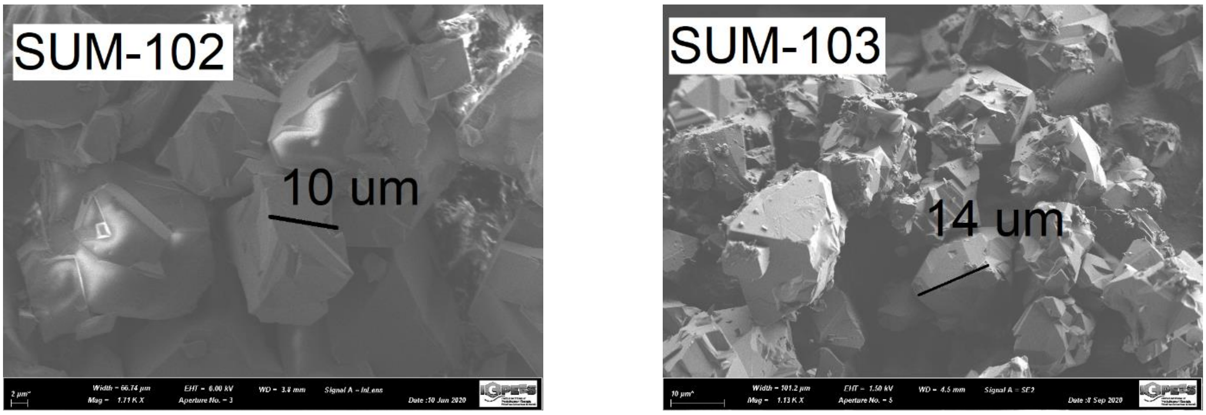

Figure 24. SEM images of SUM-102 and SUM-103.

They showed nearly the same value (Table 3). Nitrogen adsorption-desorption isotherms are presented in Figure 25.

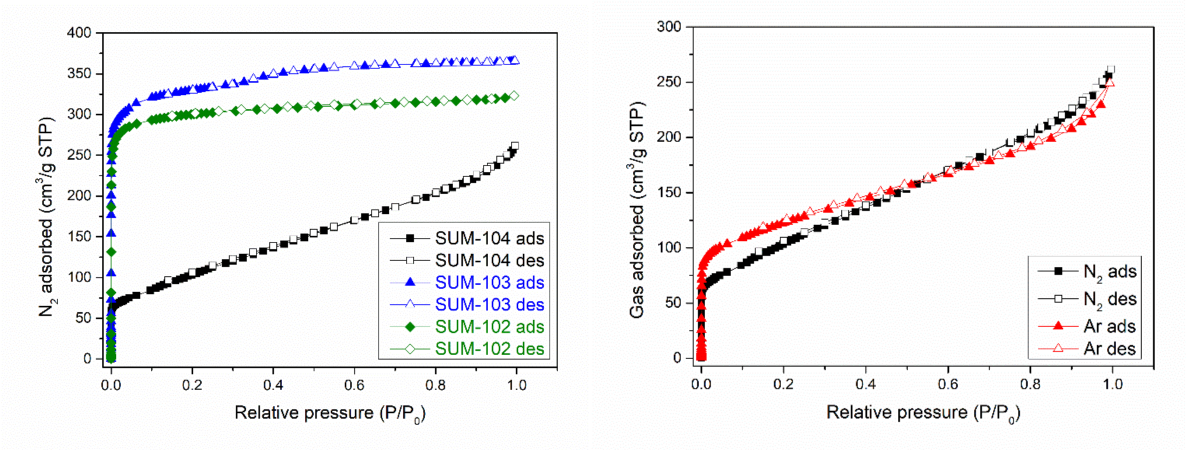

Figure 25. Left-Nitrogen adsorption isotherms of MOFs; Right- Ar and N_2 isotherms of SUM-104.

It is important to note that these isotherms show different and rather unexpected trends. Normally, we forecasted decreased surface areas with increased side chains. Solely, SUM-104 followed this assumption, exhibiting a mixture of type I (strong adsorption at low pressure region) and type II isotherm. In principle, type II isotherms are observed for macroporous or non-porous materials.

It can therefore be seen that the material with the longest side chains carrying two ethyleneoxy units (SUM-103) has a greater adsorption capacity than the material with only one ethylenoxy (SUM-102) unit as side chains. A similar observation was explained by Zhou et al. as the pore splitting effect of large side chains, which created an optimal "*space*" matching the kinetic diameter of N_2 [7].

Unfortunately, it was barely possible to find a comparative study in literature with SUM-104. Solely, in the study from Srivastava [8], Cu-BTC (HKUST-1) showed a type II isotherm, being less pronounced than SUM-104. Moreover, the reasons behind this kind of adsorption were not explained [8]. All the MOFs show type I isotherm versus Nitrogen or Argon. The slow kinetics of the adsorption process in the isotherm of SUM-104 could be explained (at least partially) by the steric hindrance generated by the long chains toward gas molecules entering the pores. This may also explain the sudden decrease in surface area. The increase in the length of the side chains in SUM-102, SUM-103 and SUM-104 is the same. In contrast, the BET surface areas measured for SUM-102 were 869 $m^2\ g^{-1}$, 1058 $m^2\ g^{-1}$ for SUM-103, and 385 $m^2\ g^{-1}$ for SUM-104. Another indication of the slow kinetics could be the same adsorption values for Ar and N_2 at the highest relative pressure. Their path is slightly different, with Ar isotherm closer to type I. As the kinetic diameter of Ar is smaller than N_2, also its more inert gas, the adsorption kinetics is slightly higher in Ar. Also, the absence of a hysteresis loop between adsorption and desorption shows that there is no strong interaction between side chains and host molecules and adsorption is purely physical, therefore the only possible factor for slow kinetics is a steric hindrance.

Table 3. Surface areas, pore sizes and pore volumes of SUM-100 series MOFs (according to Microactive software).

MOF	N_2 based measure			Ar based measure		
	SSA ($m^2\ g^{-1}$)	Pore volume ($cm^3\ g^{-1}$)	Pore diameter (Å)	SSA ($m^2\ g^{-1}$)	Pore volume ($cm^3\ g^{-1}$)	Pore diameter (Å)
SUM-102	870	0.45	9.8	846	-	7.1
SUM-103	1058	0.43	9.2	1016	-	6.8
SUM-104	385	-	-	371	-	-

The possible adaptation of the spatial arrangement within the pores due to the flexibility of these chains to optimize intermolecular interactions could be an explanation for this phenomenon.

Based on N_2 adsorption-desorption experiments, pore width of the different MOFs were calculated based on adsorption values (Micoactive software). The micropore size of SUM-102 is equal to 9.8 Å, whilst the size diminished to 9.2 Å for SUM-103. As the adsorption pattern of SUM-104 is rather "weird", its pore size distribution looked also "weird". There are 2 types of pores, one centered at 9.5Å and several mesopores having ~2-4 nm in width.

Another interesting phenomenon could be observed during the textural properties analysis, without any satisfactory explanation so far. Indeed, a remarkable color change was observed. Generally, when copper paddlewheel-bearing MOFs are activated, the color changes from blue/green to violet, according to the loss of axial water molecules. This trend was observed for NOTT-101, UTSA-90 and SUM-102. However, for SUM-103 and SUM-104 color changed from blue to deep blue (navy blue). Such kinds of color changes are also observed throughout the literature. Even for the same HKUST-1, there are some reports about navy-blue [9] and violet [10] colors after the activation. But in all cases, the explanation is the same: removal of the covalently bonded water molecules, which influenced d-d transitions of copper ions.

2) Synthesis and characterization of SUM-200 (Ni@H4L) series

Nickel-based MOFs are generally prepared for their catalytic properties [11]. Some of them were also used for CO_2 adsorption, such as Ni-MOF-74 [12]. In this Thesis, we have obtained new nickel MOFs with both, new and "old" ligands. MOFs were obtained again according to the solvothermal process using a DMA/methanol mixture. Despite their homogeneous size and shape, the diffraction of those crystals remained small. Even more crystalline samples, yielding beautiful crystals (Figure 26 left) led to wide diffractions with small intensity peaks under PXRD. However, for Ni@H4L1 (SUM-201) SCXRD could be obtained to solve the structure (Figure 26 right). Though side chains could not be observed, the structure resolution gave numerous information about the topology. It has a cubic structure with nearly 35 Å cell length. The largest pore diameters are around 9.6 Å according to the structure. However, as side chains cannot be observed the real (accessible) diameter will be less. Nickel atoms are six-coordinated with two water molecules at axial positions. Interestingly one of the oxygen atoms of the carboxylate group is not coordinated.

The 3D nickel MOFs are named SUM-200 (Ni@H4L), SUM-201 (Ni@H4L1), SUM-202 (Ni@H4L2), SUM-203 (Ni@H4L3) and SUM-204 (Ni@H4L4).

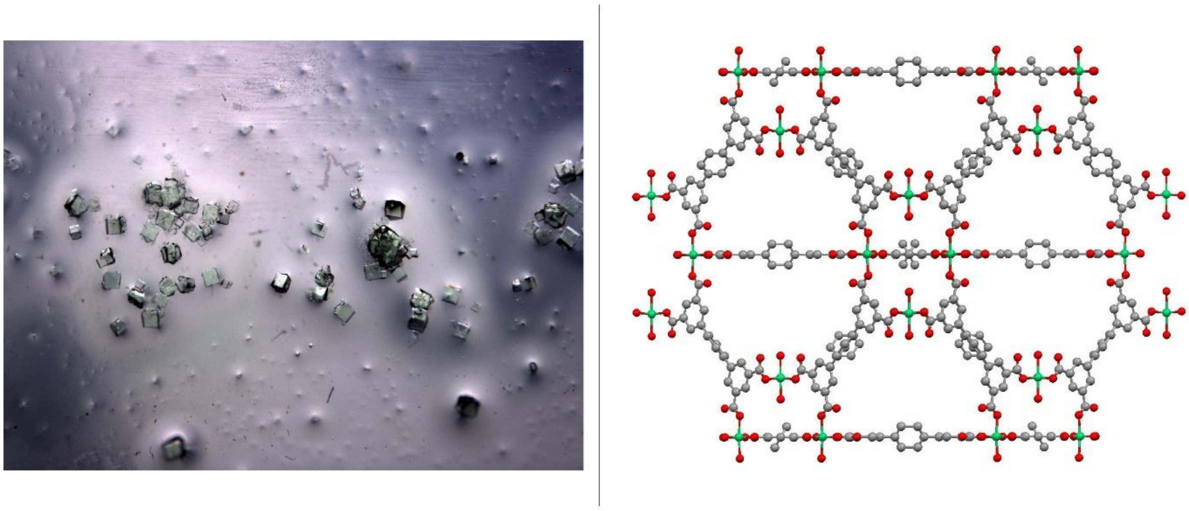

Figure 26. Left- Crystals of SUM-203 (Ni@H4L3); Right-Porosity of 3D SUM-201 (side chains not observed).

As already observed for their Cu@HxLy counterparts, SUM-203 and SUM-204 possessing larger side chains were also found stable in water (Figure 27 left). However, the stability remained lower than SUM-103 (Cu@H4L3). For example, SUM-103 was stable even after being put into water after activation. SUM-203 and 204 were stable in water but dissolved after activation if placed in water. Also, the emerald-green transparent crystals of nickel MOFs became non-transparent and clear-green in contact with water.

In these SUM-200s series, the nickel cation is hexa-coordinated in a square bipyramidal configuration. Like in copper MOFs, two water molecules coordinated in axial positions and the overall crystal system was cubic. Among these MOFs, only SUM-200 could be obtained as a powder. From SCXRD and PXRD, a new MOF and not a salt (or something else) has been undoubtedly obtained. However, FT-IR analysis was used to confirm the incorporation of the ligand (Figure 27 right).

Since the SUM-200 sample was the only MOF obtained as a powder, we had doubts about whether this phase was pure or not. Indeed, a supplementary vibration could be detected in the FT-IR spectrum around 1700 cm^{-1}, which is not observed for other MOFs. This peak corresponds to C=O stretching vibration which is observed in protonated ligands. However, even in deprotonated form H4L ligand exhibits this vibration (the analysis was performed with protonated and deprotonated forms of the H4L ligand). Therefore, it is specific to this ligand and not linked to the presence of an impurity.

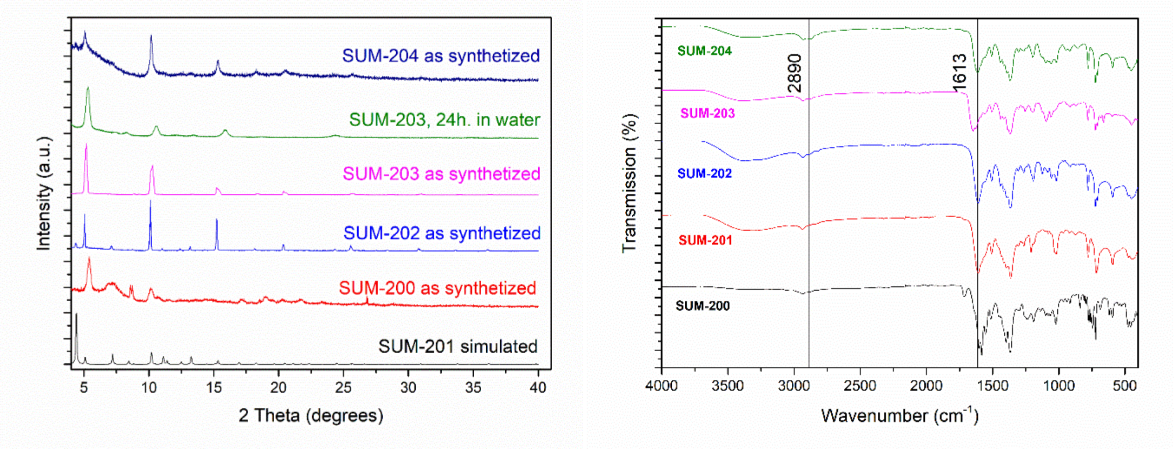

Figure 27. Left-PXRD; Right- FT-IR spectra of SUM-200 series MOFs.

Again, the peaks of side chains (2890 cm^{-1}) were observed as well as the coordination of carboxylic groups (1613 cm^{-1}).

All the crystals of the SUM-200 series were green, transparent, cubic and homogenous (except SUM-200).

The TGA analysis showed nearly the same decomposition temperature for the SUM-200 up to the SUM-204 series (Figure 28). However, the evaporation of solvent molecules happened at different temperatures. For some, it finished around 200°C, for others, it continued up to MOF decomposition. This could be related to host-guest interactions. From SCXRD analysis, we know that pores of the SUM-200s are small and decorated with large side chains, which for example can create hydrogen bonding with methanol molecules. Therefore, MOFs with an optimal size/interaction with DMA (maybe methanol) molecules made them difficult to leave the pores. From TGA analysis (indirectly), we can assume that SUM-201 has a higher size/interaction for capturing DMA (or same-sized) molecules.

The degradation of SUM-200 began nearly at 375^{o}C, for others this temperature is around 350^{o}C. Glyme chains may decrease the degradation temperature. We can do a comparison with the SUM-100 series. Where the degradation temperature of the NOTT-101 (without side chain) is slightly higher (around 10^{o}C) than others. Thus, the presence of the side chains decreased slightly the degradation temperature of the MOFs, but not significantly.

After TGA analysis, an interesting phenomenon could be observed. After calcination at 600^{o}C, the MOFs preserved their morphology. It means, they were still cubic, but their color turned to black.

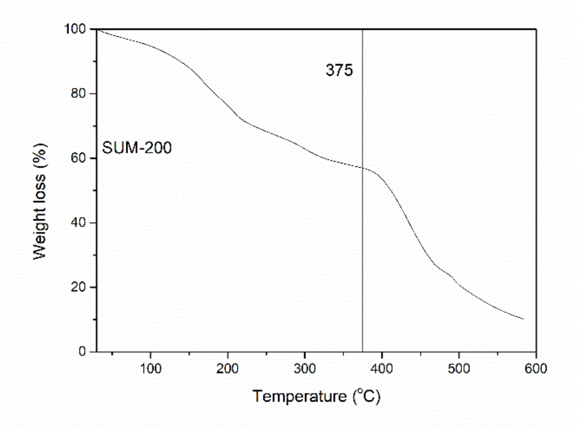

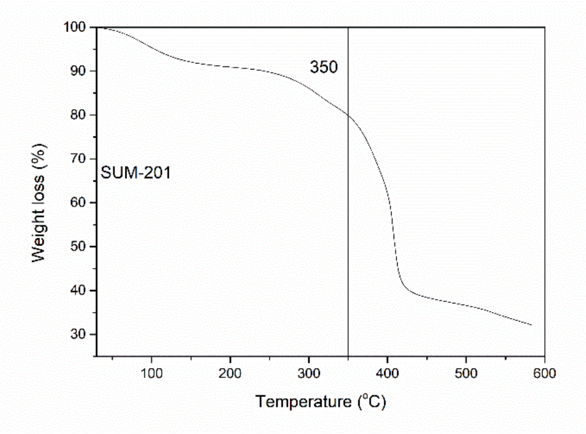

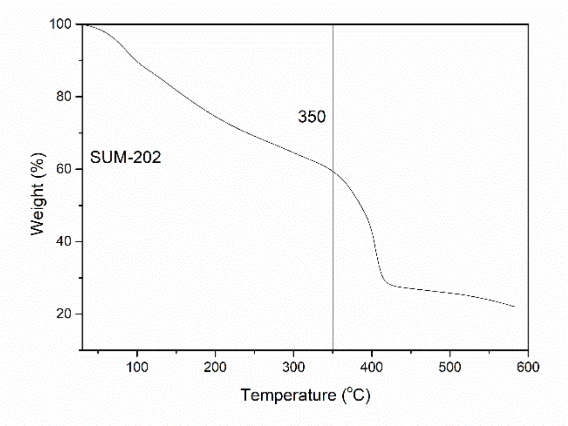

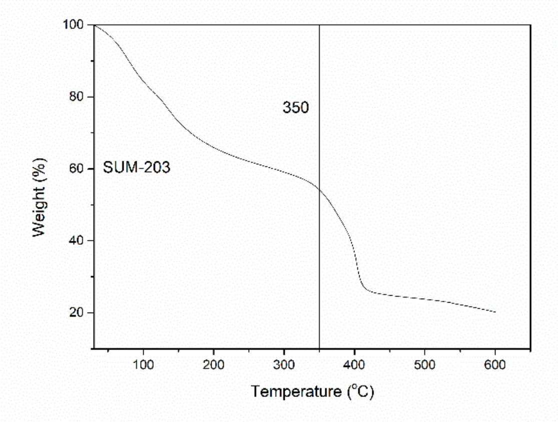

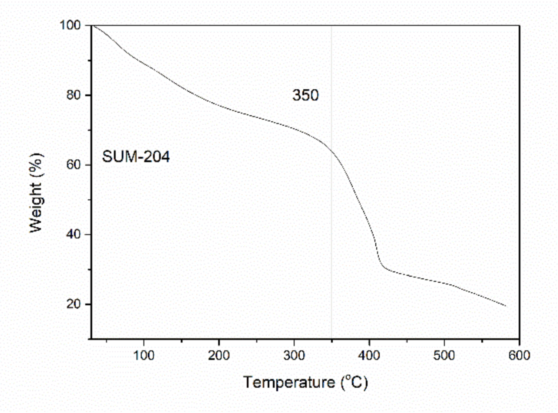

Figure 28. TGA profiles of SUM-200 series MOFs.

It made us think that in their micro/nano form they may also preserve the same morphology. PXRD pattern assessed the presence of a diffraction peak at 37,3°, corresponding to nickel oxide. In the literature, numerous examples of porous materials could be found based on the calcination of MOFs [13]. This inspired us to perform nitrogen adsorption-desorption analysis of this calcined form.

For BET analyses MOFs were activated at the same conditions that copper MOFs (160°C, 8 h). During the activation process, axial water molecules were evaporated, which demonstrated a color change from green to orange. However, none of the nickel MOFs, including calcined SUM-203, exhibited significant surface area.

3) Synthesis and characterization of SUM-300 (Ca@H4L) series

During the last decades, the use of MOFs in biological applications increased significantly. They were used in a wide range of domains, such as bio-sensing, bio-imaging, disease treatment, drug delivery, etc. [14]. It is clear that for biological applications MOFs should be biocompatible and non-toxic. As one of the tectons of the MOF is a metal ion, it should be non-toxic. For this reason, the use of Ca as a metal is really promising. It exists in our bones, nails, teeth, etc. Besides, calcium is an abundant and therefore cheap metal.

Likewise, for copper and nickel MOFs, a series of Ca-based MOFs could be obtained. Their nomenclature was defined as follows: SUM-302 (Ca@H4L2), SUM-303 (Ca@H4L3), SUM-304 (Ca@H4L4). Despite suitable crystal sizes, their diffractions were weak to completely analyze them. We obtained "some" SCXRD but the only information we can take from this is that it confirms the presence of calcium and the ligand in the crystal. It is the only information that we can gather from the structure. Even simulated SCXRD data did not match with PXRD. In Figure 29, the PXRD of SUM-300s are given.

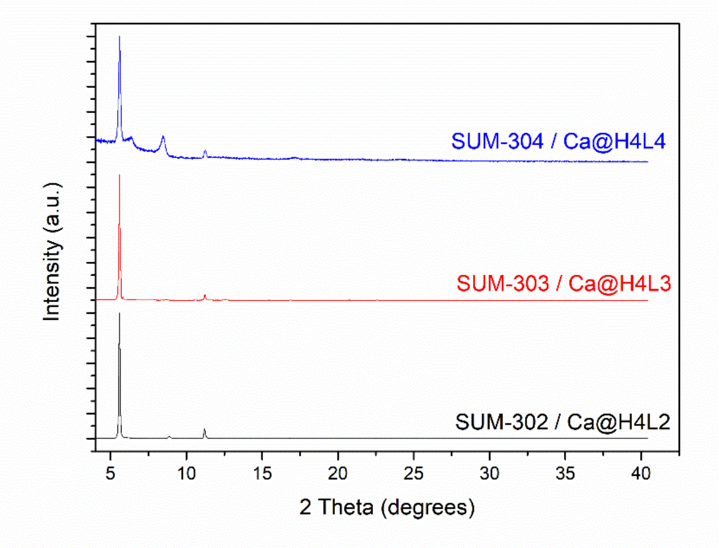

Figure 29. PXRD of SUM-300s.

TGA analysis was performed on SUM-302 and SUM-303 (Figure 30). As the H4L4 ligand was only synthesized at the end of my Ph.D. and its amount was small, all the analyses with SUM-304 could not be performed. TGA profiles of both MOFs are nearly the same. First up to 200°C, the solvent molecules were released from the structure, and later around 340-350°C MOFs began to collapse.

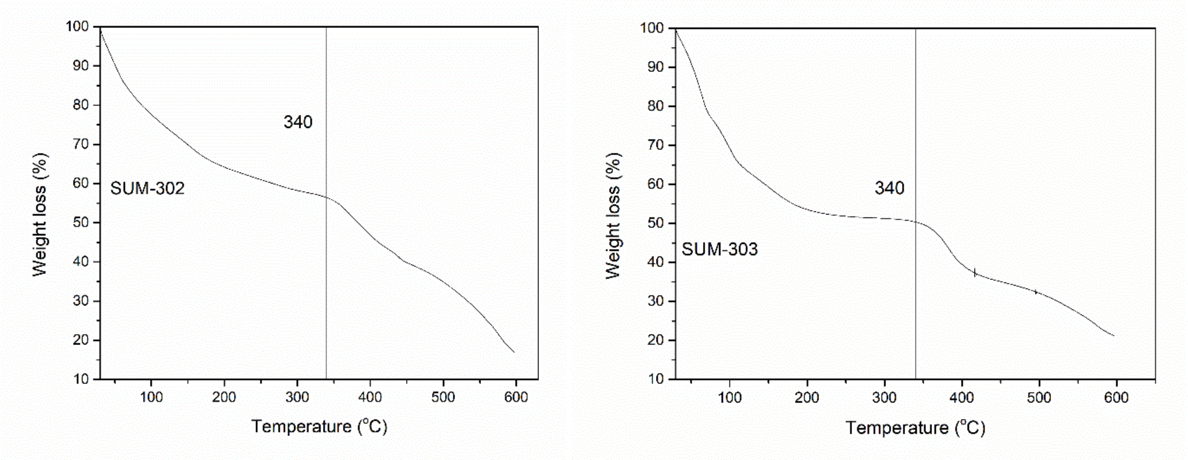

Figure 30. TGA of SUM-302 and SUM-303.

Despite quite good thermostability, none of the MOFs were stable in water. The next analysis was the BET, but unfortunately, MOFs did not exhibit significant surface area.

4) Synthesis and characterization of SUM-401 (Mg@H4L1) and SUM-403 (Mg@H4L3@DMF)

Magnesium is another non-toxic and cheap metal. One of the famous MOFs is Mg-MOF-74 which is known for its high CO_2 adsorption capacity. In nature there are enzymes called carboxylases, their function is the fixation of the CO_2 and some of these enzymes possess Mg^{2+} as an active center [15]. With this metal, we managed to obtain two new MOFs: SUM-401 (Mg@H4L1) and SUM-403 (Mg@H4L3). Both of the MOFs were obtained via the same method: DMF solution of ligand and nitrate salt heated in the presence of the acid. However, their topologies are completely different.

In Figure 31, the pores along the b axis could be observed. In the case of SUM-401 the magnesium ion is six-coordinated and crystallized in a tetragonal system (I-4). However, due to limited diffraction the structure is not completely resolved. In the case of SUM-403, we have a crystal with the $C_{19}H_{23}MgNO_{8.50}$ formula and a monoclinic crystal system. In this case also metal is six-coordinated, two of which are occupied by DMF molecules. It is noteworthy that the crystals obtained during the synthesis were homogenous.

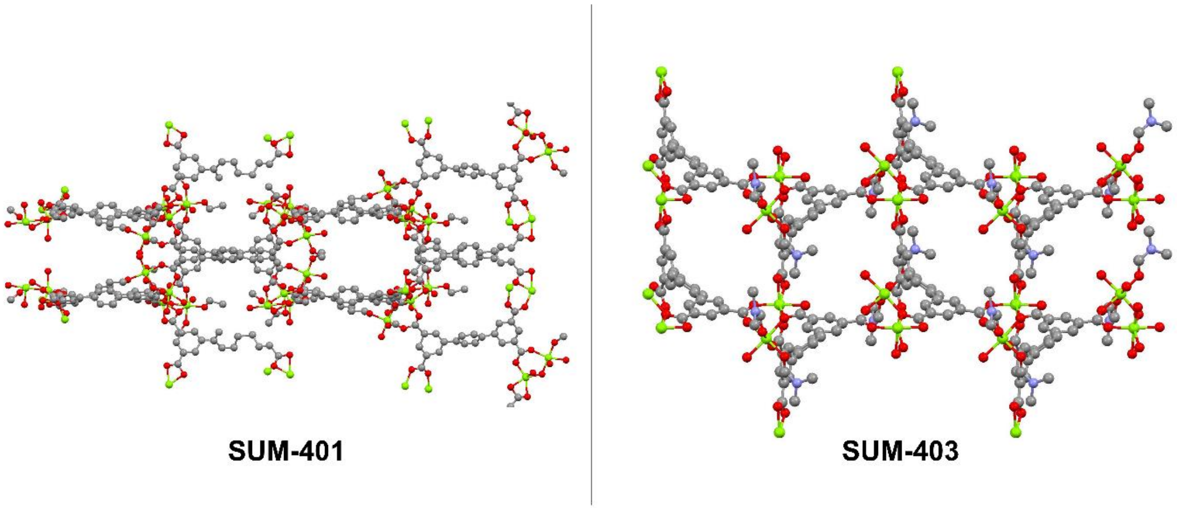

Figure 31. View from b-axis. The side chains were suppressed for better visualization of pores.

The comparative FT-IR spectra show the presence of the ligand in the MOF. Also, a shift around 1700 cm^{-1} is an indicator of the coordination of carboxylic groups (Figure 32).

Later, the thermostability of the MOFs was checked. They were heated up to 450°C under a nitrogen atmosphere (Figure 33).

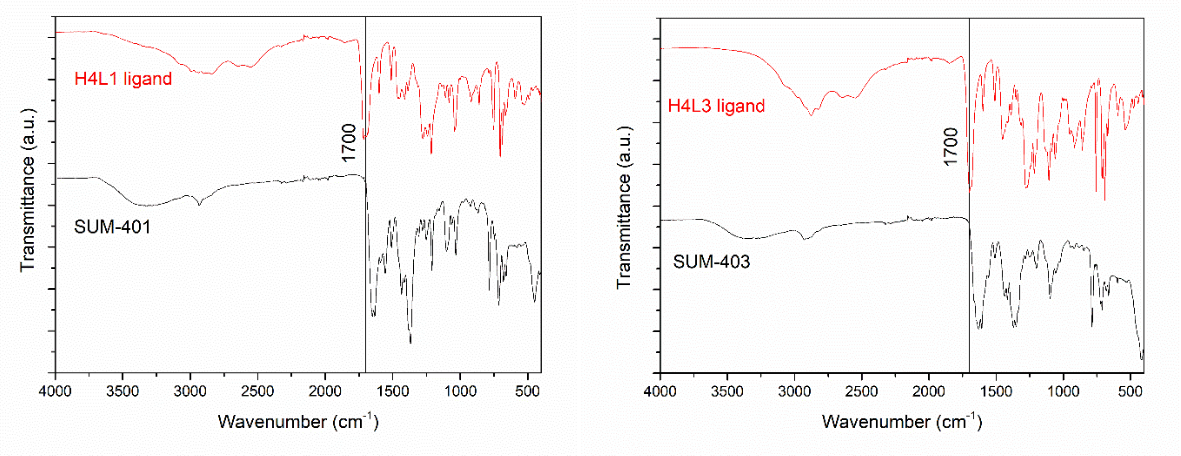

Figure 32. Comparative FT-IR spectra of SUM-401 and SUM-403 MOFs and their corresponding ligands.

As both MOFs were prepared in the same conditions (same solvents), first there is an evaporation step up to 200°C. Later, SUM-401 began to lose its structure around 400°C and SUM-403 at 333°C. Despite quite elevated thermal stability, none of the MOFs remained stable in water.

As usual for other MOFs, we tried to perform BET analyses, but unfortunately, none of the MOFs showed a surface area, like in nickel and calcium MOF cases.

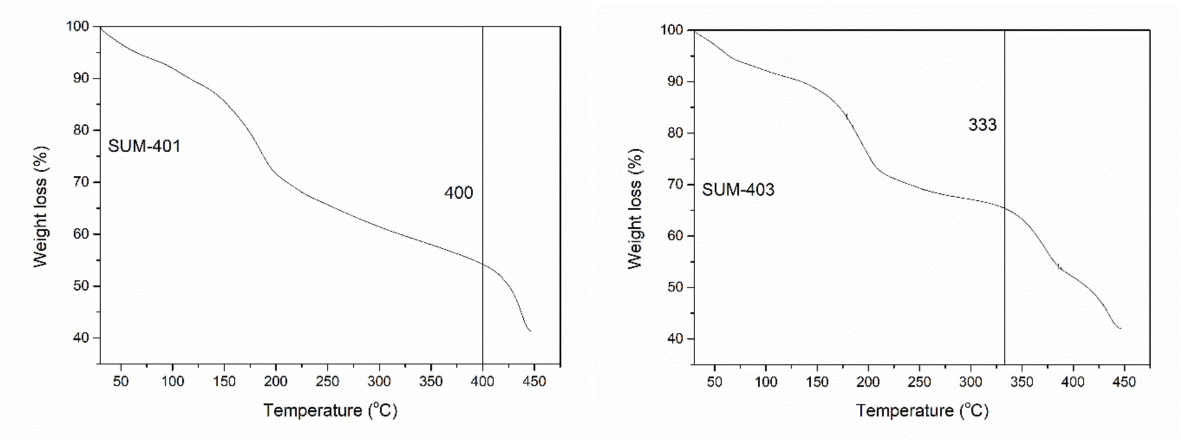

Figure 33. TGA profiles of SUM-401 and SUM-403.

III. New model ligands

1) Synthesis and characterization of LBM-10 (Cu@H4LOMe) and LBM-20 (Cu@H4LOH@pyridine)

In the introduction section, we discussed the importance to synthesize new MOFs, thus new families of ligands. As expected with those ligands, discussed in previous sections, original structures were able to form. Herein, new ligands, with only a small difference in their composition, changing methoxy to hydroxyl, were synthesized to investigate the possible changes in the coordination, hence generating new MOFs. Again, copper was selected as a basis for the metal node.

Cu@H4LOMe (LBM-10, LBM stands for Le Bel Materials) was obtained in solvothermal conditions, similar to other SUM-100 series. The ligand H4LOMe is an isomer of the H4L1 ligand. Therefore, it is logical to compare the MOFs of both ligands and to see the influence of the replacement of the methoxy group on the different parameters of the MOFs. First of all, we succeeded in synthesizing crystals with an appropriate size for SCXRD evaluation. Indeed, a publishable structure was obtained which confirms the presence of the methoxy groups. Despite copper being coordinated as a paddlewheel, like in UTSA-90 (Cu@H4L1), different angles and torsions render the MOF topology completely distinct (Figure 34).

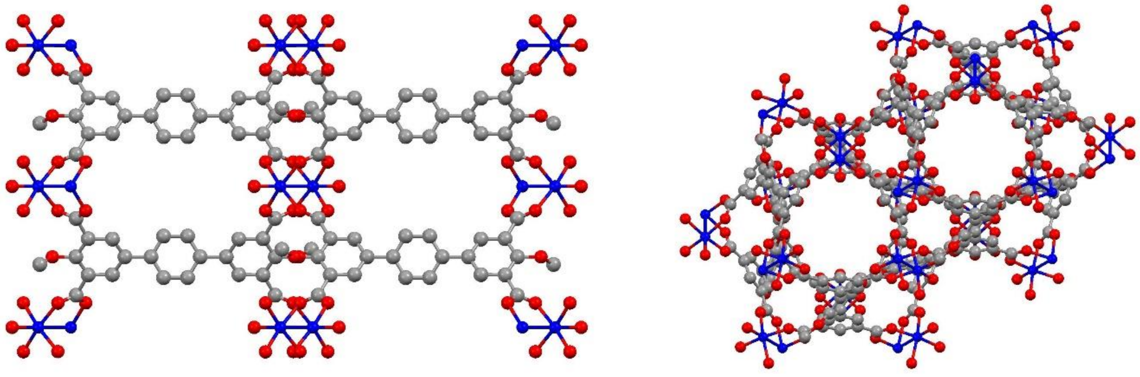

Figure 34. View from c-axis. Left-LBM-10, right- UTSA-90.

The formula of LBM-10 was $C_{12}H_{10}CuO_7$ being self-assembled in an orthorhombic system. Remember that NOTT-101 and other isostructural MOFs (UTSA-90, SUM-102, SUM-103, and SUM-104) crystallized in a trigonal system with an R-3m space group.

The morphology of the crystals was evaluated by SEM (Figure 35). Like in the optical microscope images, the SEM micrographs confirmed the “oval-rose petal” shaped crystals.

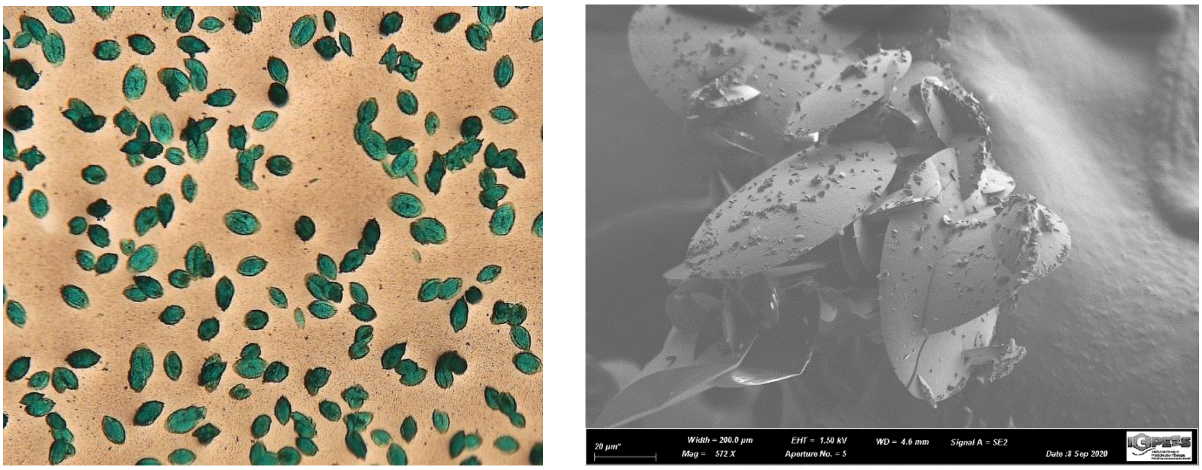

Figure 35. Macroscopic (left) and microscopic view of LBM-10 crystals.

The thermal stability of those beautiful “rose petal” crystals was evaluated by TGA. Like in NOTT type MOFs, first up to 250°C solvents molecules left the network and LBM-10 began to decompose around 300°C (Figure 36 left). Unfortunately, the MOF was not stable in water.

It was interesting to measure the surface area of the new MOF. LBM-10 activated under the same conditions as other MOFs, without solvent exchange at 160°C for 8 hours in a vacuum (Figure 36 right).

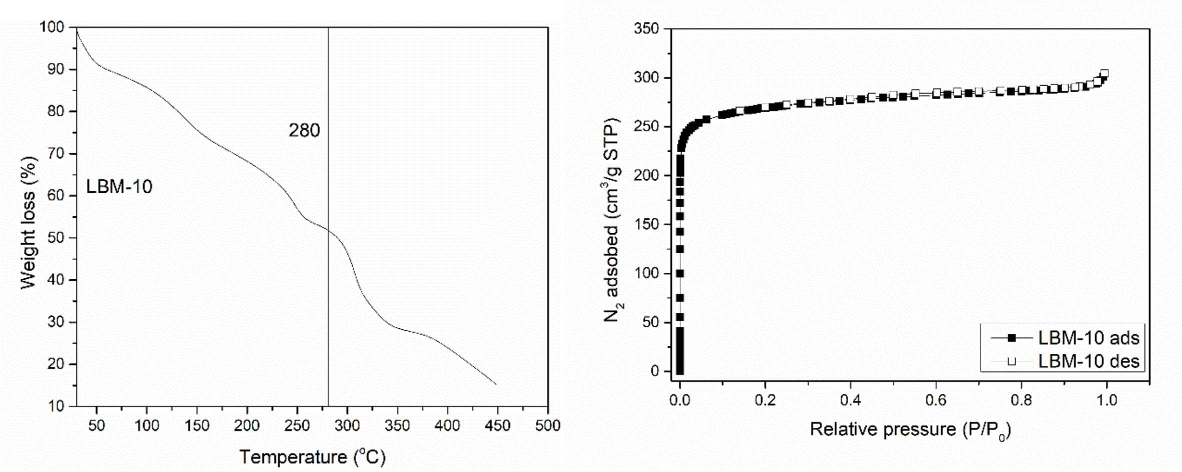

Figure 36. Left-TGA; Right- Nitrogen adsorption-desorption isotherm of LBM-10.

The BET surface area of LBM-10 was 863 m^2 g^{-1} based on N_2 adsorption and 875 m^2 g^{-1} based on Ar adsorption. The surface area of UTSA-90 (Cu@H4L1) was 1240 m^2 g^{-1}

and 1281 m^2 g^{-1}, measured from nitrogen and argon isotherms, respectively. As expected from SCXRD, the surface area was less than UTSA-90.

The next interesting novel material was the Cu MOF formed with the H4LOH ligand, which was named LBM-20. This is the sole MOF obtained by liquid-liquid diffusion described in the Thesis. The ligand was dissolved in pyridine and $Cu(NO_3)_2$ in methanol. After 24 hours, green crystals were formed. If the tube was left for more than 24 hours, blue crystals of copper with pyridine appear alongside green crystals. The green crystals were analyzed by SCXRD and their structure is shown in Figure 37.

LBM-20 crystallized in a tetragonal system and has the following chemical formula: $C_{47}H_{39}Cu_2N_5O_{12}$. Two of the four carboxylate groups are not coordinated. The Cu atom is coordinated to two pyridine moieties and two ligands via 3 Cu-O coordination bonds. Despite one uncoordinated carboxylate group and 2 capping pyridine molecules, LBM-20 exhibited a 3D structure. The crystals were not stable in the air. For this reason, no complementary analyses were performed.

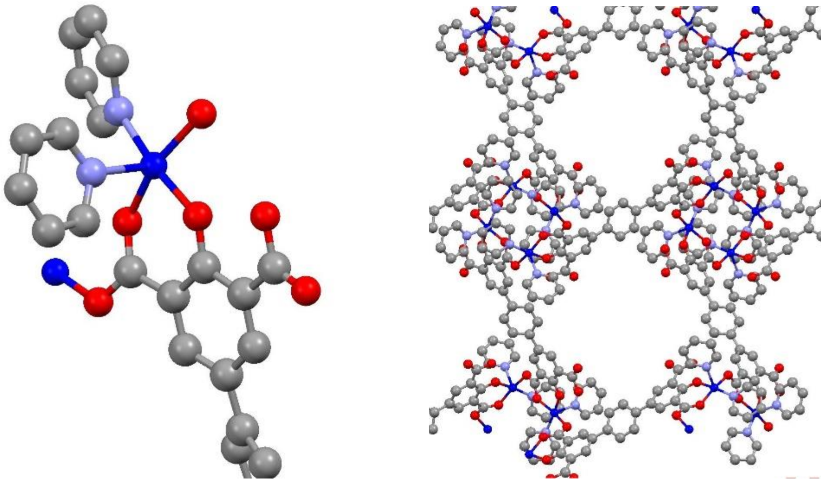

Figure 37. Left- connectivity of tectons; Right- porosity of the LBM-20, view from c-axis.

2) Synthesis and characterization of LBM-30 (Ca@H4LOMe) and LBM-40 (Ca@H4LOH@DMF)

Both MOFs were synthesized with the solvothermal method in a mixture of DMF/water. However, as the coordination abilities of the ligands were completely different, they yielded different MOF structures. Namely, LBM-30 (Ca@H4LOMe) and LBM-40 (Ca@H4LOH) were characterized by SCXRD (Figure 38). LBM-30 shows a curious structure. The first interesting thing is that oxygen of the methoxy group is also coordinated to calcium and one of the oxygen on each side of the ligand is not coordinated to anything. The network is 2 dimensional and composed of bi-layers in which two ligands appear to be stacked and associated at their ends by calcium ions. LBM-30 has a chemical formula $C_{24}H_{14}Ca_2O_{20}$ and is crystallized in a triclinic system P-1 space group. According to the crystal structure report there are 2 types of Calcium one coordinated with 7 and the last one with 8 oxygens. However, it's difficult to say rather the calcium is 7 coordinated or there is an error in the structure due to the high R factor. Ca-O distance for calcium and carboxylate group oxygen is between 2,36-2,48 Å. For Calcium and oxygen of the methoxy group the distance is between 2,5-2,6 Å. The distance between Calcium and oxygen of the water is around 2,4 Å. All these distances correspond well for 8 coordinated Calcium ion [16]. LBM-30 was stable in air, but not in water.

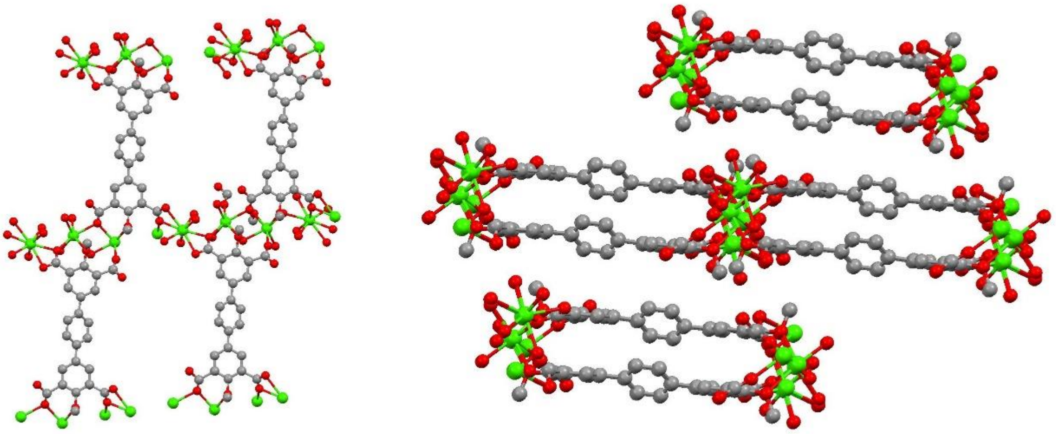

Figure 38. Left-view from a axis ; Right-view from b axis LBM-30

Later FT-IR and TGA analyses were also performed as presented in Figure 39. In the TGA curve, three steps could be equally observed. First, up to 80°C, 60% of the mass was lost. Most probably, it is related to water molecules observable in the unit cell. Later, the second wave (destruction of the structure) started to happen around 270°C.

Despite the MOF being only bidimensional, N_2 adsorption analysis was done; unfortunately, the material did not show significant surface area.

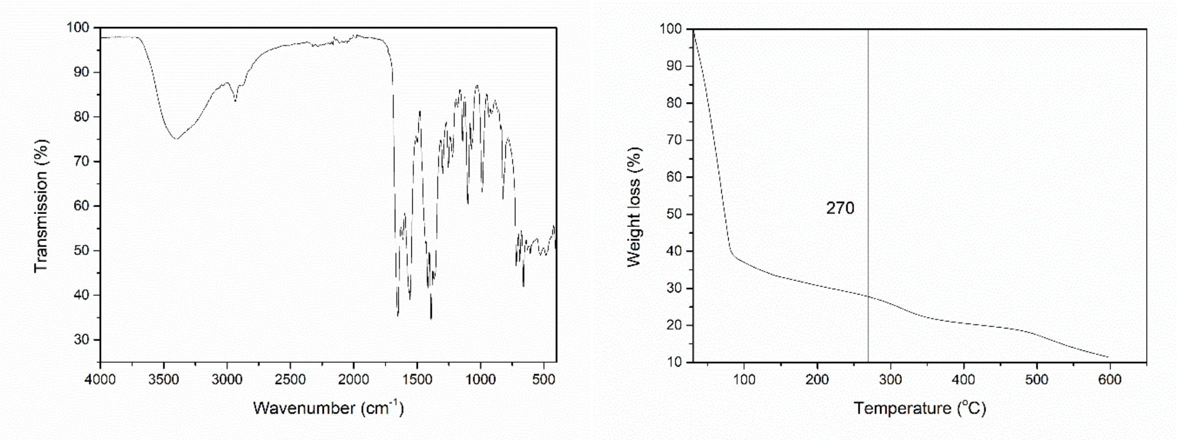

Figure 39. Left- FT-IR; Right- TGA of LBM-30.

Suitable sized single crystals were also grown for LBM-40 (Ca@H4LOH). At first glance, the structure exhibited a 3D network. However, while carefully looking, it was confirmed that was a bi-dimensional structure. This time calcium is 7 coordinated, two of them are DMF molecules and one of the oxygens of 2 carboxylic groups (from each side) is free (Figure 40).

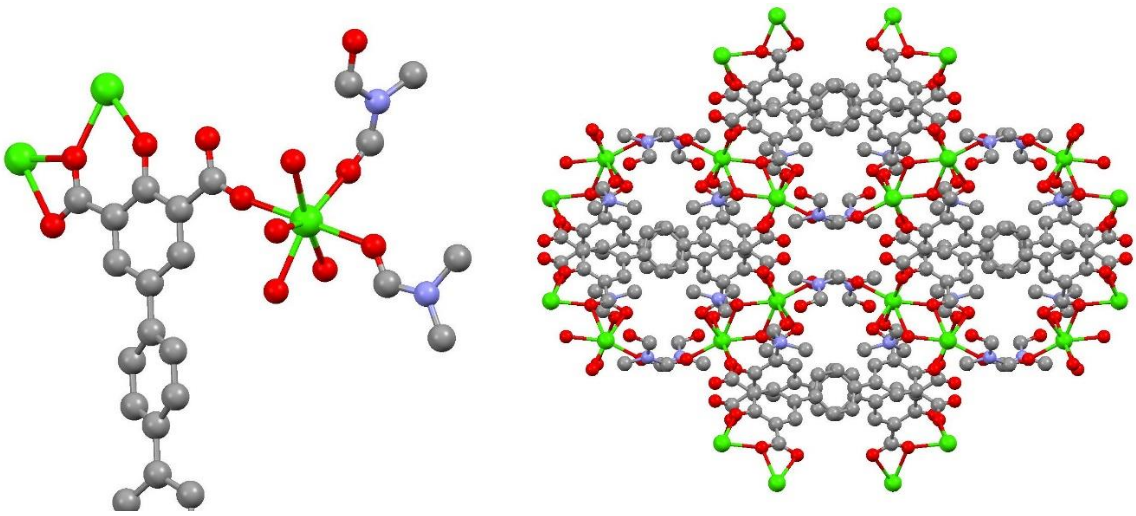

Figure 40. Left- coordination mode; Right- view from c-axis of LBM-40.

However, we observed another interesting phenomenon. For example, simulated data and PXRD data did not match. The synthesis was repeated three times and each time it did not match. It is possible that several phases were formed, or that the structure changed in the air. Another interesting observation was made while putting the MOF into water. Surprisingly, it did not dissolve in water.

After we filtered and performed PXRD analysis (Figure 41). However, this time another phase was also formed. Unfortunately, after placing the crystals in water, they turned like powder and SCXRD analysis could not be done.

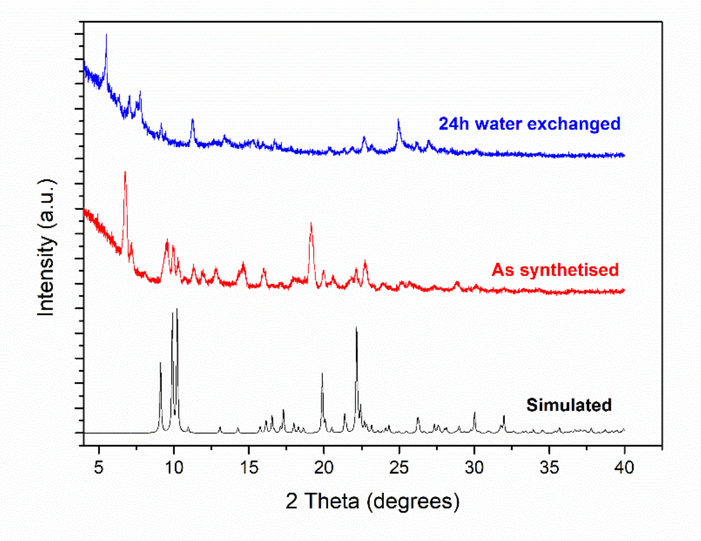

Figure 41. PXRD of LBM-40.

As we were not able to decipher the structure by SCXRD and to determine whether new phases were obtained, TGA analysis was undertaken (Figure 42). Hence, "as-synthetized" and "water-exchanged" versions of LBM-40 were tested.

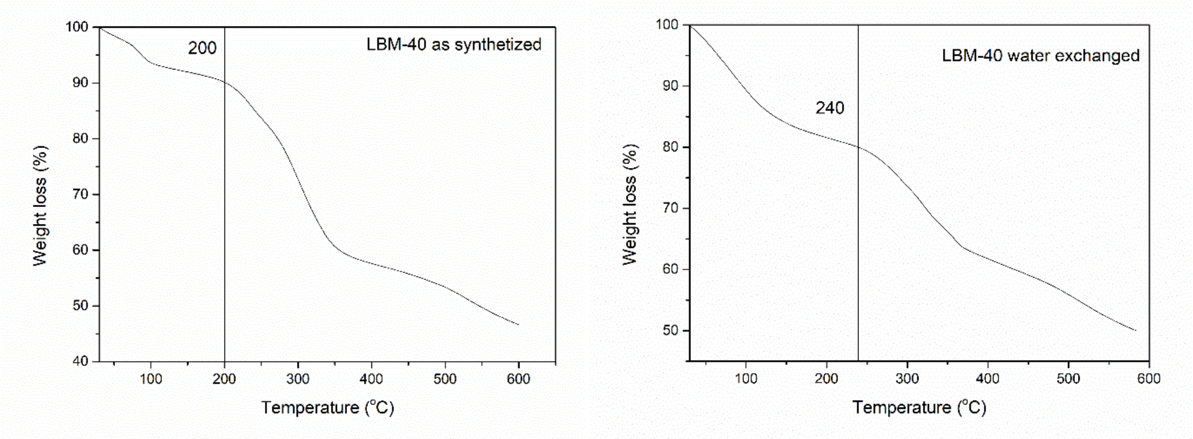

Figure 42. TGA profiles of different phases of LBM-40.

It is seen that the degradation temperature shifted from nearly 200°C to 240°C. Also, the first wave corresponding to evaporation is different. In the "as-synthetized" phase MOF lost around 10% of the mass up to its degradation. The loss for the "water-exchanged" phase was approximately double (20%). Most probably, during water immersion, the latter molecules replaced the DMF molecules but it did not lead to the destruction of the network.

3) Synthesis and characterization of LBM-50 (Zn@H4LOMe).

The last MOF with new model ligands is the MOF based on Zn and H4LOMe ligand, which was named LBM-50. For LBM-50, a suitable size of the crystals was grown, thus rendering it possible to analyze them. As the synthesis was performed solvothermally in the presence of 1-methylimidazole, a mixed ligand one-dimensional MOF was formed. Two 1-methylimidazole molecules capped one zinc ion. LBM-50 has $C_{43}H_{45}N_{9}O_{11}Zn_{2}$ chemical formula and is being self-assembled in a triclinic system at the P-1 space group (Figure 43). Like in previous MOFs, one oxygen atom of each acid group was not coordinated.

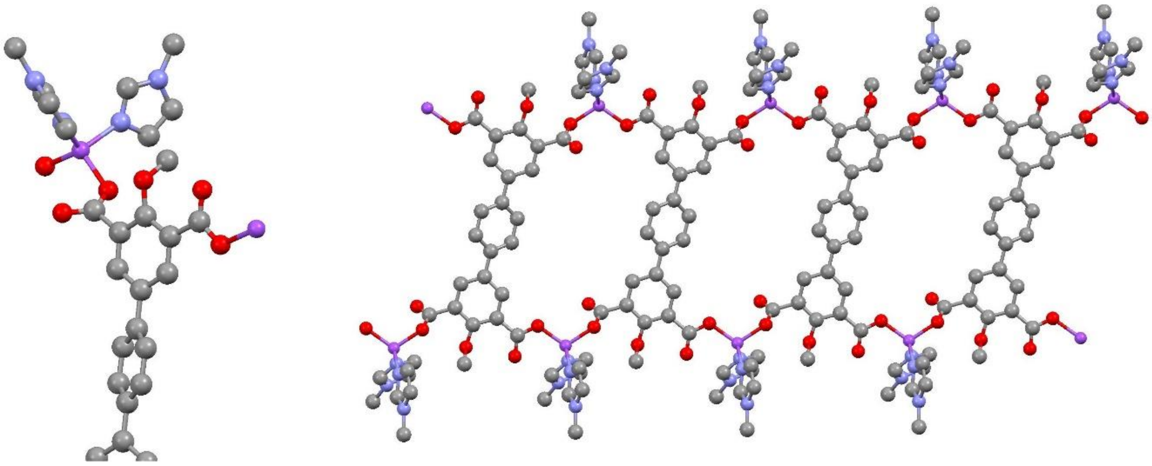

Figure 43. Left-coordination mode; Right- 1D view of LBM-50.

Again the MOF was stable in air but not in water. Since LBM-50 was unidimensional, thus diminishing the field of application, only TGA analysis was done for this MOF (Figure 44). The solvent evaporation occurred up to 150°C. This temperature is close to the boiling point of DMF. As MOF is unidimensional, DMF molecules are easily evaporated, in contrast to previous MOFs for which DMF evaporated up to 300°C. Finally, LBM-50 began to collapse around 230°C.

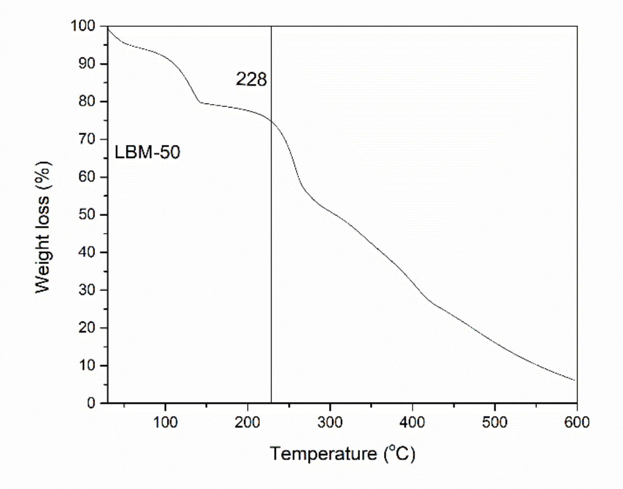

Figure 44. TGA profile of LBM-50.

IV.Dicarboxylic acids

1) Synthesis and crystal structure of SUM-552 (Zn@H2L2@bipy), SUM-503 (Zn@H2L3), and SUM-603 (Zr@H2L3).

The success of glyme modified tetracarboxylic ligand based MOFs (we will talk about it in chapter III) motivated us to synthesize the dicarboxylic version of the ligands and make their MOFs. Indeed, the possibilities of applying supramolecular recognition processes within MOFs deserve to be studied in different systems to evaluate the scope of our approach. As the synthesis of these ligands was performed in the last year of my thesis there are not a lot of MOFs with them.

The first MOF obtained was with zinc and H2L3 ligand, which was named SUM-503. It was prepared according to the solvothermal method in DMF. Again suitable-sized crystals were synthesized, but the SCXRD data was not publishable (Figure 45). However, we can deduce some information from it.

It is expected that such dicarboxylic ligand-based MOFs should be isostructural to MOF-5. For example, Wöll *et al.* [17] obtained the same topology MOFs by elongating the ligand size by adding phenyl groups to terephthalic acid. In all those Zn MOFs self-assembled to paddlewheel SBU.

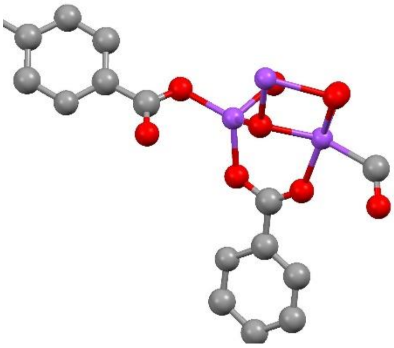

Figure 45. The connection mode of tectons in SUM-503.

However, in our case, half of the SBUs are a trinuclear zinc center and the other half are paddlewheel. Unfortunately, for the moment we were unable to get more information about its structure.

Another interesting MOF could be obtained with zinc, H2L2 ligand, and 4,4'-bipyridine (SUM-552). For SUM-552 suitable-sized crystals were synthesized and fully characterized by SCXRD (Figure 46), and even the side chains of the H2L2 ligand are observable. SUM-552 crystallized in a triclinic system.

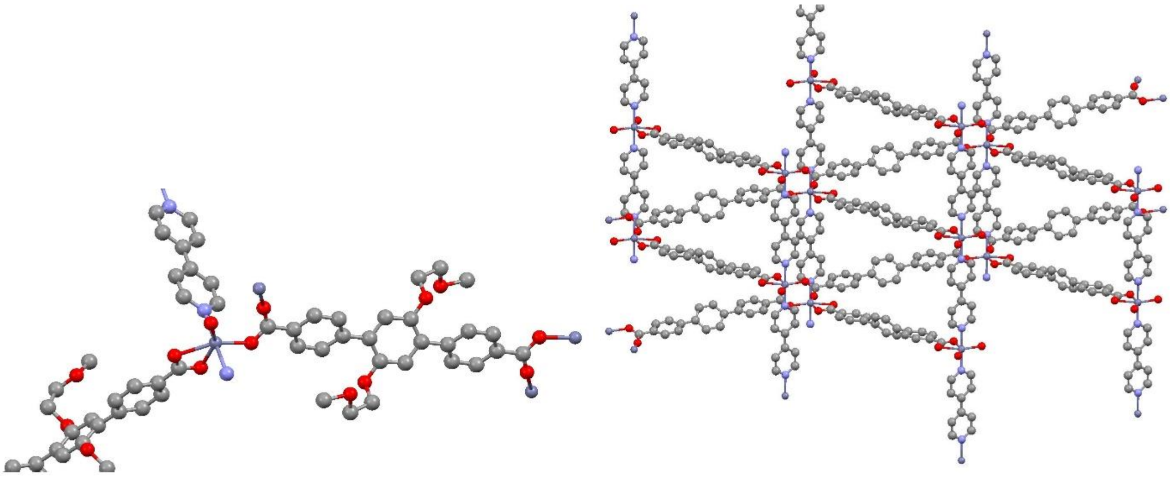

Figure 46. Above- connectivity of tectons; Below- view of the porosity of SUM-552. Side chains were erased for better visualization.

This time Zn atoms created paddlewheel like SBU but rather deformed with an elongated distance between zinc atoms. In "normal" paddlewheels distance between zinc atoms is nearly 3Å, but in the case of SUM-552, it is 4,166Å.

Finally, with diacid ligands, we tried to synthesize analogs of UiO-68. In similar conditions in the presence of benzoic acid as a modulator, single crystals of Zr@H2L3, named SUM-603, were grown. Unfortunately, SCXRD showed only zirconium SBU of the MOF. But cell parameters are coherent with the fact that it is analog to UiO-68. Also, PXRD data matches well with simulated UiO-68 (Figure 47 left).

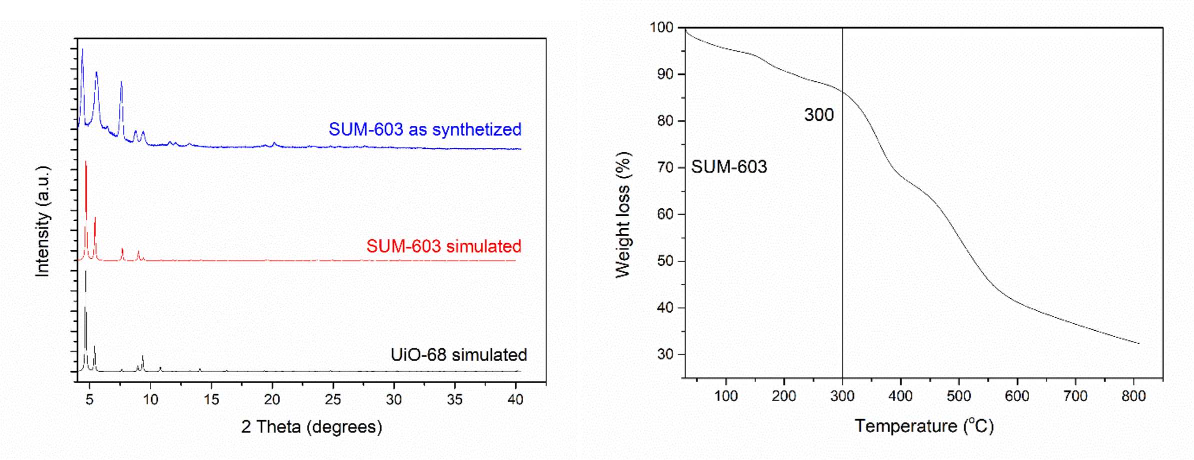

Figure 47. Left- PXRD of simulated and synthesized MOFs; Right-TGA of SUM-603.

TGA profile shows the beginning of structure degradation around 300°C, which appeared ~30-40°C less than UiO-68. The formation of zirconium MOF is very important from an application point of view since they usually exhibit high thermal and water stability.

V. Synthesis and characterization of MOF@SBA-15.

In line with their pristine form, most of the MOFs synthesized are microporous materials [18-20]. This could be a drawback for example in the conversion of bigger molecules. For this reason, MOFs were often modified pre-, or post-synthetically to create larger pore sizes, being of meso- or macroporous nature [21]. Another strategy to create hierarchical porosity in MOFs is while using templates, being either hard or soft. Also, hierarchically porous MOFs could be obtained by combining MOFs with macro- and/or mesoporous materials, such as carbon, silica, etc. [22]. Sometimes, the combination of these materials gave birth to increased stability of the MOFs, as they remained confined within another material [23].

In our experiments, several materials were screened and, in the end, the best candidate seemed to us SBA-15 mesoporous silica (Figure 48). It was found suitable and selected, thanks to its high thermal stability, uniformly distributed hexagonal mesopores (10-15 nm), and elevated surface area, *i.e;* 794 m^2 g^{-1} [23]. With SBA, organic-inorganic hybrids were prepared with the whole SUM-100 (Cu@H4L) series. But, as SUM-103 was stable and demonstrated good performance among all MOFs (chapter III), the detailed study was undertaken with SUM-103@SBA (Figure 48). We chose a different method to design an efficient hybrid. First, ethanol was added to a defined amount of SBA (10 mg) and $Cu(NO_3)_2$ (4.1 eq. vs ligand). They were ultrasonicated for 3 min for better dispersion. Later, they were put on a heating plate at 60°C and after evaporation of all the solvent, a blue homogenous powder was obtained. The next step was the same synthesis of the MOF, with the addition of solvents, acid and ligand (10 mg), and put it on the heater at 85°C. After 24 hours, the mixture was filtered and dried in the air, leaving a blue and highly homogenous powder (Figure 48).

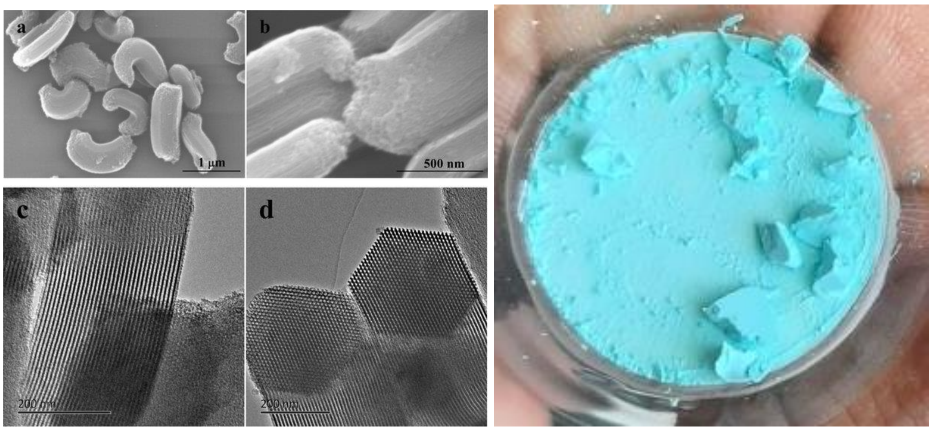

Figure 48. SBA-15 (left); SUM-103@SBA after (right) drying.

It is worth underlining that raw SBA-15 is white and SUM-103 is blue. With the help of PXRD and FT-IR, the incorporation of MOF inside SBA-15 could be assessed (Figure 49). Comparative spectra make it easy to observe the possible incorporation of the MOF. Two main peaks at 1070 cm^{-1} and 450 cm^{-1} of the SBA-15 appeared in the whole series.

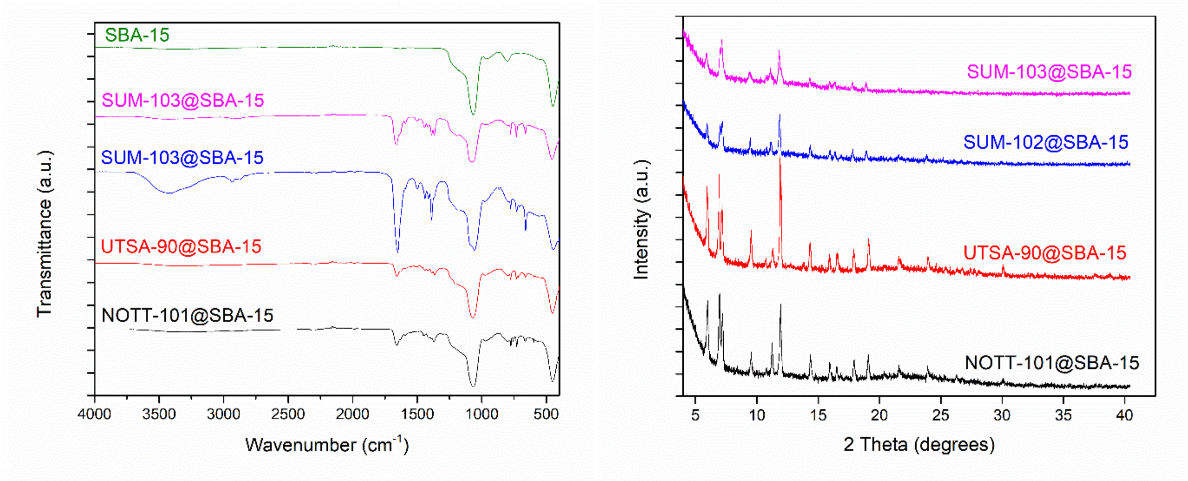

Figure 49. Left-FT-IR spectra of hybrids and SBA-15; Right- PXRD of hybrids.

TGA was also performed on hybrids (Figure 50).

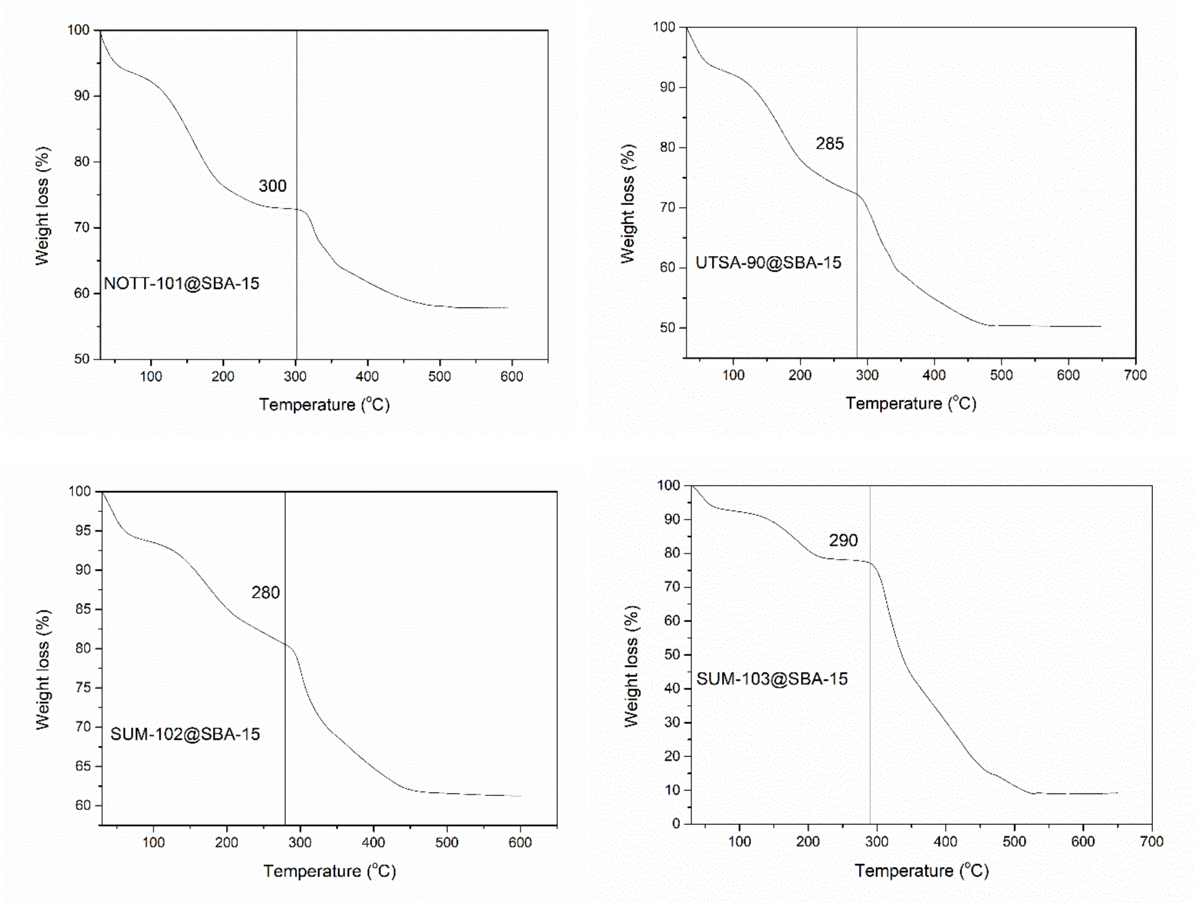

Figure 50. TGA of hybrids.

It is known that SBA-15 is mesoporous silica, being highly stable thermally, whilst MOFs began to degrade around 280-300°C. The syntheses of all hybrids were done with the same SBA / ligand ratio (10 mg/10 mg). However, from the TGA profiles, it appears that a higher content of MOF could be found in the SUM-103@SBA hybrid. Moreover, as the ligands were taken at 10 mg for each case, the molar quantity of the H4L3 was less than others. Also, from the synthesis of MOFs, we know that all the SUM-100 series have nearly the same yield between 45-55%. We can assume that silica support promotes the formation of the MOF with the H4L3 ligand.

In table 4, the weight percentages of MOF, SBA-15 and solvent in each hybrid are presented. All aforementioned analyses indirectly showed the MOF incorporation in the silica.

For direct observation of the hybrids by SEM (Figure 51), an elemental mapping of the elements was performed (Figure 52).

Table 4. Weight percentages of components of hybrids.

Name	Solvent (wt %)	MOF (wt %)	SBA-15 (wt %)
NOTT-101@SBA-15	27	16	57
UTSA-90@SBA-15	27	23	50
SUM-102@SBA-15	20	19	61
SUM-103@SBA-15	23	67	10

In Figure 51, we observe SBA-15 crystallites and MOF crystals around it. In addition, SBA-15 with its hexagonal homogenous pores could be observed in Figure 52.

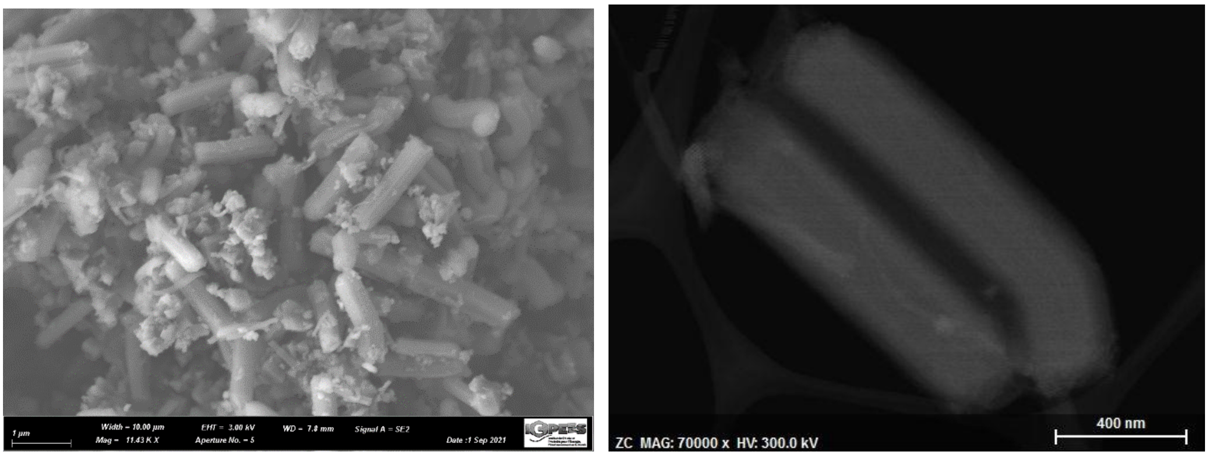

Figure 51. Left- SEM image of SUM-103@SBA-15; Right- TEM image of NOTT-101@SBA-15.

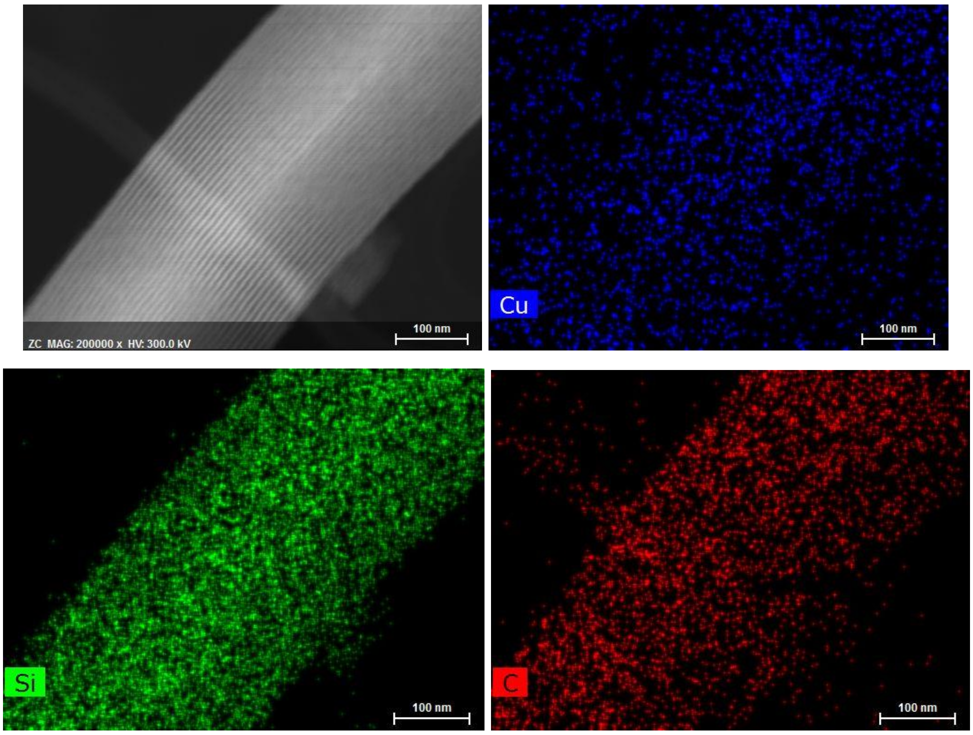

Figure 52. EDX mapping of UTSA-90@SBA-15.

Regarding the EDX mapping analysis, it is seen that Si and C elements location matches rather well. Since those elements are located at the same place, with only a small amount of C outside, it confirms that the MOF-SBA-15 hybrid structure formed.

VI.Conclusion

During the Thesis based on the 9 new ligands, 21 MOF and 4 hybrids were synthetized and characterized in depth. Among them, 4 MOFs are stable in water: 3 obtained with tetracarboxylic ligands and 1 with dicarboxylic ligands. Generally, MOFs are synthesized in series including from 2 to 5 MOFs. For example, the SUM-100 series was based on Cu, SUM-200 on Ni, SUM-300 on Ca, and SUM-400 on Mg. Among those 21 MOFs, a publishable SCXRD structure was obtained for 7 samples. Almost all MOFs were synthesized by the solvothermal method in the presence of DMF (at least).

Also, these ligands have a huge potential of generating new interesting MOFs. For example, with the H3LNO2 ligand, we have found 2 crystals, but for the moment they are not suitable for SCXRD. Also, beautiful but (too) small square-like crystals were produced with H4LOH and zirconium.

References

1. X. K. Matsuyama, *The Journal of Supercritical Fluids*, 2018, **134**, 197–203.
2. European patent, deposited, 22/12/2021, Synthesis of metal organic framework (MOF) materials with high adsorption capacity of organic compounds and CO2 capture, Nizami Israfilov, Benoît Louis, Jean-Marc Planeix, Submission number 1000505175, Application number EP21306902.4
3. N. Israfilov, K. Soukup, B. Louis and J.-M. Planeix, *New J. Chem.*, 2022, **46**, 8967–8970.
4. A. Becker, N. Israfilov, E. Ehrstein, I. Lara-Ibeas, J.-M. Planeix, B. Louis and S. Le Calvé, *Microporous and Mesoporous Materials*, 2022, **343**, 112136.
5. X. Lin, J. Jia, X. Zhao, K. M. Thomas, A. J. Blake, G. S. Walker, N. R. Champness, P. Hubberstey and M. Schröder, *Angew. Chem. Int. Ed.*, 2006, **45**, 7358–7364.
6. X. Lin, I. Telepeni, A. J. Blake, A. Dailly, C. M. Brown, J. M. Simmons, M. Zoppi, G. S. Walker, K. M. Thomas, T. J. Mays, P. Hubberstey, N. R. Champness and M. Schröder, *J. Am. Chem. Soc.*, 2009, **131**, 2159–2171.
7. T. A. Makal, X. Wang and H.-C. Zhou, *Crystal Growth & Design*, 2013, **13**, 4760–4768.
8. A. K. Kar and R. Srivastava, *New J. Chem.*, 2018, **42**, 9557–9567.
9. C. Prestipino, L. Regli, J. G. Vitillo, F. Bonino, A. Damin, C. Lamberti, A. Zecchina, P. L. Solari, K. O. Kongshaug and S. Bordiga, *Chem. Mater.*, 2006, **18**, 1337–1346.
10. N. Al-Janabi, P. Hill, L. Torrente-Murciano, A. Garforth, P. Gorgojo, F. Siperstein and X. Fan, *Chemical Engineering Journal*, 2015, **281**, 669–677.
11. U. S. F. Arrozi, V. Bon, C. Kutzscher, I. Senkovska and S. Kaskel, *Dalton Trans.*, 2019, **48**, 3415–3421.
12. A. H. Harandizadeh, S. Aghamiri, M. Hojjat, M. Ranjbar-Mohammadi and M. R. Talaie, *Nanomaterials*, 2022, **12**, 412.
13. Y. Yang, H. Dong, Y. Wang, C. He, Y. Wang and X. Zhang, *Journal of Solid State Chemistry*, 2018, **258**, 582–587.
14. H.-S. Wang, Y.-H. Wang and Y. Ding, *Nanoscale Adv.*, 2020, **2**, 3788–3797.
15. J. G. Vitillo, ***RSC Adv.***, 2015, **5**, 36192-36239.

16. A. K. Katz, J. P. Glusker, S. A. Beebe and C. W. Bock, *J. Am. Chem. Soc.*, 1996, **118**, 5752–5763.
17. J. Liu, B. Lukose, O. Shekhah, H. K. Arslan, P. Weidler, H. Gliemann, S. Bräse, S. Grosjean, A. Godt, X. Feng, K. Müllen, I.-B. Magdau, T. Heine and C. Wöll, *Sci Rep*, 2012, **2**, 921.
18. T. Devic, in *Metal-Organic Frameworks in Biomedical and Environmental Field*, eds. P. Horcajada Cortés and S. Rojas Macías, Springer International Publishing, Cham, 2021, pp. 111–154.
19. G. Férey, *Chem. Soc. Rev.*, 2008, **37**, 191–214.
20. J. Čejka, *Angewandte Chemie International Edition*, 2012, **51**, 4782–4783.
21. Z. Xiao, Y. Mei, S. Yuan, H. Mei, B. Xu, Y. Bao, L. Fan, W. Kang, F. Dai, R. Wang, L. Wang, S. Hu, D. Sun and H.-C. Zhou, *ACS Nano*, 2019, **13**, 7024–7030.
22. A. Sachse, R. Ameloot, B. Coq, F. Fajula, B. Coasne, D. De Vos and A. Galarneau, *Chem. Commun.*, 2012, **48**, 4749–4751.
23. M. Rocquin, M. Henrion, M.-G. Willinger, P. Bertani, M. J. Chetcuti, B. Louis and V. Ritleng, *Dalton Trans.*, 2014, **43**, 3722–3729.

Chapter III: Application of these new materials

Schematic of nomenclature of MOFs

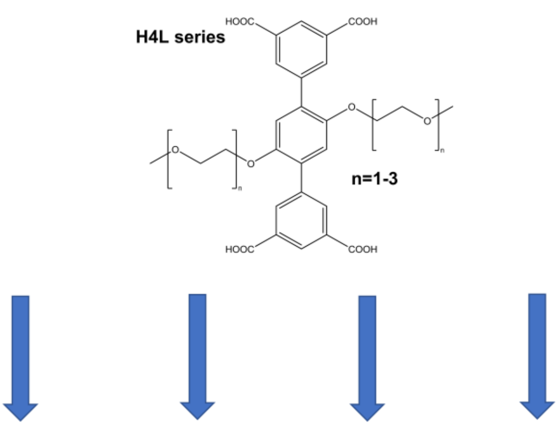

Cu²⁺
SUM-100 series
n=1 SUM-102
n=2 SUM-103
n=3 SUM-104

Ni²⁺
SUM-200 series
n=1 SUM-202
n=2 SUM-203
n=3 SUM-204

Ca²⁺
SUM-300 series
n=1 SUM-302
n=2 SUM-303
n=3 SUM-104

Mg²⁺
SUM-400 series
n=0 SUM-401
n=2 SUM-403 (with DMF)

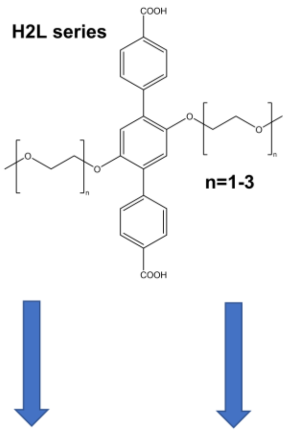

Zn²⁺
SUM-500 series
n=1 SUM-552 (with 4,4’ bipyridyl)
n=2 SUM-503

Zr²⁺
SUM-600 series
n=2 SUM-603

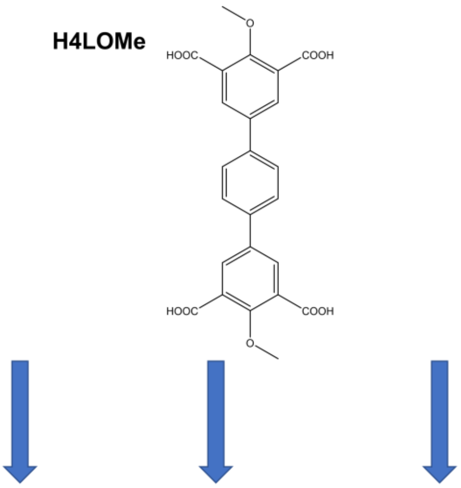

Cu²⁺
LBM-10

Ca²⁺
LBM-30

Zn²⁺
LBM-50
with methyl imidazole

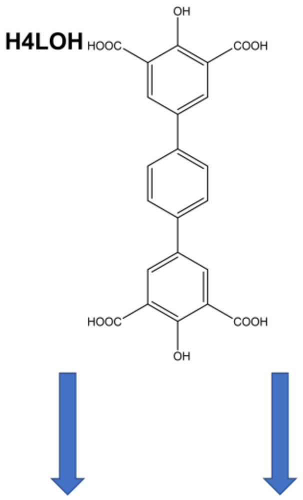

Cu²⁺
LBM-20
with pyridine

Ca²⁺
LBM-40
with DMF

I. Introduction

In this chapter, we will discuss different applications of our MOFs. The first part will be about dye adsorption of SUM-102 (Cu@H4L2) and SUM-103 (Cu@H4L3) in an aqueous environment. The example dyes will be methylene blue (cationic) and methyl orange (anionic). Later, the same MOFs will be used in formaldehyde adsorption by using synthetic air with 164 ppb HCOOH concentration.

Finally, the largest part of this chapter will be dedicated to CO_2 capture. We will see very interesting results. Especially, for SUM-103m (Cu@H4L3, with a smaller crystal size) we observed 3 different CO_2 adsorptions in 3 different countries with 3 different values.

Also, we tested more than 10 new MOFs for CO_2 adsorption. Later we will finish the chapter with a conclusion.

II. Dyes adsorption of SUM-102 (Cu@H4L2) and SUM-103 (Cu@H4L3)

In the previous chapter, we discussed the synthesis and characterization of the SUM-102 and SUM-103. Their stability in an aqueous environment and the presence of long amphiphilic branches made them an attractive candidate for the selective capture of guest molecules. Several glyme chains inside the cavity of the MOFs limit their degree of freedom, creating pseudo-crown ethers.

Strasbourg is the core of Supramolecular Chemistry thanks to the works of Jean-Marie Lehn and as mentioned in the introduction one of our main inspiration was highly selective compounds such as crown ethers and cryptands. Theoretically, inside the cavity long ethyleneoxy chains will behave like pseudo-crown ethers and outside of the cavity as podands.

Cryptands and related molecules were indeed used for metal ion adsorption [1]. However, to evaluate the potential of our SUM materials as a sorbent, we have selected a cationic organic molecule. In our study [2], methylene blue (MB) was chosen as a probe dye molecule. From one side, it is a cationic molecule, so oxygen-rich side chains may interact with MB. Secondly, the blue color with a high molar attenuation coefficient, thus rendering it easier the measure its adsorbance via UV-vis spectrophotometer. Thirdly, its molecular structure is similar to some anti-depressants (imipramine, desipramine), thus the better absorbance of MB by MOF could open a path for using MOFs for drug adsorption and/or delivery. Finally, MB is a dye, which is generally toxic to the environment and in some cases carcinogenic [3,4].

The tunable nature of the pores of the MOFs makes it possible to use them for dye removal. We use the term removal because adsorption is not the only way to eliminate the dye. There are other methods, like flocculation and photodegradation, etc.[5-8] The MOFs are generally applied in the adsorption and photodegradation part. To make it short, we will talk only in this chapter about the MOFs for the adsorption of MB.

In the literature, there are lots of examples of MOFs and MOF composites for MB adsorption. For example, Zhang *et al.* [9] used the famous HKUST-1 benchmark which was discussed earlier in this Thesis. The experiment was carried out with 5 mg of MOF in 10 ml MB solution at different concentrations, pH and temperature. After some defined time intervals, solutions were centrifuged and the adsorbance of the MB was measured via UV-vis spectrophotometer. At the end of the experiments, the best Langmuir adsorption was found at pH=7 and its value was nearly 5 mg g^{-1}.

In the study by Omar *et al.* [10], binary MOF- UiO-66/MIL-101(Fe) and its graphene oxide composite (COOH modified) were tested in MB adsorption. A batch experimental system similar to the previous one was performed. The only difference is that the adsorption was not static, MOF containing MB solution was agitated at 250 rpm. It is worth mentioning that separately the binary MOF and COOH-modified GO yielded a maximum adsorption capacity of 140 mg g^{-1} and 155 mg g^{-1}, respectively. The maximal adsorption achieved with the composite was 449 mg g^{-1}.

The best performance achieved with a MOF in MB adsorption was reported with an amino-modified MIL-101(Al) [11]. The modification with amino groups increased the electrostatic interaction and led to the reach of a Langmuir adsorption of 762 mg g^{-1}. It is worth mentioning that the non-modified MOF adsorbed only 195 mg g^{-1} of dye. Moreover, the amino-MIL-101(Al) adsorbed 185 mg g^{-1} of methyl orange (MO) (anionic dye). However, after MB adsorption on amino-MIL-101(Al) around 30% of Al was lost, yielding significant structural damages to the MOF. Surprisingly, this phenomenon could not be observed with MO.

Herein, nearly the same experiment was performed. The dye adsorption capacity of both MOFs was evaluated. In the case of SUM-103, both isothermal adsorption and kinetic studies were performed. The adsorption parameters have been determined in water (neutral pH) at 30 °C (for isothermal conditions). Before the adsorption tests, adsorbed DMF molecules were exchanged with water (24 h at room temperature). MOF was then filtered and dried under air for another 24 h.

Firstly, both SUM-102 and SUM-103 were compared under identical conditions. The values of dye adsorption, expressed in the percentage of dye solutions (10 mL; 10 mg L−1) over 3 mg MOF after 24 h and at 30 °C are given in Table 5.

Table 5. Adsorption of dyes *versus* MOFs sample (by wet% of dyes adsorbed over MOFs)

	SUM-102 (%)	**SUM-103 (%)**
Alizarin yellow R	64	77
Methylene blue	83	94

Those values show that methylene blue (MB) is more efficiently adsorbed than alizarin yellow R. Likewise, a significant increase in adsorption was observed while increasing the side chain length. The study of the adsorption of MB on SUM-103 was extended by performing measurements of isothermal adsorption capacity and a kinetic study, detailed in the experimental section. The adsorption protocol was carried out using the batch method by adding 20, 50, 100 and 200 ppm methylene blue aqueous solutions over 3 mg MOF in different vials (10 mL) and then placed in the oven at 30 °C. After adsorption of MB, the color of the MOFs changed from blue to deep blue. The adsorption of MB on MOFs was also assessed by the presence of characteristic strong vibration bands of MB in the FT-IR spectrum (Fig. 53). After 24 h, the supernatant of the solution was analyzed using a UV-VIS spectrophotometer at 664 nm.

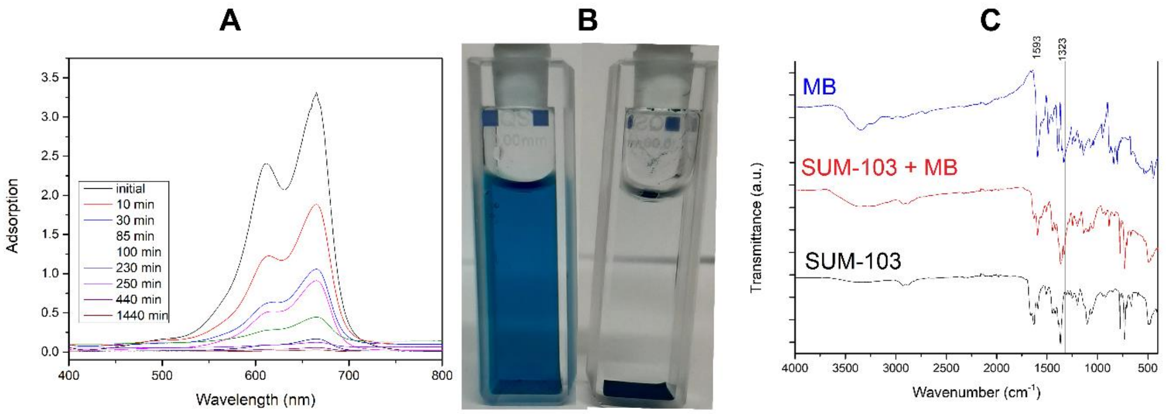

Figure 53. (A) MB adsorption kinetics over SUM-103, (B) 2.5 mL, 15 mg L^{-1} MB solution before & after 24 h at room temperature, (C) FT-IR comparison before and after adsorption.

The isothermal adsorption capacities were modeled according to Langmuir and Freundlich models. It was observed that the quantity of MB adsorbed at the surface of the material is 194 ± 4 mg g^{-1} (Langmuir) for SUM-103. By comparison, SUM-103, therefore, appears as a MOF exhibiting a significant adsorption capacity while exhibiting an average specific surface area (Table 6).

Table 6. Comparison of adsorption capacity of different MOFs

MOF	Q_i maximum adsorption capacity (mg g^{-1})	BET surface area (m^2 g^{-1})
SUM-103	194 ± 4	1058
HKUST-1 [12]	454	1726
NH2-MIL-101 (Al) [11]	762 ± 12	2100
UiO-66 [13]	91	765

The kinetic study of MB adsorption was carried out at room temperature. For kinetic studies, 3 mg SUM-103 was placed in a quartz cell, later 2.5 mL, 15 mg L^{-1} methylene blue solution was added. At regular time intervals, the concentration of MB was measured by UV-vis spectroscopy.

A pseudo-second order kinetic model was used, fitting suitably the experimental data. This validates that the adsorption is mostly chemisorption, rather than physisorption. As expected, at low MB concentration, it was possible to achieve nearly quantitative adsorption rates. Hence, after 48 h at 25 °C, 99.8% adsorption was observed for 2.5 mL of MB solution with a concentration of 8.7 mg L^{-1} over 1.8 mg of MOF, being consistent with the model Langmuir used for describing the adsorption phenomenon. The kinetic fitting graphs, according to the different models, were given in Figures 54 and 55, respectively.

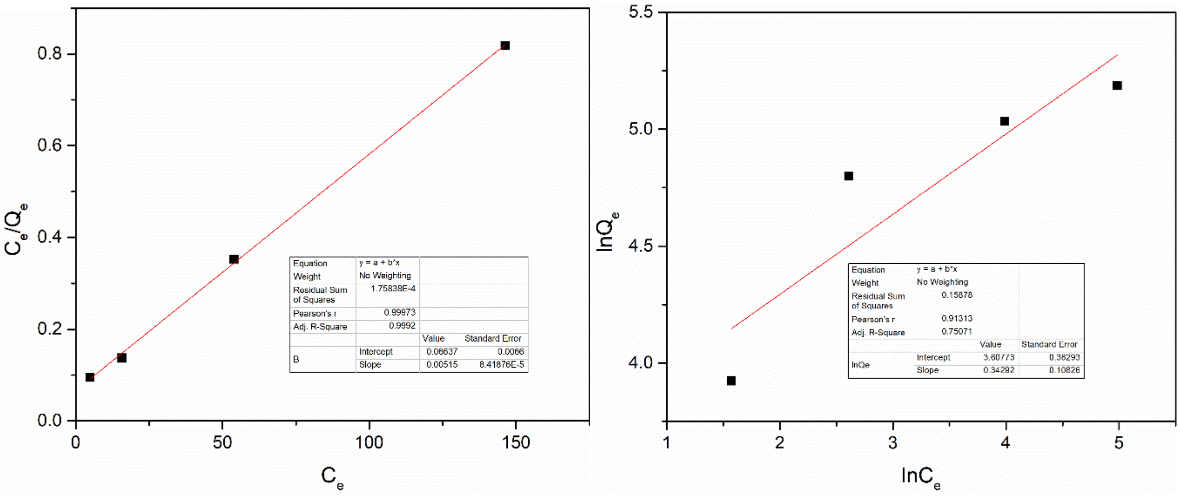

Equation	y = a + b*x		
Weight	No Weighting		
Residual Sum of Squares	1.75838E-4		
Pearson's r	0.99973		
Adj. R-Square	0.9992		
		Value	Standard Error
B	Intercept	0.06637	0.0066
	Slope	0.00515	8.41876E-5

Equation	y = a + b*x		
Weight	No Weighting		
Residual Sum of Squares	0.15878		
Pearson's r	0.91313		
Adj. R-Square	0.75071		
		Value	Standard Error
lnQe	Intercept	3.60773	0.38293
	Slope	0.34292	0.10826

Figure 54. Langmuir (left) and Freundlich (right) fitting parameters for MB adsorption over SUM-103.

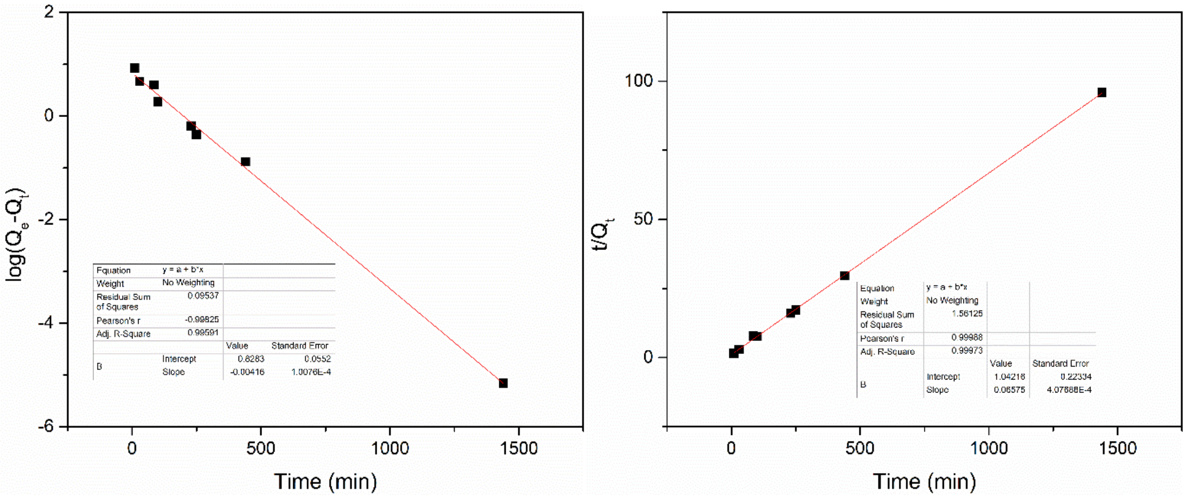

Fquation	y = a + b*x		
Weight	No Weighting		
Residual Sum of Squares	0.09537		
Pearson's r	-0.99825		
Adj. R-Square	0.99591		
		Value	Standard Error
B	Intercept	0.8283	0.0552
	Slope	-0.00416	1.0076E-4

Equation	y = a + b*x		
Weight	No Weighting		
Residual Sum of Squares	1.56125		
Pearson's r	0.99988		
Adj. R-Square	0.99973		
		Value	Standard Error
B	Intercept	1.04218	0.22334
	Slope	0.06575	4.07888E-4

Figure 55. Pseudo first order (left) and pseudo-second order (right) fittings for MB adsorption on SUM-103.

In conclusion, new series of MOFs, named SUM (standing for Strasbourg University Materials) have been prepared using original ligands. Designed for supramolecular interactions, ligand side-chains are composed of ethylene glycol moieties. These MOFs exhibit useful properties without damageable reduction of their adsorption capacity. A single crystal study showed that the "primary structure" of NOTT MOFs is preserved. X-Ray diffraction patterns and TGA analysis showed their high stability in air and water.

The amphiphilic character of the pores introduced by ethylene glycol chains gave birth to specific stability to these solids in water and thus to a strong potential of use for extracting organic pollutants from water.

As a consequence SUM-103 could be used in water to extract organic molecules such as methylene blue (cationic) or alizarin yellow R (anionic). In addition, the comparative study of SUM-102 and SUM-103 showed higher values with the latter (94 *vs.* 83%), under the same conditions, thus highlighting the importance of supramolecular interactions created by the side chains. Compared to other MOFs, and taking into account their surface area, the MB uptake demonstrates that functionalization by fragments capable of supramolecular interactions with a substrate could be an interesting way for MOF adsorption properties modulation.

III. HCOH adsorption of SUM-102 (Cu@H4L2) and SUM-103 (Cu@H4L3)

The possibility of pore engineering in MOFs makes them attractive not only for dye adsorption in the aqueous phase but also for the capture of gases. MOFs are mainly used for gas adsorption. Among gases, most commonly tested as adsorbates are CO_2, N_2, H_2, C_2H_2, etc. Besides, less popular toxic warfare gases have also been tested [14], such as NH_3 or VOCs (Volatile Organic Compounds) [14,15]. Herein, our as-synthesized MOFs, namely SUM-102 and SUM-103, were evaluated in the adsorption of gaseous formaldehyde, which is a harmful VOC, under realistic conditions of indoor air concentration.

Indeed, Formaldehyde is one of the most toxic and even carcinogenic contaminants found in indoor air [16,17]. Even though it may be detected in outside air exhaled or created by traffic [18-21] or photochemical processes [18,20,22], it is more commonly found in indoor air due to the existence of several sources. A difference can be drawn between continuous and point sources [23,24]. Construction materials (chipboard, OSB, laminate flooring, etc.) [25,26], decorative materials (paint, dyes, etc.) [25,27,28], and furniture [20,24,25,27,28], particularly those constructed from particleboard attached with urea-formaldehyde glue [29-32], are all continuous sources.

All combustions (unvented paraffin stoves, candles, incense sticks, etc.) [20,21,28,33] are considered point sources, like in the use of disinfectants and other cleaning chemicals [19,34]. In addition, the combination of ozone from outside air with terpenes generated by wood-based products [22,35-38] can produce formaldehyde in situ. As a result, formaldehyde may be found in practically all indoor situations, with concentrations ranging from 10 to 100 g m^{-3} in household settings to several hundred g m^{-3} in workplace settings [16,18,20,22]. As already stated, formaldehyde has been classified as a carcinogen (category 1) by the International Agency for Research on Cancer (IARC) since 2006. Because of these negative consequences, French law on this pollutant in indoor air in public buildings has been tightened. Agreeing to Proclaim No. 2011-1727 of December 2011, a constrain esteem of 30 g.m^{-3} has been set for long-term exposure to formaldehyde since 2015.

Table 7. Parameters of MOFs and their adsorption capacity

Adsorbent	**SSA values [m^{2} g^{-1}]**	**Pore volume [cm^{3} g^{-1}]**	**Mass [mg]**	**Adsorption capacity [µg g^{-1}]**	**Break through time [min]**	**Saturation time [min]**	**HCHO surfaces adsorption capacity [µg m^{-2}]**	**HCHO volumetric adsorption capacity [g m^{-3}]**
HKUST-1	1733	0.89	3.0	504 ± 87	70	1040	0.29	566
Cu@H4L1 **UTSA-90**	1239	0.63	5.2	513 ± 58	490	1152	0.41	814
Cu@H4L2 **SUM-102**	870	0.45	5.6	453 ± 50	10	1110	0.52	1007
Cu@H4L3 **SUM-103**	1058	0.57	6.5	302 ± 33	60	834	0.29	530

This esteem will be brought down to a threshold of 10 mg. m^{-3} in early 2023. [39].

One of the benchmark MOFs used in formaldehyde adsorption remains HKUST-1. In our recent paper [40], we compared SUM-102 and SUM-103 with some cation-exchanged zeolites and HKUST-1. During the experiment, the concentration of formaldehyde was set to 164 ppb in flow gas (synthetic air). The details are given in the experimental part. Table 7 summarizes the textural properties of the MOFs and their adsorption capacity and detailed data obtained.

As it can be seen from Table 7, HKUST-1 exhibits the highest specific surface area among the tested MOFs. Also, it led to achieve the highest formaldehyde adsorption capacity. However, if we look at the adsorption per surface area unit and volume unit, SUM-102 demonstrated higher adsorption capacities. While comparing surfacic adsorption capacity, SUM-102 is nearly twice better than benchmark HKUST-1.

In contrast to the adsorption of dyes (Section 1), the longer side chains decreased the adsorption of formaldehyde. It could be explained as a sum of several interactions. Firstly, both the oxygen atoms in the side chains and formaldehyde are hydrogen bond acceptors, therefore repulsion between them is expected. On the other side, these chains could create an optimally sized cavity for formaldehyde molecules. Thus, the combination of both effects, yielded a higher surfacic and volumetric adsorption capacity for SUM-102.

IV. CO_2 adsorption

1) SUM-100 series

It is not a secret that CO_2 is the most emitted greenhouse gas and ever growing one. In the introduction chapter, the different CO_2 capture methods were discussed, focusing also on the nature of potential MOFs for capturing CO_2. Likewise, the importance of ethylene glycol for adsorbing CO_2 was also considered. Therefore, we have tested our MOFs in CO_2 adsorption. The first NOTT-101, UTSA-90, SUM-102, and SUM-103 were analyzed in the CO_2 adsorption at 273 K from atmospheric pressure up to 10 bar by Micromeritics ASAP 2050. Before the analysis, the samples were activated at 160°C for 8 hours. The results are given in Figure 56. It is noteworthy that except for

NOTT-101, all MOFs exhibited nearly the same adsorption capacity, around 10-13 mmol/g under given conditions. While calculating the adsorption of CO_2 per surface area, UTSA-90 exhibited the lowest and SUM-102 reached the highest value. However, the high adsorption (19 mmol/g) of NOTT-101 attracted our attention since the value was much higher compared to other MOFs of the series: 19 vs 10-12 mmol/g. The only difference relies on a slightly different synthesis method of NOTT-101, yielding smaller crystal sizes. To check this hypothesis, other MOFs were prepared according to the same procedure. It should be noted that the MOFs were previously prepared as microcrystalline (visible under an optical microscope) powder, except NOTT-101.

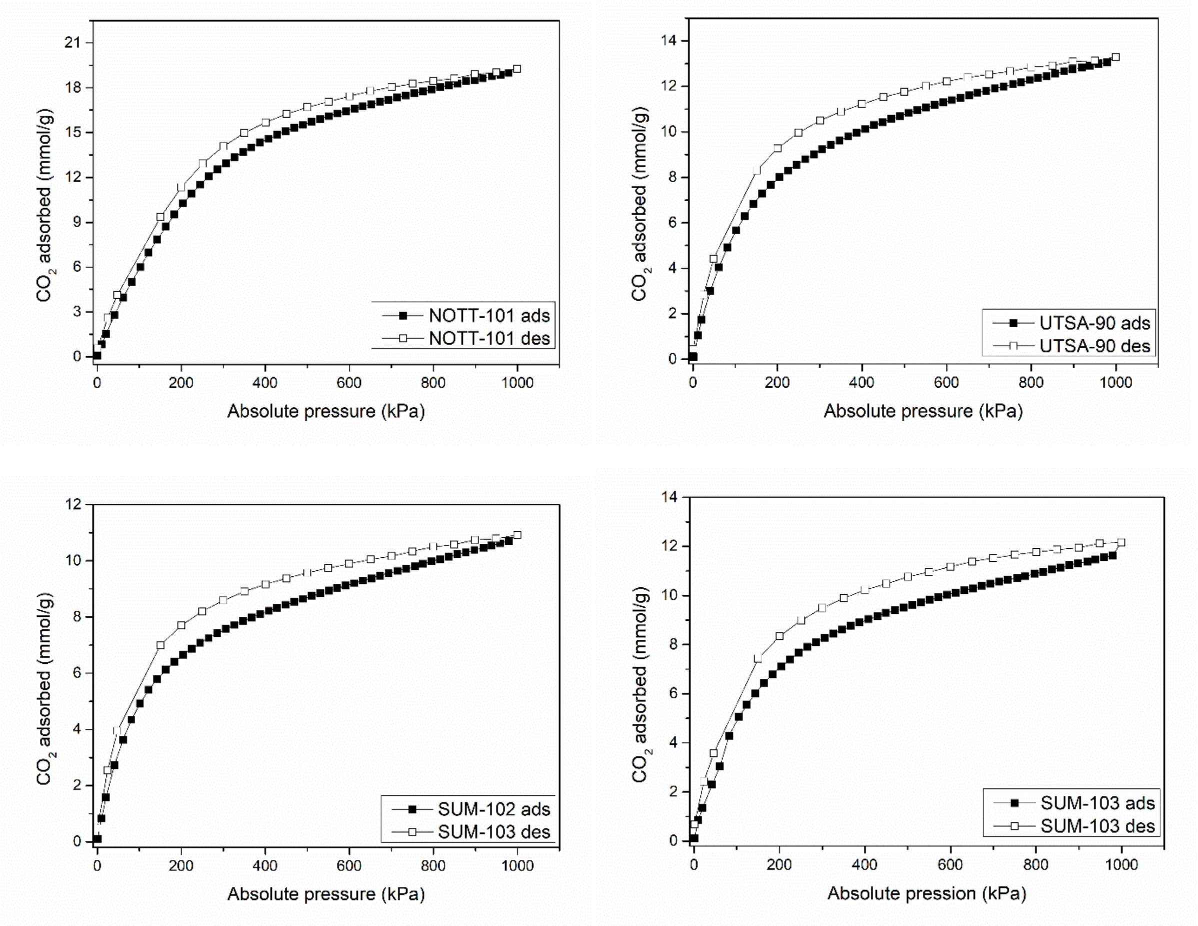

Figure 56. CO_2 adsorption/desorption of MOFs at 273K.

Thus, we added “m” to the ending of the names of the MOFs to differentiate them from previously synthesized crystals. An example of the difference in average sizes is given in Figure 57.

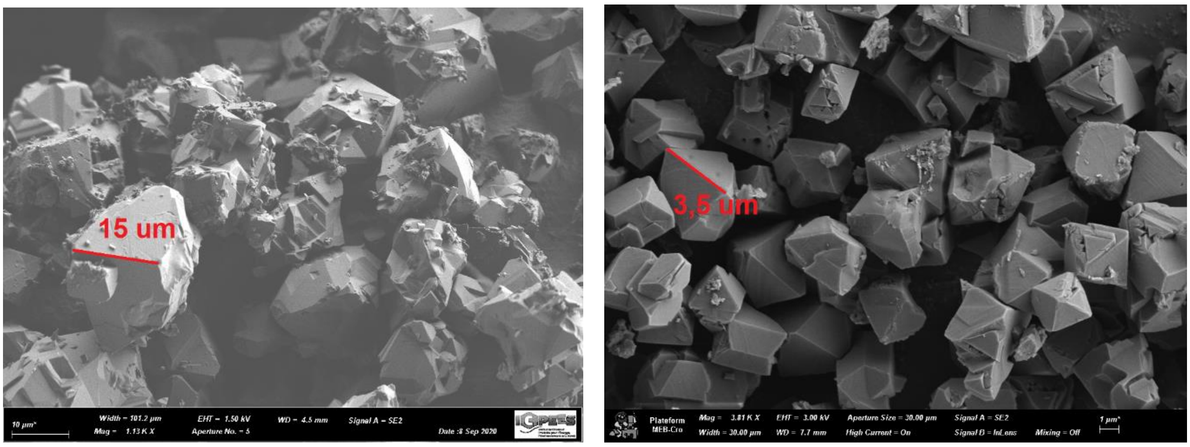

Figure 57. SEM images of SUM-103 (left) and SUM-103m (right).

Hence, the new smaller crystal-sized samples were evaluated in the CO_2 adsorption. It is important to highlight here that no significant change was made in the procedure of MOFs synthesis, solely the ratio between the water and the acid was adapted as follows: instead of 0.65 mL of water and 33 μL HCl, 2-3 drops of HCl (3.7 % solution) were added and the temperature was slightly raised from 80 to 85°C. The new results obtained are presented in Figure 58.

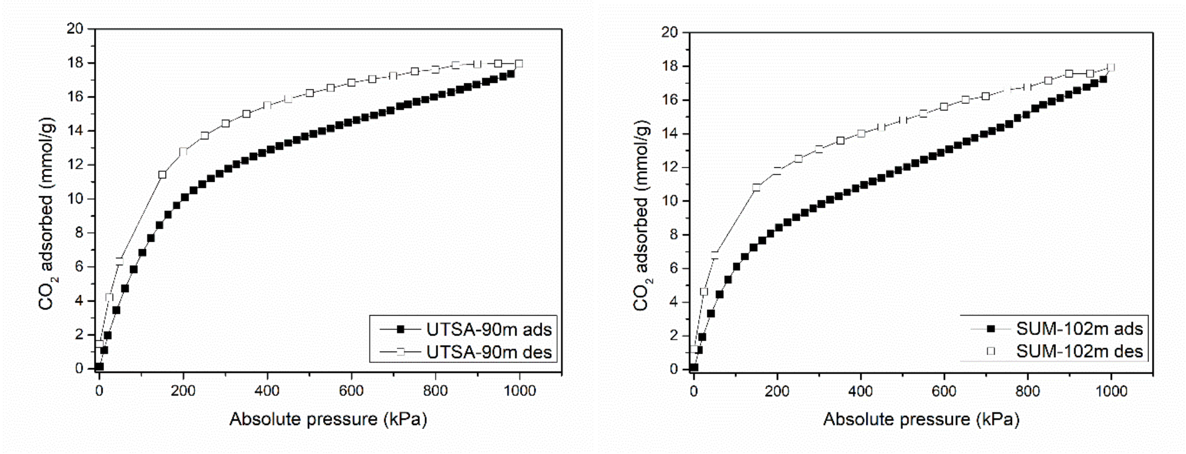

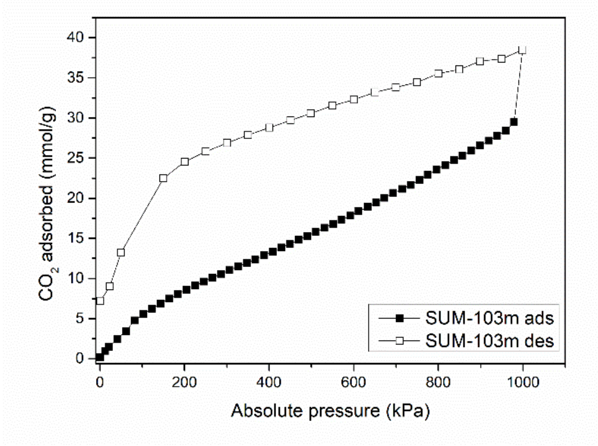

Figure 58. CO$_2$ adsorption of MOFs (small crystal sized).

From the results, a significant increase in the adsorption capacity could be observed for all MOFs. In the case of UTSA-90 and UTSA-90m the adsorption increased from 13 mmol g^{-1} to 17.36 mmol g^{-1} (34%). Within the SUM series, the adsorption capacity increased with geometric progression. The values of CO$_2$ adsorption for SUM-102 and SUM-102m were 10.7 mmol g^{-1} and 17.23 mmol g^{-1}, respectively (61% increase). Finally, the biggest surprise was observed for SUM-103m. Compared to pristine SUM-103 (11.6 mmol g^{-1}), the adsorption **was dramatically enhanced to 38.5 mmol g^{-1}, a 232 % increase**. To the best of our knowledge, SUM-103m is the best CO$_2$ adsorbing material in the world. But as in the song "can't take my eyes off you" the results are "too good to be true".

Also, a larger hysteresis between adsorption and desorption branches could be observed while increasing side chains (Figure 58). For instance in SUM-103m, nearly 7 mmol g^{-1} CO$_2$ was left inside (or outside?) the MOF pores, in a near-vacuum. Hence, several issues and questions need to be answered:

1) Does the size of the crystal play a significant role?

2) Are those results reproducible?

3) Will a larger side chain further increase the adsorption capacity?

To answer the first question, we played with the synthesis conditions to grow even smaller-sized crystals. We succeeded to make around 100 nm-sized crystals, which were nearly 35 times smaller than SUM-103m. It is important to remind here that SUM-103m was smaller than SUM-103 by nearly 5 times. To synthesize small-sized crystals, the easiest way is to increase the nucleation rate. Therefore, we eliminated the acid from the reaction mixture, and instead, we added a diluted KOH solution. The CO_2 adsorption profile for this MOF, which we called SUM-103 v.2.4 is given in Figure 59.

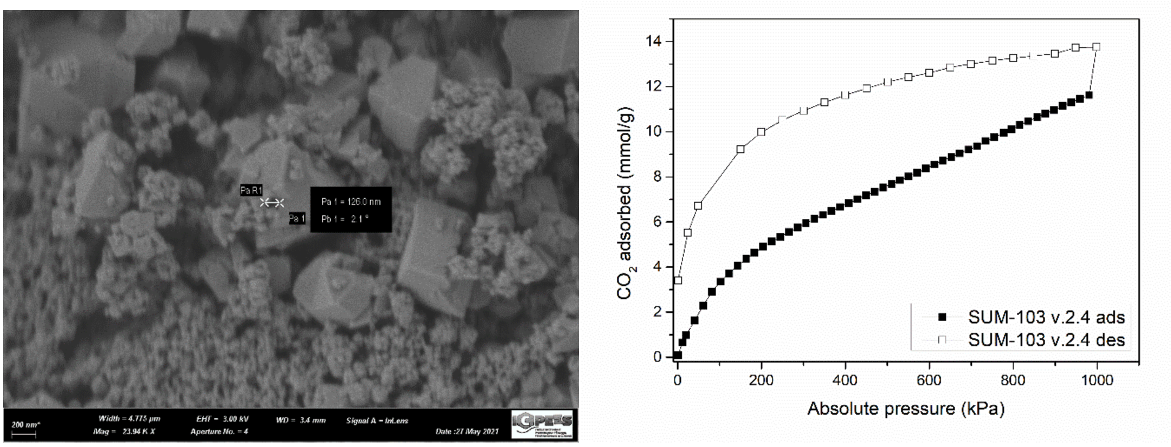

Figure 59. SEM image (left) and CO_2 adsorption isotherm (right) of SUM-103 v.2.4.

As it can be seen from the isotherm, CO_2 adsorption capacity decreased compared to SUM-103m, from 38.5 mmol g^{-1} to 13.8 mmol g^{-1}, but remained still higher than SUM-103 (11.6 mmol g^{-1}). However, like in SUM-103m, some CO_2 was left in the MOF (3.4 mmol g^{-1}).

The specific surface areas of modified MOFs were measured before CO_2 adsorption. All the aforementioned values are presented in Table 8.

Table 8. Comparison of different parameters of MOFs (ASAP 2050 device).

MOF	Average crystal size (µm)	Surface area (m^2/g)	CO_2 adsorption (mmol g^{-1}) at 10 bar and 273K
UTSA-90	10-15	1240	13
UTSA-90m	5-10	1333	17.4
SUM-102	10-15	870	10.7
SUM-102m	10-15*	900	17.2
SUM-103	10-15	1058	11.6
SUM-103m	3-5	850	38.5
SUM-103 v.2.4	0.05-2	703	13.7

The first question can now be answered (at least partially). The key parameter to reaching high adsorption is not linked to crystal size. However, before trying to switch to the second question, we pay attention to the “crystal size” column for SUM-102m in Table 8. The reason for the asterisk “*” next to the value is that a rather weird round “coronavirus”-like morphology was observed for these 10-15 μm sized crystals (Figure 60, right). These formations were homogenous and around 200 nm-sized. We did not further investigate the nature and formation of these round coronavirus-like morphologies. Also, it is worth mentioning that in the synthesis of the SUM-102m only DMF, water, hydrochloric acid, copper nitrate, and ligand were used. It is worthy to mention that neither surfactant nor modulator was used, in the protocol which yielded those unusual structures.

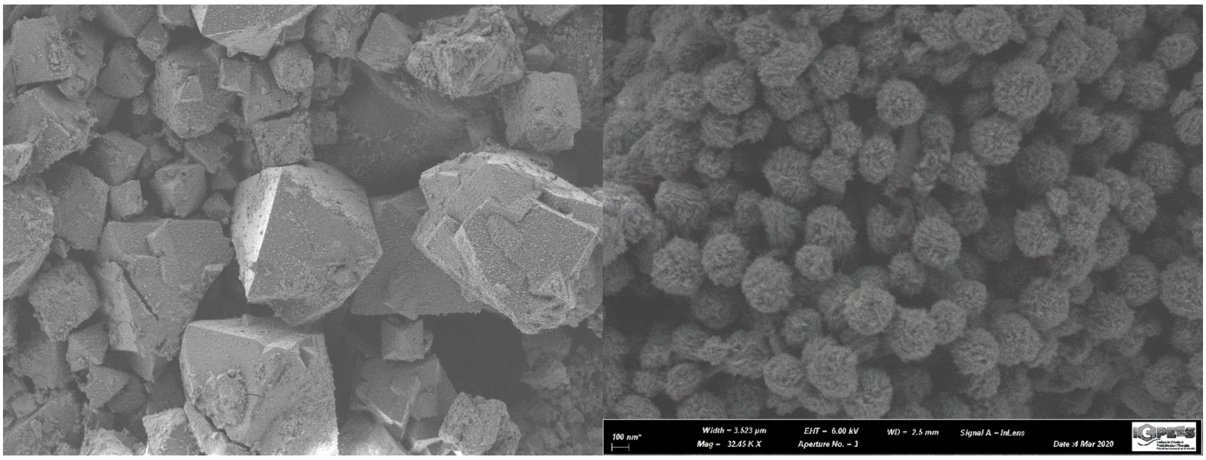

Figure 60. Crystals of SUM-102m (left) and "coronavirus" like structures (right).

At present, the second point related to the reproducibility of these results can be discussed. The first thing to consider is that the adsorption was unbelievably higher. Our colleagues from the ICPF in Prague (Center for textural analysis) repeated 3 times the measurement on the same sample. The results were 35 mmol g^{-1}, 35 mmol $g^{-1,}$ and 38.5 mmol g^{-1}, respectively. Besides, the same adsorption capacity was achieved over a new batch of SUM-103 material.

Therefore, it was decided to perform CO_2 adsorption experiments based on the gravimetric method in South Africa, in the laboratory of Len Barbour at Stellenbosch University. The device for measuring CO_2 adsorption was based on gravimetric data. Simply saying, MOF hanged from a thin wire linked to an extremely sensible balance. The adsorption is calculated based on mass changes (CO_2 uptake). The experiments could be performed from atmospheric up to 20 bar and at 273K.

SUM-103, SUM-103m and SUM-103 v.2.4 were evaluated up to 20 bar (Figure 61). It appeared that nearly the same adsorption was reached for all MOFs, being around 9 mmol g^{-1}. A significant discrepancy is observed with the volumetric measurements performed at ICPF in Prague (by Dr. Karel Soukup). It worth to underline that despite excat same caracteristics and synthesis methods, the batch of the MOFs were different. The second remarkable difference relies on the shape of the curves, which corresponds to a type I isotherm, characteristic of purely microporous materials.

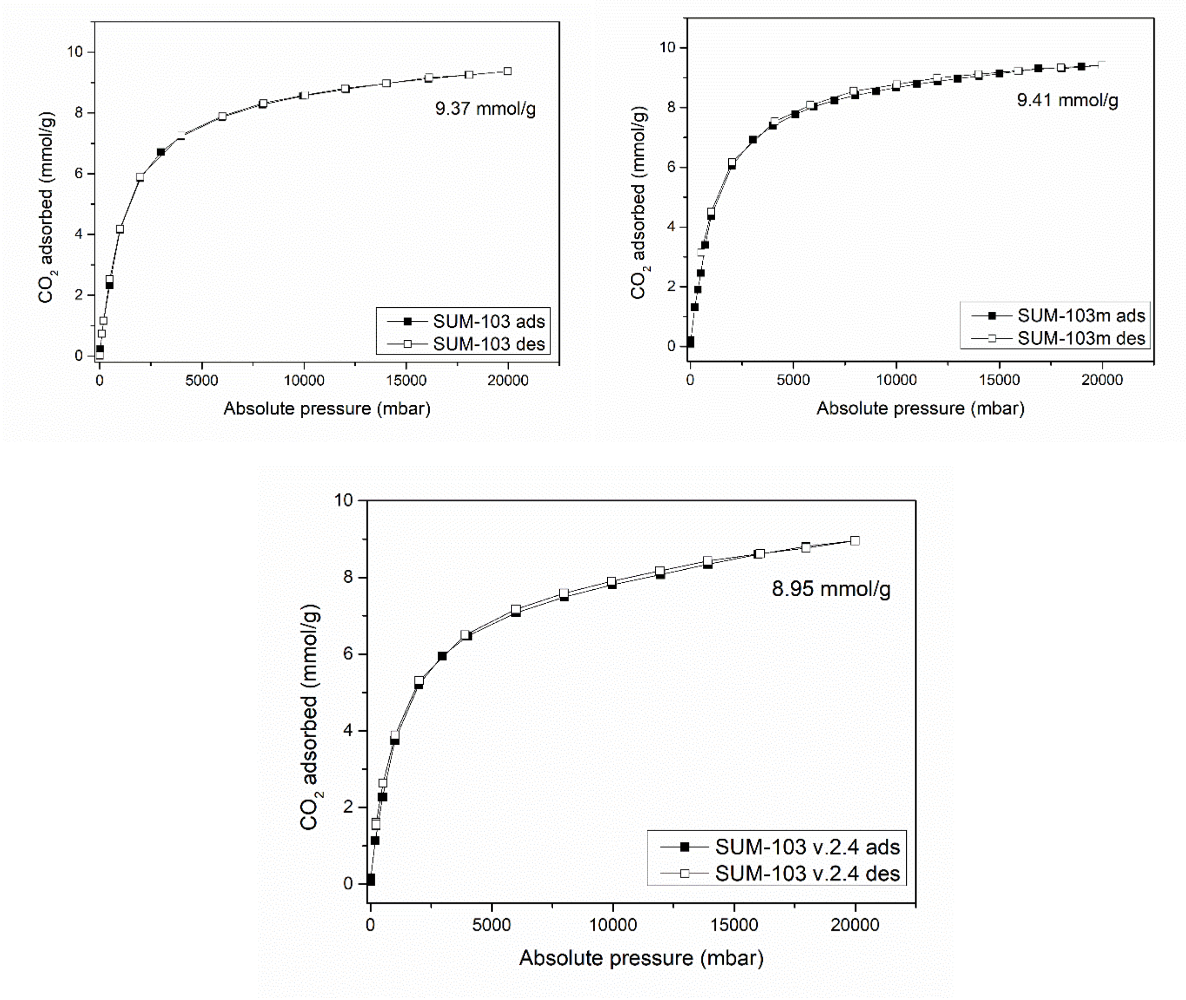

Figure 61. CO_2 adsorption isotherms of MOFs made with the gravimetric method.

Those values obtained were also reproducible, with an absence of a hysteresis loop in stark contrast to the isotherms obtained by the volumetric method (Figures 58-59).

To partially conclude on this second point, both the results acquired with the volumetric method in the Czech Republic and the ones obtained by the gravimetric method in South Africa are reproducible. However, a serious discrepancy both in the shape of the isotherms and the CO_2 adsorption capacity is observed. Hence, a new question arises here: are those differences related to the use of different techniques?

To find an answer to this question, the third series of experiments were performed at the MADIREL in Marseille (by Dr. Sandrine Bourrelly). The adsorption was measured at 303K up to 40 bar. The "homemade" device was volumetric coupled with a microcalorimeter which allows measuring the heat of adsorption, which gives information about the strength of interaction between host and guest.
The CO_2 adsorption profile at 303 K showed maximal adsorption of 20.9 mmol/g (Figure 62). As the device in the MADIREL laboratory was homemade, the following figures were named after the city of the corresponding Universities (Prague, Marseilles, Stellenbosch). From the adsorption capacity, the values obtained with Hiden Isochema IGA-001 (Stellenbosch, gravimetric) and Microcalorimetry coupled device (Marseille, volumetric) are close to each other, respectively around 9.5 and 12 mmol g^{-1} (at 20 bar).

However, we should take into consideration that there is a 30K(°C) temperature difference. Also, the later profile of the adsorption branch is rather like the one obtained with ASAP 2050 measurement (Prague, volumetric), even being more exponential without saturation. These 30K differences between adsorption temperatures may be sufficient to explain a decrease in the adsorption capacity. Indeed, different values are reported in the literature, varying from 10-15% up to several times [41,42]. But taking into account the "weird" adsorption pattern of the SUM-103m, it was difficult to predict this behavior.

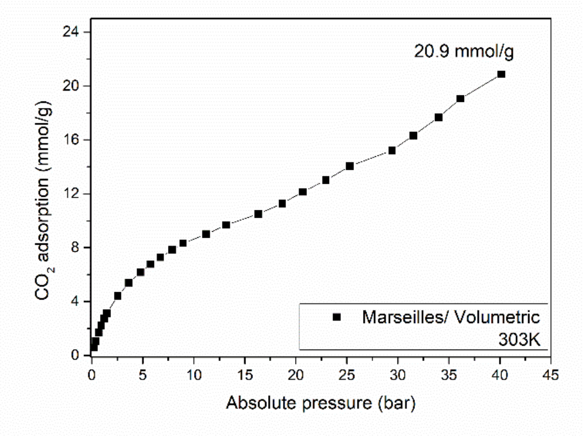

Figure 62. CO_2 adsorption isotherm done in Marseille (left)

Furthermore, as we measured the adsorption of CO_2 with microcalorimetry, we obtained results on the heat of adsorption. In the beginning, the value is around 30 kJ mol^{-1}, which is slightly higher than "classic" MOFs. This shows specific adsorption sites with high energy. However beginning from nearly 10 bar, this value drops to 17 kJ mol^{-1}, which is close to the liquefication enthalpy of CO_2, meaning adsorption happens mostly based on the interaction between CO_2 molecules. This kind of CO_2-CO_2 interaction was also observed by Hou *and al.* [44] Moreover, according to C. R. C. Jensen and N. A. Seaton [45] continuous adsorption in microporous materials could happen because of the compressibility of adsorbates. By taking into account the previous tests, it is difficult to undoubtedly explain the discrepancies between the methods and equipment. Different devices and different temperatures made rather difficult the comparison. One thing is important to highlight, something “mystical” occurred with these MOFs and the mystery raises while increasing the side chain length.

Now, we need to discuss the 3rd question, whether the adsorption is linked (or not) to the size of the side chains. For this purpose, the H4L4 ligand was synthesized and its corresponding MOF was named SUM-104. This copper MOF was prepared in the same conditions as SUM-103m (the best adsorbent).

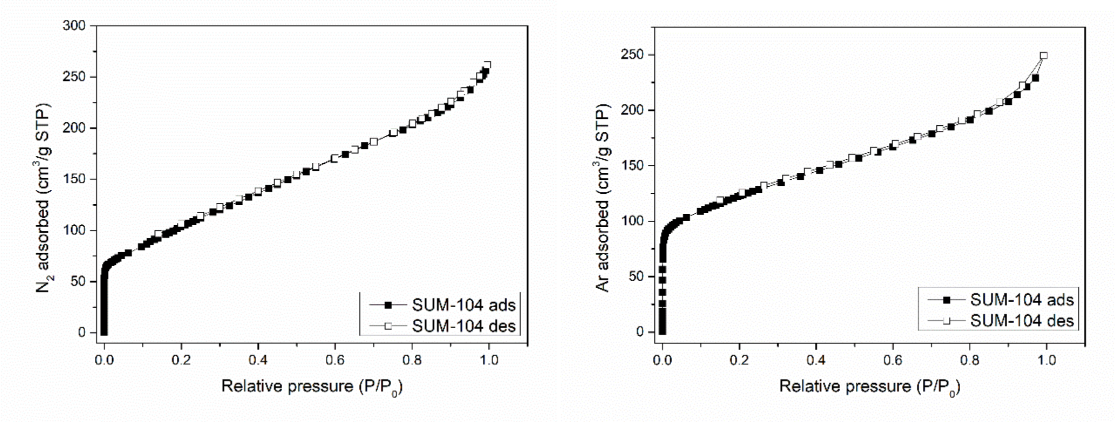

Figure 63. Nitrogen (left) and Argon (right) adsorption isotherms for SUM-104.

Nitrogen and argon adsorption-desorption isotherms are shown in Figure 63. All the MOFs beginning from this part are analyzed via ASAP 2050 (Dr. Karel Soukup) at 273K and up to 10 bar, except SUM-200 series MOFs. As seen, another surprise has been witnessed: the profile of adsorption is not matching with classical type I isotherm for microporous materials. Despite Ar and N_2 can be considered inert gases (Nitrogen is less inert, with some quadrupole moment), SUM-104 has an affinity towards them and especially at lower pressures up to 1 bar. The shape of the adsorption is closer to (large) mesoporous materials, but from PXRD studies, the MOF material has been shown to be purely microporous.

We observe this weird tendency also with pore sizes, calculated based on the adsorption. In the case of Ar, where adsorption in the "mesoporous zone" is less, most of the pores have a 5.8 Å width, with some "anomalies" between 2.4-4.6 nm (Figure 64).
In the case of Nitrogen, the width of micropores is 10 Å. However, some "anomalies" observed for Argon, in the case of Nitrogen became significant, according to results little less than half of the pores have between 2.5-5 nm width. Sometimes 2-4 nm size could indeed be due to intercrystalline voids between the particles/crystals. But in the case of Nitrogen, the ratio of larger pores is high.

The specific surface areas for SUM-104 are found 371 m^2 g^{-1} and 385 m^2 g^{-1}, respectively for N_2 and Ar physisorption measurements.

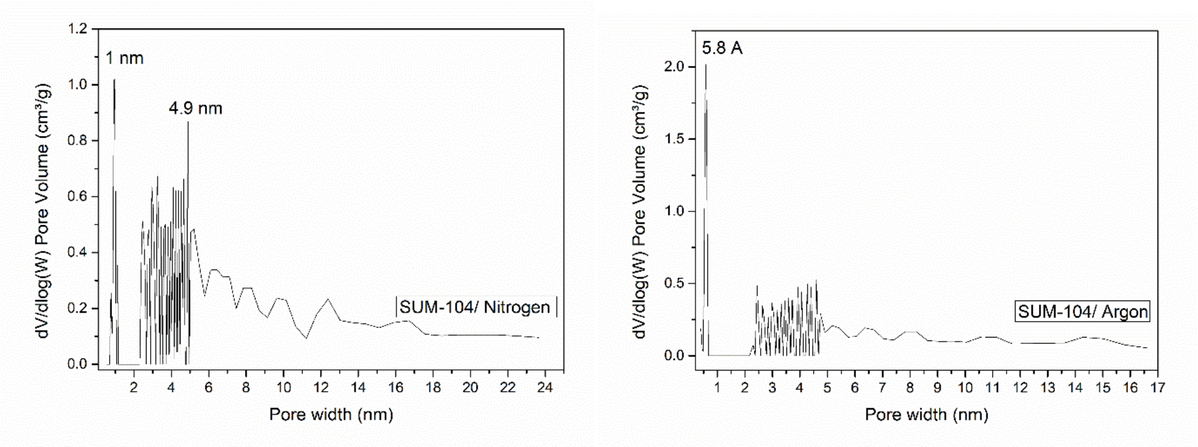

Figure 64. Pore width distribution: Left-based on Nitrogen, Right-based on Argon adsorptions for SUM-104.

For the CO_2 adsorption, SUM-104 showed the same trend as SUM-103m, but the adsorption was less than SUM-103m (Figure 65). The maximal adsorption at 10 bar is 19.3 mmol g^{-1}. However, like in SUM-103m, there is a large hysteresis and after desorption 4.64 mmol g^{-1} CO_2 is left inside (or outside) the material. Thus, now we can answer our last question. The adsorption of CO_2 does not increase with increasing the length of the side chain. Interesting thing is that the percentage of the leftover CO_2 after the desorption is close. In the case of SUM-103m, it's 18.7%, and for SUM-104 it is 24%. However, we will see in the case of Ca@H4L3 (SUM-303) (figure 68) that the increase of the equilibration time eliminates the remaining CO_2.

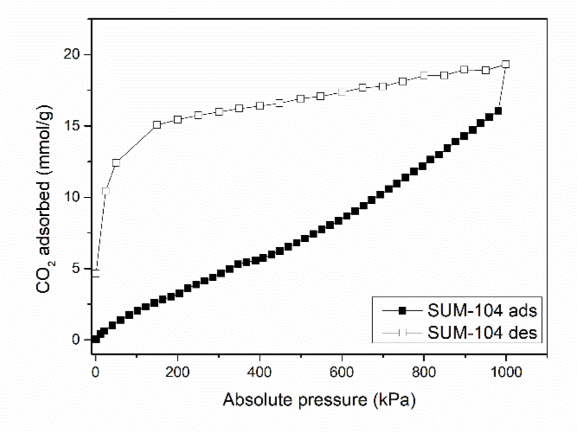

Figure 65. CO$_2$ adsorption isotherm of SUM-104.

2) SUM-200 series

Again, the CO$_2$ adsorption capacity of the SUM-200 series seems rather "weird". It is important to remind here that SUM-200 series MOFs did not exhibit a high specific surface area (chapter II). Then there the following question arises: can MOF without significant surface area adsorb a gas? The answer is yes. We do not know exactly how the SUM-200 series adsorbs CO$_2$, but the values remained small as shown in Figure 66. It is possible that Nitrogen and Argon molecules, which have kinetic diameters of 360 pm and 340 pm respectively, cannot enter the pores of the MOF. Compare to previous gases, CO$_2$ has a slightly smaller diameter-330 pm, and also it is much more polar than them.. We tested the MOF in our laboratory at up to 1 atm pressure at 273 K (ASAP-2020 device).

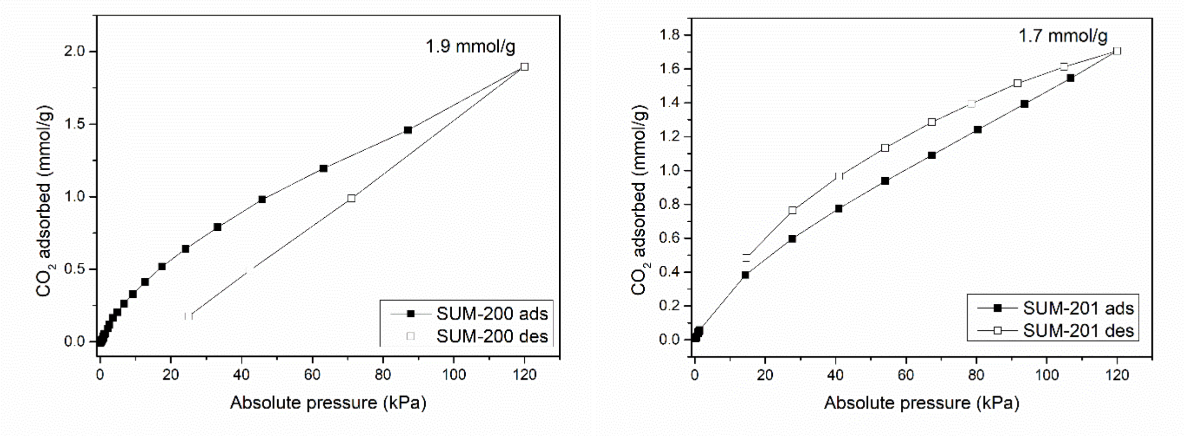

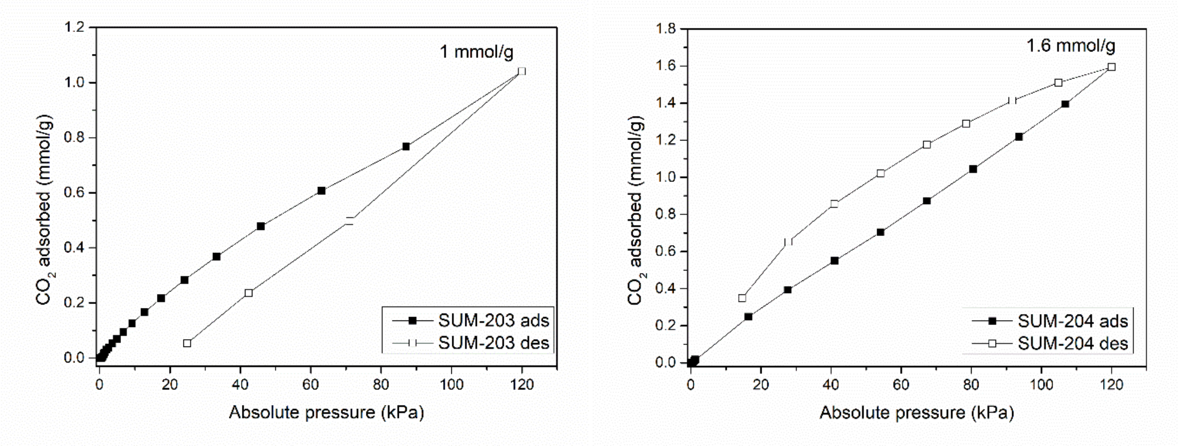

Figure 66. CO$_2$ adsorptions of SUM-200 series.

The adsorption data for SUM-202 is missing because the same synthesis procedure on a larger scale (20-30 mg) is not working. Though specific surface area remains low, it can be observed that an increasing side chain length diminishes the porosity. Hence, the adsorption decreases with increasing chain length. However, this trend was reverted for SUM-204. After all, it is discussable whether 1 or 2 mmol g^{-1} are significantly higher values and/or less than 1 mmol g^{-1} difference is enough to judge the adsorption.

For, SUM-203 the CO$_2$ adsorption was also measured in Stellenbosch with the gravimetric method up to 20 bar and at 295K. The results are comparable with the volumetric method that we did in our laboratory, taking into account difference in temperature (Figure 67).

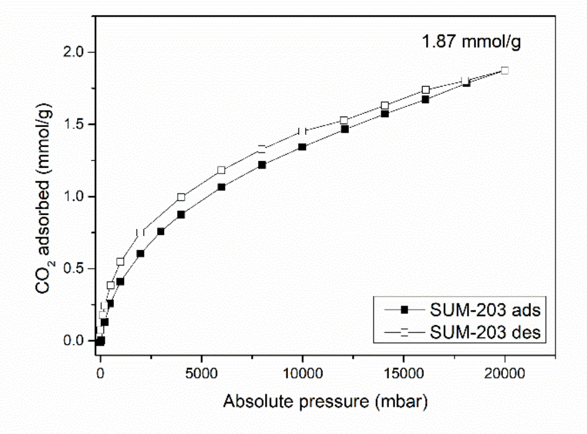

Figure 67. CO$_2$ adsorption isotherm of SUM-203 at 295K.

3) High adsorption of other H4L3 based MOFs.

The good results achieved with SUM-103m encouraged us to test other MOFs with the H4L3 ligand for CO_2 adsorption. For this purpose Ca, Mg, Zn and Li* MOFs were sent for analysis. The measures were performed at 273K.

As discussed in chapter II, SUM-303 (Ca@H4L3) did not present any surface area. However, SUM-303 was tested in the CO_2 adsorption. The result of the adsorption of SUM-303 is presented in Figure 68. Also, this time to find a sudden increase in the adsorption branch which is observed in the last point, the adsorption equilibration time was increased from 30 to 90 seconds.

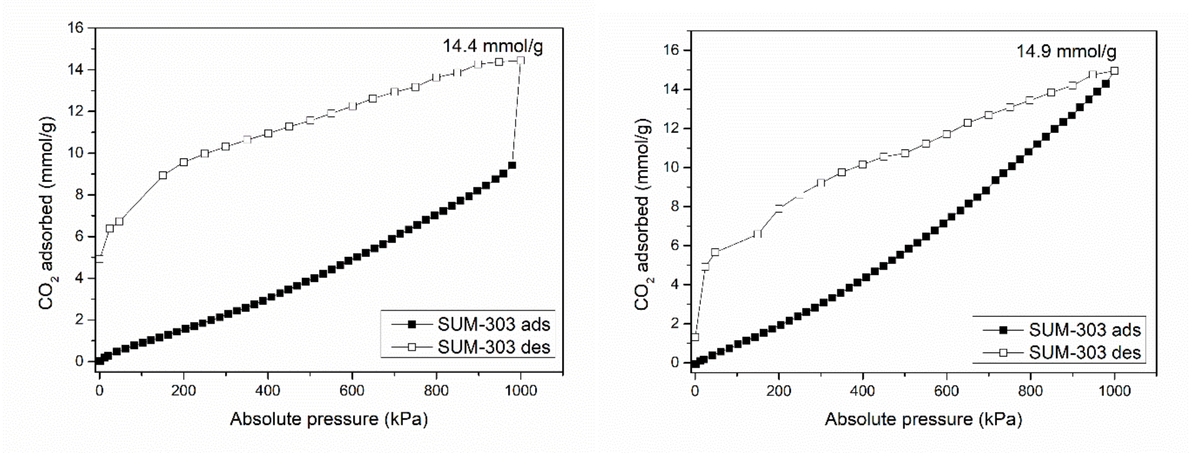

Figure 68. CO_2 adsorption of SUM-303 with the 30s (left) and 90s (right) equilibration time.

It is worth mentioning that we also measured the surface area and CO_2 adsorption (up to 122 kPa) in our lab. Likewise, no significant surface area could be measured for SUM-303 by N_2 adsorption.

When paying attention to the two isotherms in Figure 68, we observe that a sudden increase disappeared while increasing the equilibration time. Moreover, in the first case (30s equilibration time) 4.9 mmol g^{-1} gas was left in the material, versus 1.3 mmol g^{-1} with 90s equilibration time. Also, the adsorption is slightly increased from 14.4 mmol g^{-1} to 14.9 mmol g^{-1}. Therefore, despite not showing surface area, SUM-303 adsorbs a significant amount of CO_2.

This high CO_2 adsorption shows again the importance of the functionalization with glyme group bearing chains. These adsorption tests and the other ones beginning from this part were done by the ASAP-2050 device at 273K.

The next MOF is the SUM-403 (Mg@H4L3). Previously, the importance of Mg MOFs was discussed for CO_2 adsorption in the case of Mg-MOF-74. Also, in chapter II, the unique structure of SUM-403 with the coordination of DMF molecules was presented.

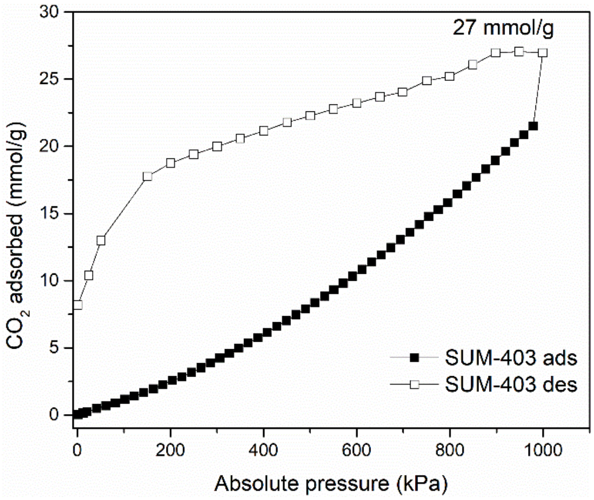

Figure 69. CO_2 adsorption isotherm of SUM-403.

A stunning value of 27 mmol g^{-1} adsorbed was reached over SUM-403 (Figure 69). It could be related to the synergetic effect of the side chains and Mg open metal sites. Most probably, DMF molecules have left the structure, by creating open metal sites behind them [43]. It worth to mention that nearly in all CO_2 adsorption studies the MOFs with ligands H4L3 showed sudden increase at last point (10 bar). As previous example showed, most probably in all samples it is linked to the equilibration time.

Later, we synthesized Zn MOF of the H4L3 ligand (SUM-153). This MOF exhibited the same topology that SUM-103, according to the PXRD pattern shown in Figure 70 left. The adsorption isotherm shows a quite high 17.6 mmol g^{-1} CO_2 adsorption at 10 bar and 273K (Figure 70 right). However, as shown in other H4L3 MOFs, the hysteresis remains present and some CO_2 molecules were left inside MOF (6.1 mmol g^{-1}). Interestingly, the equilibration time was 90 seconds. Thus, it could indicate high energy interactions between CO_2 and SUM-153 or it is difficult for CO_2 molecules to enter and leave the pores because of their long side-chains. Or again, we need to increase the equilibration time.

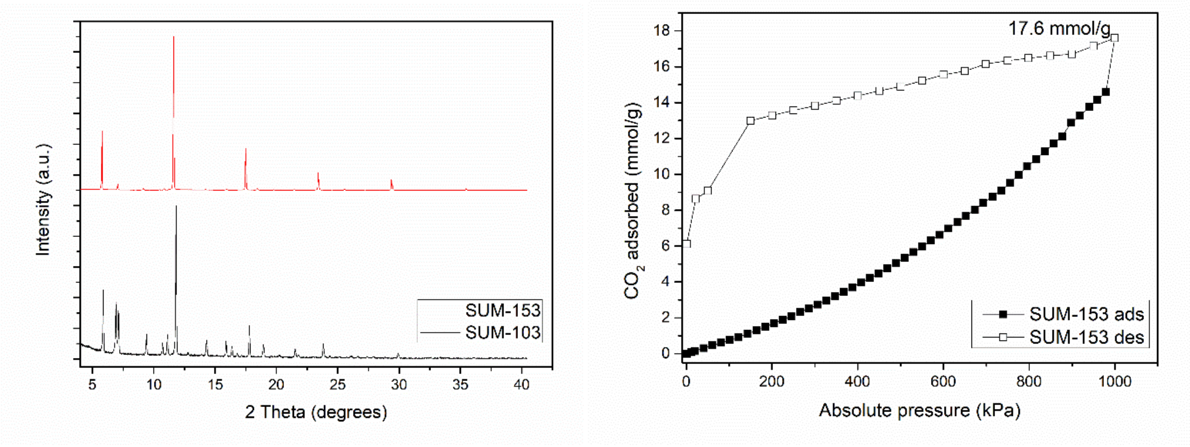

Figure 70. PXRD comparison (left) and CO_2 adsorption isotherm (right) of SUM-153.

The last MOF of the H4L3 series for CO_2 adsorption application was Li@H4L3. As-synthesized crystals did not diffract well for SCXRD analysis. Despite having thin, long crystals intensity of diffraction was very small even for PXRD. As the MOF was prepared at a high temperature in DMF and methanol, there was no probability that it is the crystals of the ligands. Because even at room temperature ligand is soluble in DMF. Thus, we sent a sample for CO_2 adsorption (Figure 71).

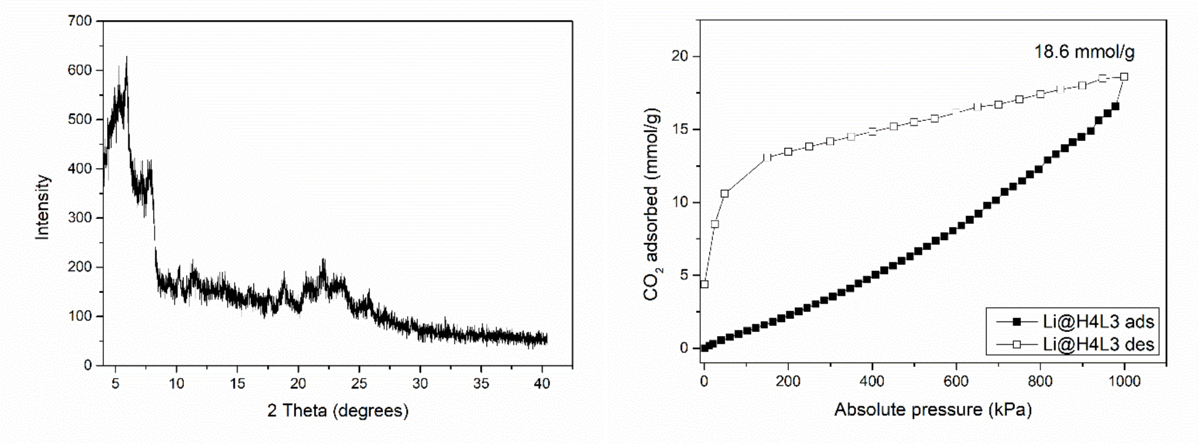

Figure 71. PXRD (left) and CO_2 adsorption isotherm (right) of Li@H4L3.

Surprisingly (or not), Li@H4L3 showed adsorption trends like most other H4L3 MOFs, high adsorption with hysteresis loop, and some CO_2 left inside (4.4 mmol g^{-1}). This time the equilibration time was also 90 seconds.

4) LBM-10 (Cu@H4LOMe) and SUM-401 (Mg@H4L1)

Previously, we mentioned that LBM-10 (Cu@H4LOMe) had a 3D porous network. However, its surface area was smaller in comparison with its “isomer” UTSA-90. As could be seen for SUM-100 series MOFs, the change in the synthesis process influenced a lot of the CO_2 adsorption capacity. For this reason, LBM-10 was prepared similar to SUM-103m.

The adsorption was 9.6 mmol g^{-1}. Despite being a good value, compared to its isomer UTSA-90m (17.4 mmol g^{-1}) and even UTSA-90 (13 mmol g^{-1}) the adsorption remained lower. Nonetheless, it was expected as it has nearly 1.5 times less surface area.

LBM-10 showed a new topology compared to UTSA-90 (see chapter II). However, the new not always means better. LBM-10 showed less surface, therefore less adsorption versus UTSA-90. Also, despite being prepared like SUM-103m, the adsorption was not so high, it proves again indirectly the importance of the glyme chains.

The next tested MOF for CO_2 adsorption was SUM-401, based on magnesium and H4L1 ligand (Figure 72). Again the description of the structure and physico chemical parameters of the MOF is given in chapter II. SUM-401 like is H4L3 analogue SUM-403 not showed surface area. However, the CO_2 adsorption, is quite high, 14.3 mmol g^{-1}, with a desorption hysteresis.

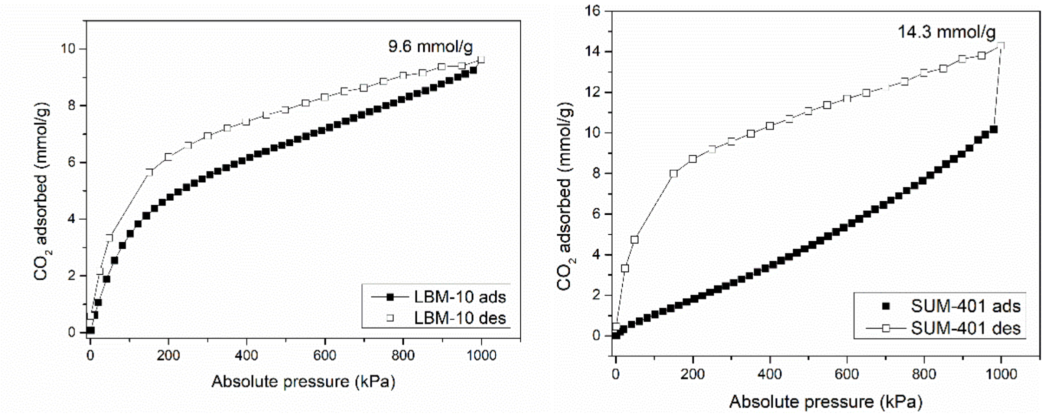

Figure 72. CO_2 adsorption isotherm of LBM-10 (left) and SUM-401 (right).

5) SUM-103@SBA-15 (Cu@H4L3/SBA-15)

Hybrid SUM-103@SBA-15 was also tested in the CO_2 adsorption. The latter hybrid was synthesized at 85°C, like SUM-103m. However, the TEM images and elemental mapping showed that MOF was inside the pores, which have a 10-15 nm diameter. Therefore, the size of crystals is much smaller than SUM-103m. However, as can be seen from SEM images and also some TEM images, some crystals were also located outside.

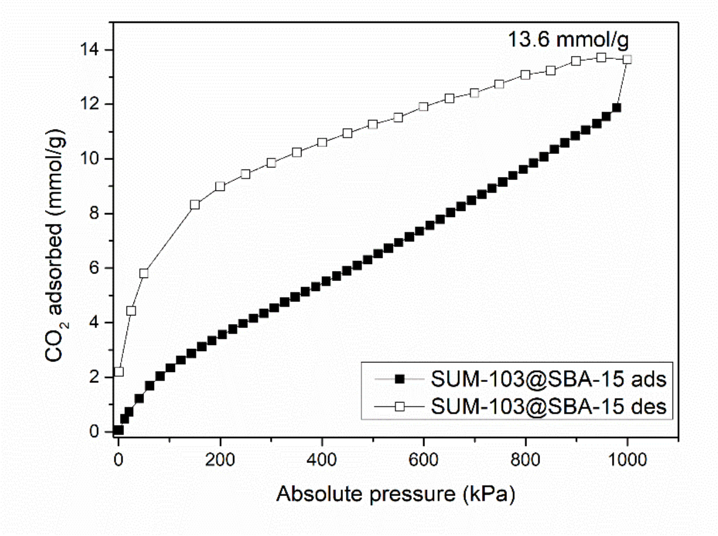

Figure 73. CO_2 adsorption isotherm of SUM-103@SBA-15.

Figure 73 shows a 13.6 mmol g^{-1} quantity of CO_2 adsorbed, being much less than SUM-103m, but still a compatible value. As it can be seen from TGA data (Figure 50), nearly 10% of the total mass is SBA-15, ~70% SUM-103 and ~20% is solvent. Thus, for dry hybrid, there is an 87% MOF and 13% SBA-15. The SBA-15 is a silica-based material that does not have significant interactions with CO_2 and also pore aperture of the SBA-15 is nearly 45 times wider than the kinetic diameter of the CO_2. Therefore, only the MOF content adsorbed the CO_2.

V. Conclusion

The synthesized materials were tested for adsorption of different guest molecules in different environments. The most stable MOFs in the aqueous environment SUM-102 and SUM-103 were used in the adsorption of dyes. They both exhibited decent adsorption of cationic and anionic dyes. With an increasing side chain, the adsorption of both dyes increased. Which is an indicator of the importance of the glyme chains. The maximum adsorption of cationic dye (methylene blue) at 30°C was 194 ± 4 mg g^{-1}.

Later, the same MOFs were tested in the adsorption of gaseous formaldehyde at small concentrations (164 ppb). In this case, we observed a reverse trend. The increased length of the chain decreased the adsorption. This could be related to a decrease in pore size and/or repulsion because MOFs side chains and also formaldehyde are hydrogen bond acceptors. Furthermore, SUM-102 showed high volumetric (based on pore volume) and surfacic (based on surface area) adsorption than other materials used [39], even nearly twice more than HKUST-1 a benchmark MOF for formaldehyde adsorption.

In conclusion, adding ethyleneoxy chains with different lengths, on one hand, allowed to creation of specific supramolecular interactions with host molecules and on the other hand, they controlled the pore size of the MOFs. Especially, the stability against the moisture (humidity) of the supramolecular MOFs allowed their use in an aqueous environment, which opens wide application domains for them. Thus, by varying interaction/size ratio, we successfully designed the adsorbents for dyes (methylene blue and methyl orange) in water, for gaseous formaldehyde, for CO_2 and even for N_2 (SUM-104).

The maximal methylene blue capture (Langmuir) was 194 ± 4 mg g^{-1}, which is less but comparable to benchmark MOFs. Slightly inferior adsorption of anionic dye was expected, however, in both cases, the MOF with a longer length of chain adsorbed more dye. This shows some supramolecular interactions involving glyme functional groups.

In the case of gaseous formaldehyde (164 ppb in synthetic air), if taken by surface area and/or pore volume SUM-102 showed even better results (up to twice) against benchmark MOF-HKUST-1. UTSA-90 and SUM-103 showed lower uptake compared to SUM-102. Let us remember that UTSA-90 has shorter and SUM-103 has longer chains than SUM-102. Therefore, for gaseous formaldehyde best interaction/size ratio MOF was SUM-102, adsorbing 1007 g m^{-3} of it.

For CO_2 adsorption tests, 3 different results were acquired over 3 different machines in 3 different countries. The first tests with ASAP-2050 showed a surprisingly high 38.5 mmol g^{-1} uptake for SUM-103m at 10 bar and 273K. Later the same material at 273K and 10 bar, with HidenIsochema IGA-001 showed 8.7 mmol g^{-1} uptake. Again the same material at 10 bar and 303K showed nearly 8.7 mmol g^{-1} CO_2 adsorption.

Later, with ASAP-2050 we performed CO_2 capture tests for most of our H4L3 based MOFs. Interestingly, not depending a lot on the metal core, all MOFs showed high adsorption. Especially high adsorption was observed with SUM-403 (Mg@H4L3) with 27 mmol g^{-1} uptake.

To finish, the high thermal and moisture stability, possibility to modify chain length (pore size, interactions) and obtained good results with various molecules shows a promising future for these materials.

References

1) J-M. Lehn, Supramolecular Chemistry: Concepts and Perspectives, Wiley, 1995.
2) N. Israfilov, K. Soukup, B. Louis and J.-M. Planeix, *New J. Chem.*, 2022, **46**, 8967–8970.
3) N. K. Gupta , Y. Ghaffari , S. Kim , J. Bae , K. S. Kim and M. Saifuddin , *Sci. Rep.*, 2020, **10** , 4942.
4) S. S. Auerbach , D. W. Bristol , J. C. Peckham , G. S. Travlos , C. D. Hébert and R. S. Chhabra , *Food Chem. Toxicol.*, 2010, **48** , 169-177
5) S. Rojas , J. A.-R. Navarro and P. Horcajada , *Dalton Trans.*, 2021, **50** , 2493.
6) K. A. Adegoke , O. S. Agboola , J. Ogunmodede , A. O. Araoye and O. S. Bello , *Mater. Chem. Phys.*, 2020, **253** , 123246.
7) W. Ren , J. Gao , C. Lei , Y. Xie , Y. Cai , Q. Ni and J. Yao , *Chem. Eng. J.,* 2018, **349** , 766-774.
8) L. Wang , H. Xu , J. Gao and Q. Zhang , *Coord. Chem. Rev.*, 2019, **398** , 213016.
9) S. Lin, Z. Song, G. Che, A. Ren, P. Li, C. Liu and J. Zhang, *Microporous and Mesoporous Materials*, 2014, **193**, 27–34.
10) A. S. Eltaweil, E. M. Abd El-Monaem, G. M. El-Subruiti, M. M. Abd El-Latif and A. M. Omer, *RSC Adv.*, 2020, **10**, 19008–19019.
11) E. Haque, V. Lo, A. I. Minett, A. T. Harris and T. L. Church, *J. Mater. Chem. A*, 2014, **2**, 193–203.
12) M. R. Azhar, H. R. Abid, H. Sun, V. Periasamy, M. O. Tadé and S. Wang, *Journal of Colloid and Interface Science*, 2017, **490**, 685–694.
13) A. A. Mohammadi , A. Alinejad , B. Kamarehie , S. Javan , A. Ghaderpoury , M. Ahmadpour and M. Ghaderpoori , *Int. J. Environ. Sci. Technol.*, 2017, **14** , 1959 — 1968.
14) E. Barea, C. Montoro and J. A. R. Navarro, *Chem. Soc. Rev.*, 2014, **43**, 5419–5430.
15) X. Han, W. Lu, Y. Chen, I. da Silva, J. Li, L. Lin, W. Li, A. M. Sheveleva, H. G. W. Godfrey, Z. Lu, F. Tuna, E. J. L. McInnes, Y. Cheng, L. L. Daemen, L. J. M. MPherson, S. J. Teat, M. D. Frogley, S. Rudić, P. Manuel, A. J. Ramirez-Cuesta, S. Yang and M. Schröder, *J. Am. Chem. Soc.*, 2021, **143**, 3153–3161.
16) T. Salthammer, S. Mentese and R. Marutzky, *Chem. Rev.*, 2010, **110**, 2536–2572.

17) N. L. Gilbert, M. Guay, D. Gauvin, R. N. Dietz, C. C. Chan and B. Lévesque, *Atmospheric Environment*, 2008, **42**, 2424–2428.

18) C. Wang, X.-F. Huang, Y. Han, B. Zhu and L.-Y. He, *Journal of Geophysical Research: Atmospheres*, 2017, **122**, 11,934-11,947.

19) T. Wangchuk, C. He, M. R. Dudzinska and L. Morawska, *Atmospheric Environment*, 2015, **113**, 151–158.

20) B. Wang, S. C. Lee and K. F. Ho, *Atmospheric Environment*, 2007, **41**, 2851–2861.

21) S.-C. Lee and B. Wang, *Atmospheric Environment*, 2004, **38**, 941–951.

22) W. Xiaoyan, W. Huixiang and W. Shaoli, *Atmospheric Environment*, 2010, **44**, 2074–2078.

23) T. Salthammer, *International Journal of Hygiene and Environmental Health*, 2015, **218**, 433–436.

24) M. Weng, L. Zhu, K. Yang and S. Chen, *Environmental Monitoring and Assessment*, 2010, **163**, 573–581.

25) C. Marchand, S. Le Calvé, Ph. Mirabel, N. Glasser, A. Casset, N. Schneider and F. de Blay, *Atmospheric Environment*, 2008, **42**, 505–516.

26) J.-Y. An, S. Kim and H.-J. Kim, *Journal of Hazardous Materials*, 2011, **187**, 44–51.

27) C. Trocquet, I. Lara-Ibeas, A. Schulz, P. Bernhardt, B. Cormerais, S. Englaro and S. Le Calvé, *Atmospheric Pollution Research*, 2021, **12**, 340–351.

28) N. L. Gilbert, D. Gauvin, M. Guay, M.-È. Héroux, G. Dupuis, M. Legris, C. C. Chan, R. N. Dietz and B. Lévesque, *Environmental Research*, 2006, **102**, 1–8.

29) L. Zhang, C. Steinmaus, D. A. Eastmond, X. K. Xin and M. T. Smith, *Mutation Research/Reviews in Mutation Research*, 2009, **681**, 150–168.

30) C. Yrieix, A. Dulaurent, C. Laffargue, F. Maupetit, T. Pacary and E. Uhde, *Chemosphere*, 2010, **79**, 414–419.

31) P. A. P. Mamza, E. C. Ezeh, E. C. Gimba and D. E. Arthur, 2014, **3**, 9.

32) P. Solt, J. Konnerth, W. Gindl-Altmutter, W. Kantner, J. Moser, R. Mitter and H. W. G. van Herwijnen, *International Journal of Adhesion and Adhesives*, 2019, **94**, 99–131.

33) K. B. Rumchev, J. T. Spickett, M. K. Bulsara, M. R. Phillips and S. M. Stick, *European Respiratory Journal*, 2002, **20**, 403–408.

34) D. Poppendieck, H. Hubbard, M. Ward, C. Weschler and R. L. Corsi, *Atmospheric Environment*, 2007, **41**, 3166–3176.

35) F. Rancière, C. Dassonville, C. Roda, A.-M. Laurent, Y. Le Moullec and I. Momas, *Science of The Total Environment*, 2011, **409**, 4480–4483.

36) J. Williams, H. Li, A. B. Ross and S. P. Hargreaves, *Atmospheric Environment*, 2019, **218**, 117019.

37) J. P. Porterfield, S. Eibenberger, D. Patterson and M. C. McCarthy, *Phys. Chem. Chem. Phys.*, 2018, **20**, 16828–16834.

38) M. Nicolas, O. Ramalho and F. Maupetit, *Atmospheric Environment*, 2007, **41**, 3129–3138.

39) Décret n° 2011-1727 du 2 décembre 2011 relatif aux valeurs-guides pour l'air intérieur pour le formaldéhyde et le benzène, 2011.

40) A. Becker, N. Israfilov, E. Ehrstein, I. Lara-Ibeas, J.-M. Planeix, B. Louis and S. Le Calvé, *Microporous and Mesoporous Materials*, 2022, **343**, 112136.

41) S. Nandi, P. D. Luna, T. D. Daff, J. Rother, M. Liu, W. Buchanan, A. I. Hawari, T. K. Woo and R. Vaidhyanathan, *Science Advances*, 2015, **1**, e1500421.

42) L. Ge, L. Wang, V. Rudolph and Z. Zhu, *RSC Adv.*, 2013, **3**, 25360–25366.

43) R. A. Maia, B. Louis, W. Gao and Q. Wang, *React. Chem. Eng.*, 2021, **6**, 1118–1133.

44) X.-Y. Li, Y.-Z. Li, L.-N. Ma, L. Hou, C.-Z. He, Y.-Y. Wang and Z. Zhu, *J. Mater. Chem. A*, 2020, **8**, 5227–5233.

45) C. R. C. Jensen and N. A. Seaton, "An Isotherm Equation for Adsorption to High Pressures in Microporous Adsorbents", 1996, **12**, **11**, 2866–2867.

General Conclusion

At the beginning of the project we put some fundamental questions: Can MOFs be efficiently prepared from ligands with supramolecular "recognition" functions? How does the presence of such functions influence the stability and the structural properties of these solids? Can these new materials be used in the main applications of porous materials such as gas or liquid phase adsorption, separation, or extraction? Do these new materials bring new or different properties? How do supramolecular interactions occur or are they at the origin of such properties?

To find an answer to these questions we synthesized and fully characterized 9 new ligands and more than 21 new MOFs and 4 hybrids. As there was a lot of materials bearing the name of different research centers such as HKUST (Hong-Kong University of Science and Technology), MIL (Materiaux Institut Lavoisier), UiO (University of Oslo) we decided to call our MOFs SUM (Strasbourg University Materials) and LBM (Le Bel Materials).

Our work shows that we can answer yes to the first question. We can prepare MOFs from supramolecular functionalized ligands. At least up to tetraglyme it is possible and we will continue to increase the size of glyme chains. But most probably it will be only for scientific purposes. Because, the price of di-, tri-, and tetra- glyme is not so expensive, however beginning from pentaglyme price increases exponentially. In the future, it is also possible to find some less expensive alternatives for glyme, bearing heteroatoms with a long chain.

We determined that adding aliphatic chains with oxygen atoms nearly not influenced thermal stability and increased considerably stability against humidity. The examples are NOTT-101 (ligand is without the chain) and SUM-103 (side chain is diglyme). NOTT-101 is not stable in water, also it is not stable after activation. On the other hand, SUM-103 is stable after activation and even stable in water (putting to water after activation). We observed also this stability in the example of the SUM-200 series (Ni@H4L), SUM-203 was stable in water, but not after activation (after activation in water).

Compared to known MOFs without the side chain, more precisely NOTT-101, no structural changes were observed. The main topology stayed the same with slight changes in torsion and bonding angles.

The next question was about the applicability of these materials. Firstly, the stability in an aqueous environment increased largely in the domain of application. The tests on SUM-103 for adsorption of cationic and anionic dye showed significant values, especially for cationic dye (methylene blue). Moreover, the increase in side chains led to better adsorption of both dyes. Another interesting feature of these materials was their extremely high CO_2 adsorption. It is a little bit discussable, hence 3 different analyses, in 3 different countries, made with 3 different devices showed different results, both in adsorptions and the trend of adsorptions. Most of our analyses were done with Micromeritics ASAP-2050 device and we obtained stunning results like 38.5 mmol g^{-1} for SUM-103 or 27 mmol g^{-1} for SUM-403 at 273K and 10 bar. In general H4L3 ligand-based MOFs, not depending on their topology gave high CO_2 adsorption, at least 14 mmol g^{-1}. It shows the important role of diglyme chains.

Furthermore, our MOFs, especially SUM-102 showed high formaldehyde adsorption. If compared by pore volume and/or by the specific surface area it largely outperforms a benchmark HKUST-1 MOF. Compared to zeolites its adsorption is much higher.

From our experiments, we can say that the new materials bring new and different properties. Such as high stability and high adsorption that we discussed just before.
Also, functionalization with fragments known to develop supramolecular interactions results in significant increases in the retention capacities and for a variety of substrates. We conclude at this stage of the studies that these specific properties are probably due to supramolecular interactions. Especially in the case of dye adsorption. However, the exact mechanism of these interactions has not been identified yet. Now we are working with another group on computer simulation of the adsorption of different guest molecules.

The first idea that comes while said “supramolecular” is the hydrogen-bonded big protein assemblies. However, the heart of supramolecular chemistry is the weak inter or intramolecular (or ionic) interactions, such as Van der Waals, hydrogen bonds, halogen bonds, π-π stacking, etc… Generally speaking, most of the simplest MOFs with terephthalic, biphenyl-4,4′-dicarboxylic acid and similar ligands were synthesized. Thus, the new “el-dorado” for MOFs is their modification with supramolecular groups. The first attempt to synthesize supramolecular MOFs could be considered the functionalization of MOFs with simple groups such as $-NH_2$[1], $-NO_2$[2], -COOH[3] groups. The electronic properties of these groups can create different kinds of weak interactions with guest molecules. Also, these kinds of interactions could be created by an ion. In the work of Bu and al. [4], the MOF named NKU-521 was doped with K ion, which increased the isosteric heat of adsorption of CO_2 up to 41 kJ mol^{-1}. Moreover, the presence of LBS (Lewis Base Sites) increases the adsorption of CO2 [5,6]. In our cases, numerous oxygen atoms could be considered LBS. As mentioned throughout the thesis, one of the reasons for the supramolecular functionalization of our MOFs was the creation of pseudo-crown ethers or cryptands inside the pores of the MOF. The next step as a continuation of this Ph.D. will be a Post-doc, where we will study the extraction of lithium from groundwater. The adsorption/separation of lithium ions from the water will be investigated. We already have the first results that our MOFs capture lithium ions. However, in this post-doc, we will study this process in more detail. Such as, how much it adsorbs? how much does it release? is it easy to regenerate? is the adsorption selective? etc. Moreover, there is a just published study with our SUM-602 (Zr@H2L2) and SUM-603 (Zr@H2L3) (they don't know that we have a patent) which is used as a medium for lithium-ion storage in batteries[7].

To conclude, we think that one of the main branches of MOFs development could be the synthesis (or post-synthetic modification) of MOFs with supramolecular groups, which will create more specific host-guest interactions by increasing the adsorption/separation capacity of the MOFs.

Ph.D. means a Philosophy doctor, therefore I decided, in conclusion, to touch a little bit on the philosophical side of my project. I think the one word which is crucial for our MOFs design and uses and also for supramolecular chemistry, thus life, is repeatability. In order to go from their separate constituents to MOFs, an immeasurable sequence of processes allows the scale factor to be crossed from nanometres to centimeters. How can one not marvel at such repeatability of arrangement leading ultimately to such special properties? And on all levels, macro, meso, micro, nano as shown in figure 73B where we observe the wing of a butterfly, where the left and right sides are chiral copies (so repeated twice) and we zoom (fig.73C) we see that these parts also consisted of a huge number of repeated units. This is similar somehow to fractals.

In most cases of MOFs we observe an elementary cell of the crystal (size of a nanometer) gave the same motif at the micro level (fig.74). In our case, we modified this repeating unit by adding glyme chains, which itself is repeating (mono, di, tri, and we plan to synthesize up to 8).

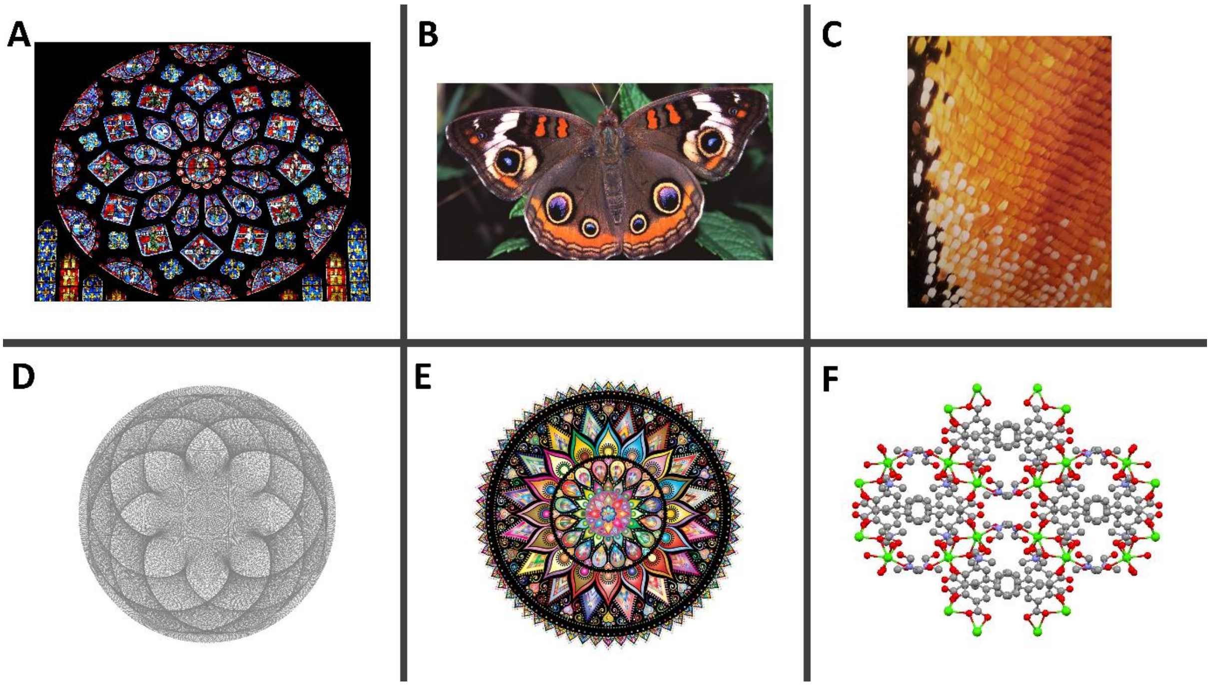

Figure 73. A-Rose window of Notre Dame de Paris; B- Butterfly; C- Butterfly's wing zoomed ; D- Pattern of Venus and Earth around the Sun; E- Mandala (used in Hindu religions); F- LBM-40.

In MOF design there are two popular approaches: Top-down and bottom-up. If we made an analogy between beauty/functionality and top-down synthesis. We can say that by creating more beautiful structures we can create more functional materials. But it is here of course more an ideal wish than a philosophical point of view. Therefore we can guess that by adding more and or different glyme chains (synthetically possible) we can obtain more functional MOFs. We can observe this when we pass to H4L3 and H4L4. Unexpectedly, Cu@H4L3 adsorbs an incredibly high amount of CO_2, and Cu@H4L4 adsorbs inert gases like nitrogen and argon, for H4L7 or H4L8 we will, we hope, soon write the rest of the story in the framework of a maturation project with various partners…

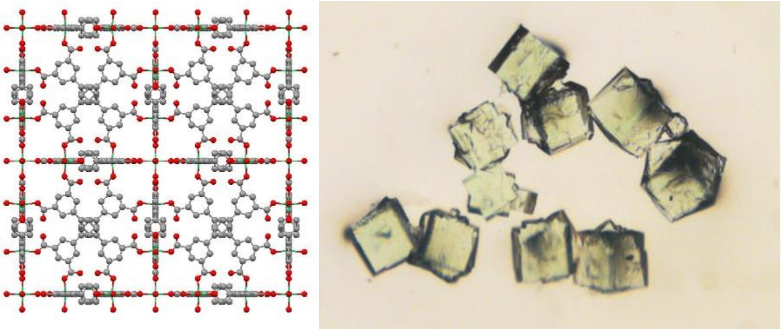

Figure 74. Left-4 cubic cell unit of SUM-200 (Ni@H4L1); Right- Micrograph of SUM-203 (Ni@H4L3).

Unfortunately, today scientific research seems to be more focused on commercializing MOFs by decreasing their price. Why not change the paradigm for once? Why not synthesize beautiful MOFs and later find some applications?

References

1. S. Choi, T. Watanabe, T.-H. Bae, D. S. Sholl and C. W. Jones, *J. Phys. Chem. Lett.*, 2012, **3**, 1136–1141.
2. D. K. Maity, A. Halder, B. Bhattacharya, A. Das and D. Ghoshal, *Crystal Growth & Design*, 2016, **16**, 1162–1167.
3. M. N. Ahamad, M. S. Khan, M. Shahid and M. Ahmad, *Dalton Trans.*, 2020, **49**, 14690–14705.
4. N. Li, Z. Chang, H. Huang, R. Feng, W.-W. He, M. Zhong, D. G. Madden, M. J. Zaworotko and X.-H. Bu, *Small*, 2019, **15**, 1900426.
5. J. Yu, L.-H. Xie, J.-R. Li, Y. Ma, J. M. Seminario and P. B. Balbuena, *Chem. Rev.*, 2017, **117**, 9674–9754.
6. N. MacDowell, N. Florin, A. Buchard, J. Hallett, A. Galindo, G. Jackson, C. S. Adjiman, C. K. Williams, N. Shah and P. Fennell, *Energy Environ. Sci.*, 2010, **3**, 1645–1669.
7. S. Shalini and A. J. Matzger, *Chem. Commun.*, 2022, **58**, 5355–5358.

Experimental Part

I. General methods

1H-NMR and 13C-NMR spectra were recorded at 25 °C on Brucker AV300 (300 MHz) Bruker AV400 (400 MHz) or Bruker AV500 (500 MHz) spectrometers in deuterated solvents with the residual solvent peak used as the internal reference (CDCl3: 7.26 ppm for 1H, 77.2 ppm for 13C; DMSO-d6: 2.50 ppm for 1H, 49.9 ppm for 13C).

The abbreviations for specifying the multiplicity of 1H-NMR signals are defined as follows: s = singlet, d = doublet, dd = doublet of doublet, ddd = doublet of doublet of doublets, t = triplet, q = quadruplet, m = multiplet, br = broad. Coupling constants are given in Hertz and chemical shifts in ppm.

MS (Mass spectrometry) was performed at the “Service de Spectrométrie de Masse” of the University of Strasbourg. Low (LRMS) (positive and negative mode ESI: Electro Spray Ionization) were recorded on Thermoquest AQA Navigator® with a time flight detector.

Elemental analyses were performed on a Thermo Scientific Flash 2000 by the "Service Commun de Microanalyse" of the University of Strasbourg.

UV-Vis spectrometry measurements were performed on a Perkin-Elmer Lambda 900 spectrophotometer in 1mm quartz cuvettes. Wavelength (λ) are given in nm. All solvents used were purchased as spectrometric grades.

Thermo gravimetric analysis (TGA) were performed on a Pyris 6 TGA Lab System apparatus (Perkin- Elmer), using a N2 flow of 20 mL/min and a heat rate of 5°/min.

Crystallization method: All commercial solvents used for crystallization were of analytical grades and used without further purification.

For crystallization under solvothermal conditions, a solution of reagents contained into a sealed glass vial (height 5 cm, diameter 1.5 cm) was heated by means of a dry bath VWR digital heatblock.

Liquid-Liquid diffusions technics were conducted in glass crystallization tubes (height= 15 cm, diameter= 0.4 cm) at ambient temperature.

X-Ray diffraction: Single-crystal data were collected on a Bruker SMART CCD diffractometer with Mo- Kα radiation at 173 K. The structures were solved using SHELXS-97 and refined by full matrix least- squares on F2 using SHELXL-2014 with anisotropic thermal parameters for all non-hydrogen atoms.

The hydrogen atoms were introduced at calculated positions and not refined (riding model). The SQUEEZE command has been employed when disordered solvent molecules were present in structures, to account for the corresponding electron density.

XRPD patterns: Powder X-ray diffraction (XRPD) data were recorded using a Bruker D8 AV diffractometer with Cu-Kα radiation at room temperature. The radiation wavelength λ of the incident X-rays was 1,54 Å and a 2θ range is from 5° to 30° was investigated.

Adsorption measurements: Nitrogen, Argon and carbon dioxide adsorption-desorption isotherms were measured at their respective condensing temperature, except CO_2 (77, 87 and 273 K) up to 1 bar using the ASAP 2020 Micromeritics analyzer. Nitrogen, and carbon dioxide isotherms up to 10 bars at 273 were performed by using the ASAP 2050 Micromeritics analyzer. Gravimetric CO_2 adsorption experiments were performed on the Hiden Isochema IGA-001 device at 273K and up to 20 bar. Also, some volumetric measurements (CO_2) were realized in a homemade device coupled with microcalorimetry at 303K and up to 40 bar.

Activation of the samples was achieved by heating them at 160 °C under a vacuum for 8h. The samples were degassed under a high vacuum (2 μmHg) and adequately thermally treated overnight before each measurement.

The surface area was calculated using Brunauer–Emmett–Teller (BET) and Langmuir method.

II. Formaldehyde adsorption calculations

The analytical method for formaldehyde adsorption is based on three highly coupled steps: i) uptake of gaseous formaldehyde into an aqueous acetylacetone solution at room temperature (gas and liquid flow rates set to 20 mL min^{-1} and 17 μL min^{-1}, respectively); ii) chemical reaction between formaldehyde and acetylacetone at 65°C via the Hantzsch reaction; and iii) on-line fluorescence detection of the reaction product, i.e., 3.5-diacetyl-1.4-dihydrolutidine (DDL), excited by a LED centered at 415 nm and fluorescence collected on a photomultiplier (Hamamatsu) coupled to a 530 ± 40 nm band pass filter. The commercial formaldehyde analyser (microF, Chromatotec, Val-de-Virvée, France) has a temporal resolution of 2 s, a response time of 10 min and a detection limit of about 1 μg m^{-3} (0.81 ppb). These data can be averaged to obtain time steps typically varying between 10 min and 1 hour. In this work, MOF data were averaged over 20 minutes. Each investigated material was introduced separately in a copper tube (1/8-inch outer diameter) where it was packed between two quartz wool plugs. The exact amount of adsorbent was weighted with a precision balance, with an error of 0.2 mg. This tube was then mounted in the experimental setup shown in Figure 75. To ensure a constant gaseous formaldehyde concentration of 164 ppb, a synthetic air flow (10 mL min^{-1}) was passed through a formaldehyde aqueous solution (0.0925 wt.%) maintained at 20°C thanks to a Peltier modulus and then diluted in a second synthetic air flow (390 mL min-1). A resulting formaldehyde gaseous flow of 164 ppb could therefore be generated. The resulting overall relative uncertainty of the pre-calibrated and generated gaseous concentration was calculated to be in the range of 9-11%. Before the adsorption experiments, the gas was flown through the bypass, diluted and analysed. The obtained intensity corresponds to the initial concentration (C_0) and, therefore, it was used as an indicator to determine when saturation was reached, i.e., when the outlet concentration was equal to the inlet concentration ($C = C_0$). All the adsorption experiments were performed at room temperature, i.e., 20 ± 3 °C.

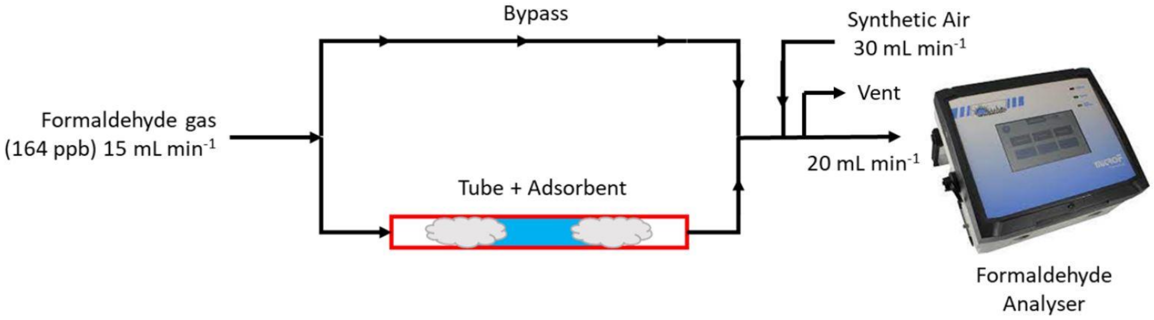

Figure 75. Experimental setup of formaldehyde adsorption.

Dynamic adsorption experiments were performed to obtain the corresponding breakthrough curves representing the evolution of the adsorbate concentration in the effluent leaving the adsorbent bed as a function of time. In air treatment, the breakthrough time is usually defined as the time in which 5% of the feed concentration (C_0) is leaving the adsorbent bed. Additionally, breakthrough curves allow determining the total adsorption capacity of each material. This capacity can be calculated from each curve using equation (1):

q=$\frac{QC_0}{m}\int_{t_0}^{ts}(1-\frac{C}{C_0})\,dt$ (1)

where q represents the dynamic adsorption capacity per gram of adsorbent, Q is the gas flow rate, m is the mass of adsorbent, t_0 corresponds to the initial time and ts to the saturation time, C_0 is the initial concentration, and C is the outlet concentration at a given time. The error in the calculation of the dynamic adsorption capacity was estimated according to Eq.2 :

$$\frac{\Delta q}{q}=\frac{\Delta Q}{Q}+\frac{\Delta C_0}{C_0}+\frac{\Delta t}{t}+\frac{\Delta m}{m} \quad (2)$$

where Δq is the error on the adsorption capacity. ΔQ is the error on the flow rate, ΔC_0 is the error on the initial concentration and Δm is the error on the adsorbent mass.

III. Dye adsorption calculations

The adsorption capacity of MB was calculated based on Equation (1)a-c . The equilibrium adsorption capacity of adsorbent was calculated using Equation (2)c .

$$Q_t=(C_0-C_t)\cdot\frac{V}{m} \quad (1)$$

$$Q_e=(C_0-C_e)\cdot\frac{V}{m} \quad (2)$$

where Q_t and C_t define the adsorption capacity of the adsorbent (mg g^{-1}) and the adsorbate concentration (mg L^{-1}), respectively. V represents the volume of adsorbate solution and m the mass of MOF adsorbent. Likewise, Q_e and C_e define the adsorption capacity of adsorbent and adsorbate concentration (mg L^{-1}), respectively, at the equilibrium conditions. The MB isotherms were fitted with Langmuir and Freundlich models in order to calculate the maximal adsorption capacity and get insights about the nature of the adsorption. Linear form of Langmuir equation is expressed as indicated below:

$$\frac{C_e}{Q_e}=\frac{1}{Q_mK_L}+\frac{C_e}{Q_mC_e} \quad (3)$$

C_e is the equilibrium concentration, Q_e is equilibrium uptake capacity. K_L and Q_m are obtained from the slope and the intercept of C_e/Q_e vs Q_e plot. The separation factor-R_L is calculated with Eq (4).

$R_L = \frac{1}{1+C_m K_L}$ (4)

C_m is maximal initial concentration of methylene blue. The R_L shows favorability of adsorption. The value between 0 and 1 shows good adsorption. To fit the data to Freundlich model the Eq (5) was used: (5) $lnQ_e = lnK_F + 1/n\ lnC_e$ To find K_F and 1/n (adsorption constants), the plot of lnQ_e vs lnC_e were drawn. In order to properly describe the adsorption process, two popular methods for studying the adsorption kinetics were applied: Pseudo-first order (PFO) and pseudo second order (PSO). Linear equation of PFO (6) and PSO (7) could be expressed as below:

$\ln(Q_e - Q_t) = lnQ_e - k_1 t$ (6)

$\frac{t}{Q_t} = \frac{t}{Q_e} + \frac{1}{K_2 Q_e^2}$ (7)

Q_e and Q_t are the amounts of methylene blue adsorbed (mg g^{-1}) on MOFs at equilibrium and at the time t, k_1(min^{-1}) and k_2 (g $mg^{-1}min^{-1}$) are the rate constants of PFO and PSO, respectively.

IV. MOLECULES SYNTHESIZED

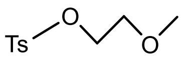

1

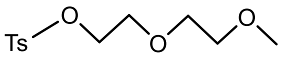

2

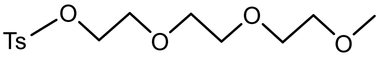

3

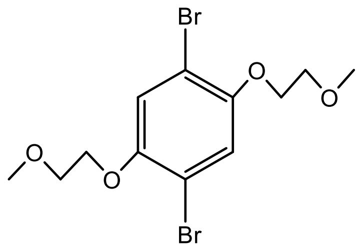

4

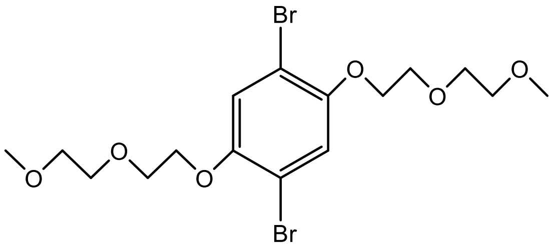

5

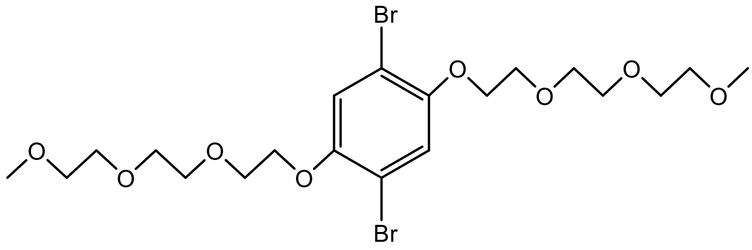

6

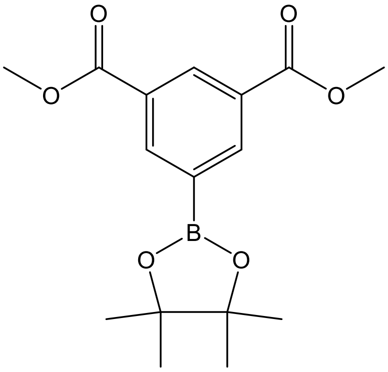

7

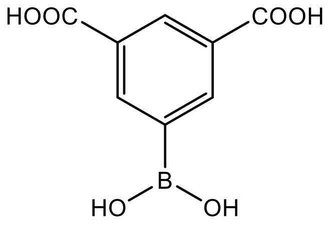

8

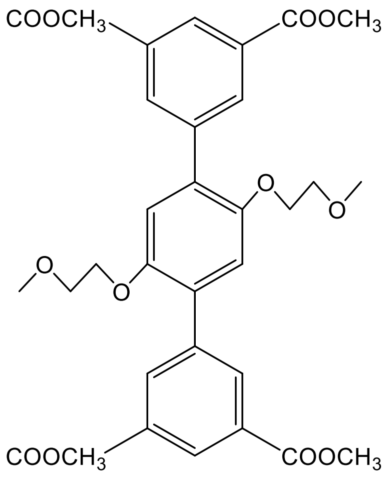

9

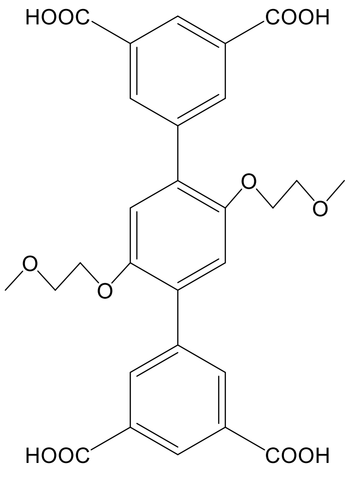

10

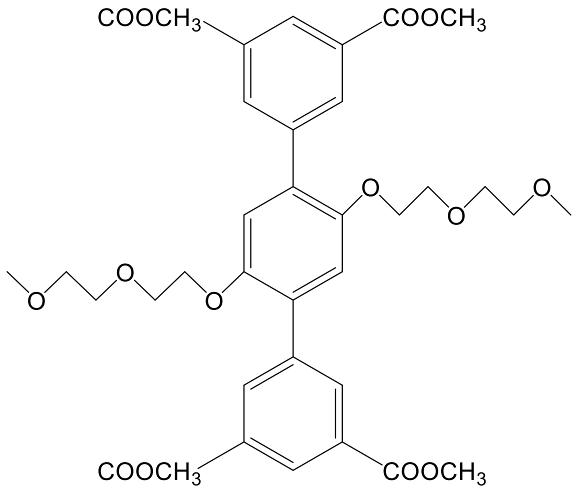
COOCH3
COOCH3
O
O
O
O
O
O
COOCH3
COOCH3

11

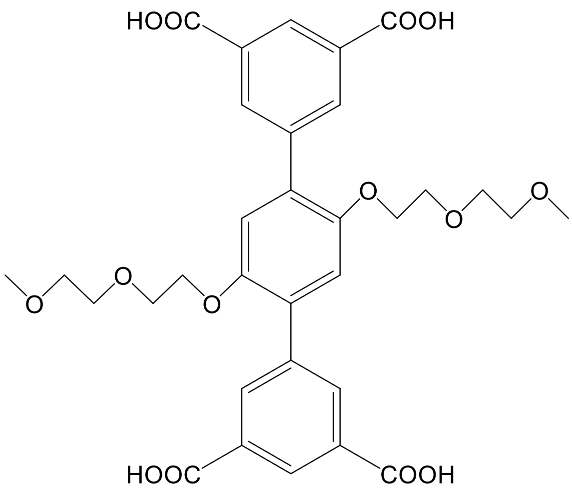
HOOC
COOH
O
O
O
O
O
O
HOOC
COOH

12

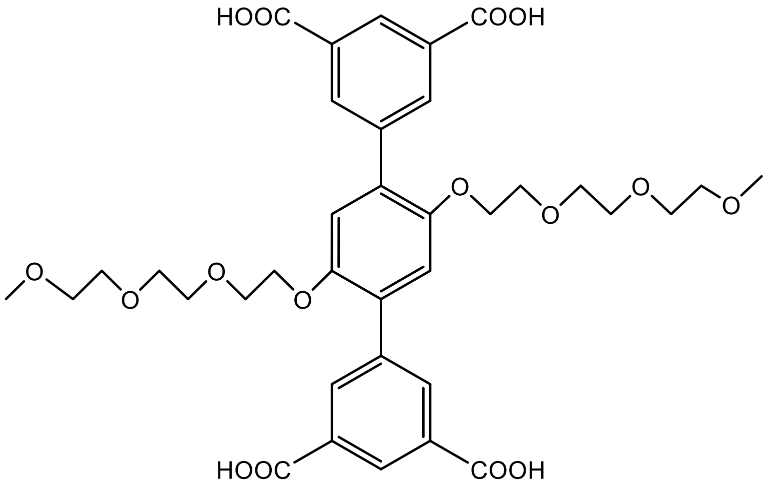
HOOC
COOH
O
O
O
O
O
O
O
O
HOOC
COOH

13

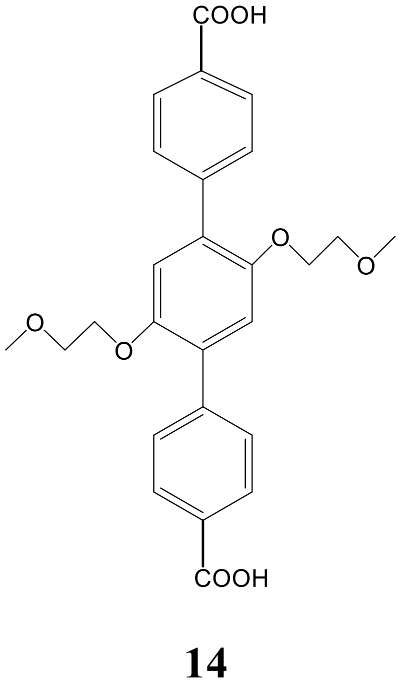
COOH
O
O
O
O
COOH

14

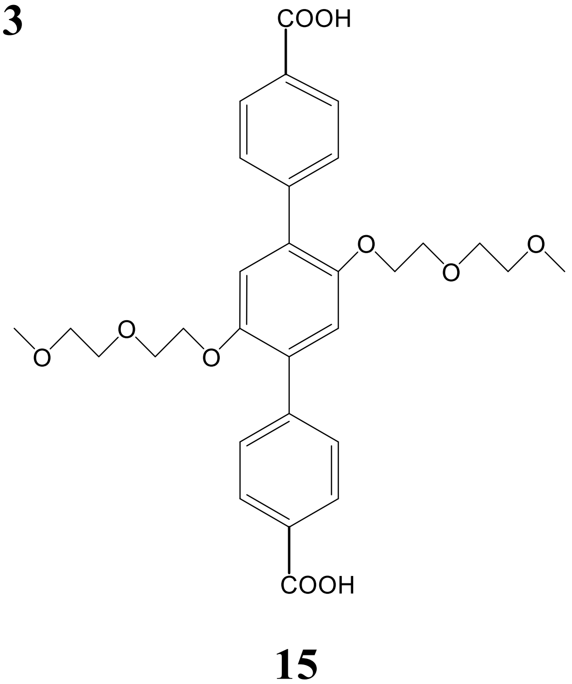
COOH
O
O
O
O
O
O
COOH

15

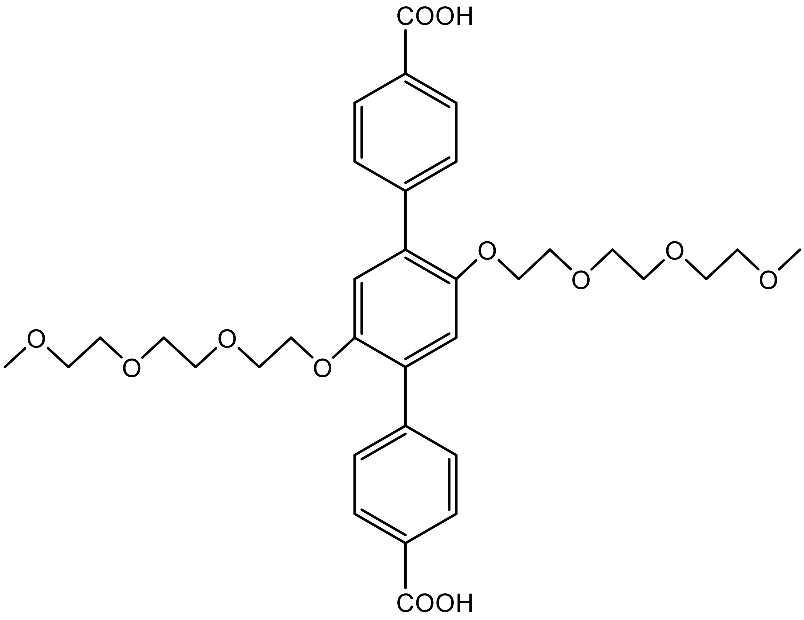

16

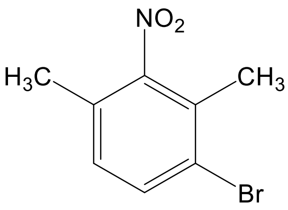

17

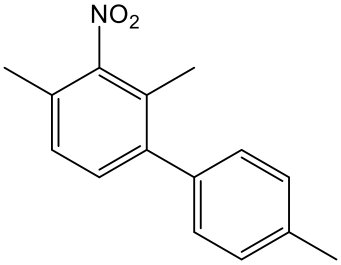

18

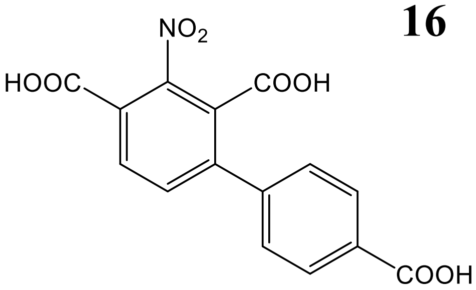

19

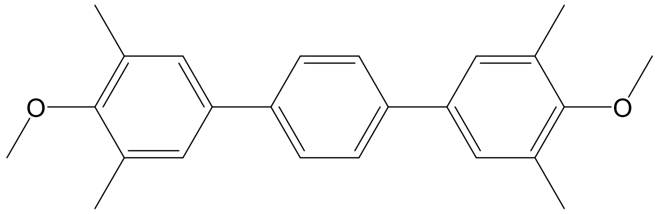

21

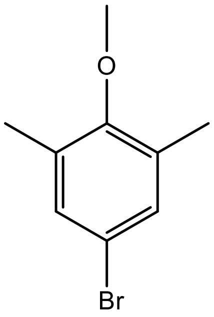

20

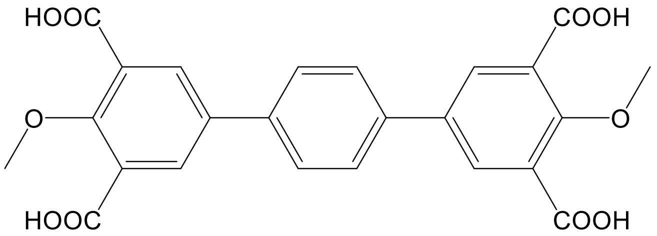

22

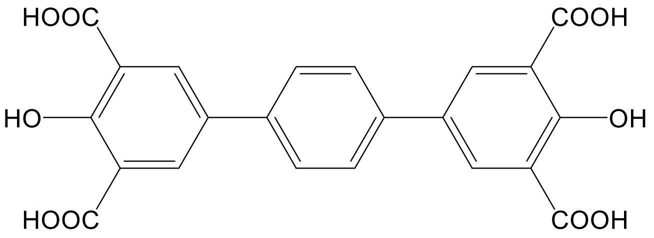

23

V. Synthesis and characterization of compounds

As mentioned earlier in chapter I, the synthesis procedures improved. Therefore, only one of the synthesis methods is given here.

General procedure for obtaining 1-3:

Double necked flask dried oven before reaction. In an ice bath, 2-(2-methoxyethoxy) ethanol (22 mmol) dissolved in CH_2Cl_2 under Argon atmosphere. Further, triethyleneamine (22 mmol) was poured into the flask. In a separate flask tosyl chloride (23 mmol) dissolved in CH_2Cl_2, a white cloudy solution was obtained. The solution of tosyl chloride was added dropwise to the mixture. Reaction continued overnight (18 h). 50 ml water was poured into the reaction mixture. The aqueous phase was washed with dichloromethane, the organic phase was collected and washed with 3 M HCl (50 ml), $NaHCO_3$ (50ml) and with water (50ml). Dried on $MgSO_4$, filtered and reduced.

The pale yellow oil was obtained and purified further with column (CH_2Cl_2/cyclohexane 1/1). The yield of compounds: ~80%

An improved method for 3 (applicable 1-3) :

Double necked flask dried oven before reaction. 2-(2-(2-methoxyethoxy)ethoxy)ethanol (9.9 mmol) dissolved in THF (20 mL) and water (15 mL) with NaOH (30 mmol). Later, tosyl chloride (10.5 mmol) was dissolved in THF (20 mL) and added dropwise to the mixture while mixing at ambient temperature. Despite THF and water being miscible, in our case (most probably because of NaOH) the layers were separated. After the overnight reaction, layers separated. Aqueous layer washed 2 times with diethyl ether and once with dichloromethane. The organic layer was washed twice with water. Organic layers combined, dried on $MgSO_4$ filtered with cotton and reduced. The pale yellow oil was obtained. Yield: 61%

General procedure for obtaining 4-6:

Double necked flask dried oven before reaction. Dibromohydroquinone (4.48 mmol), compound 1-3 (11.22 mmol) and potassium carbonate (26.88 mmol) were added to the flask. Then flask was evacuated and filled 3 times with Argon. Finally, DMF was added. Reaction continued overnight (18 h). Reaction mixture quenched with 120 ml water, white precipitation obtained. A small amount of benzoquinone gives brownish color. Product recrystallized to eliminate this color. The yield of compounds: ~70%

An improved method for 6 (applicable to 4-6) :

Double necked flask dried oven before reaction. Dibromohydroquinone (0.25 mmol), compound 3 (0.75 mmol) and potassium carbonate (1 mmol) were added to the flask. In presence of acetone (50 mL). Then the flask was evacuated and filled 2 times with Argon. Reaction mixture heated to reflux and gently evacuated and filled 2 times with Argon. One of the key points of this reaction is to prevent the formation of benzoquinone which gives a red color to the product even at trace amounts and decreases the yield of the reaction. After 2 days of reaction, the reaction mixture dried, and some water, methanol and excess NaOH were added and heated to 50°C for 5 min while mixing. Later, methanol evaporated, and the aqueous layer was washed twice with diethyl ether. Organic layers were combined and washed twice with water. Dried on $MgSO_4$, filtered and reduced. Yield for compound 6: 63%.

Procedure for obtaining 7:

Firstly, dimethyl 5- bromo-benzene-1,3-dicarboxylate (5.4 g, 20 mmol) was tared on a triple-necked round bottom flask. Under Ar atmosphere, bis-(pinacolato) diborane (6g, 23.6 mmol) and potassium acetate (oven dried) (5.6g, 57 mmol) were added respectively. Then, dry 1,4-dioxane (50ml) poured and solution degassed with Ar for 5 min. Finally, $Pd(dpff)_2Cl_2$ (0.2g, 0.27 mmol) added and mixture heated to 80°C. After 24h reaction stopped and the mixture was extracted with ethyl acetate (20ml). Organic layer dried over $MgSO_4$, filtered and reduced at vacuum. Obtained crude product purified with column (silica gel, ethyl acetate/petroleum ether, 1/8 v:v). The white powder was obtained with an 85% yield (5.427g, 17 mmol).

Procedure for obtaining 8:

In a 100 mL flask 3,5-Dimethylphenylboronic acid (3.33 mmol) dissolved in t-BuOH/water (20/15 mL). Later, NaOH (10 mmol) was added and the mixture was heated to reflux. $KMnO_4$ (27 mmol) was added portion-wise. After the overnight reaction, the mixture was filtered, and t-BuOH evaporated and acidified. Product filtered and fast rinsed with acetone. Snow white powder was obtained. Yield: 60%.

General procedure for obtaining 9 and 11:

Double necked flask dried oven before reaction. Compound 7 (6.25 mmol) and compound 4-6 (2.08 mmol) were tared, then 40 ml DMF was added under Argon atmosphere. After 20 min mixing under argon, Cesium carbonate (6.25 mmol) and Tetrakis(triphenylphosphine)palladium (0) (0.054 mmol) added and mixture heated. Reaction continued overnight.

Reaction mixture was dried under reduced pressure, extracted with chloroform and purified with the column. White solid obtained. Yield for compound 8: 79%, compound 10: 90%

Compound 9:

1H NMR (500 MHz, CDCl3) δ 8.67 (d, J = 1.7 Hz, 2H), 8.49 (d, J = 1.7 Hz, 4H), 7.07 (s, 2H), 4.13 (t, J = 4.7 Hz, 4H), 3.98 (s, 12H), 3.66 (t, J = 4.7 Hz, 4H), 3.34 (s, 6H). 13C NMR (126 MHz, CDCl3) δ 166.38, 150.39, 138.61, 134.90, 130.47, 129.71, 129.44, 116.28, 71.01, 69.32, 59.23, 52.47.

LRMS (ESI+) for compound 9 calculated: $C_{32}H_{34}O_{12}$, 610.21 found: $C_{28}H_{25}O_{12}Na$, 633.19

Elemental analysis (%) for $C_{32}H_{34}O_{12}$ calculated: C 62.95, H 5.61; found: C 60.52, H 5.54

Compound 11:

1H NMR (300 MHz, CDCl3) δ 8.67 (t, J = 1.6 Hz, 2H), 8.46 (d, J = 1.6 Hz, 4H), 7.05 (s, 2H), 4.19 – 4.12 (m, 4H), 3.98 (s, 12H), 3.76 (dd, J = 5.5, 4.3 Hz, 4H), 3.60 – 3.55 (m, 4H), 3.48 – 3.43 (m, 4H), 3.31 (s, 6H).

13C NMR (126 MHz, CDCl3) δ 166.33, 150.29, 138.70, 134.89, 130.46, 129.65, 129.41, 116.07, 71.88, 70.79, 69.68, 69.42, 59.02, 52.47

LRMS (ESI$^+$) for compound 11 calculated: $C_{36}H_{42}O_{14}$, 698.26, found $C_{36}H_{42}O_{14}Na$, 721.25

Elemental analysis (%) for $C_{36}H_{42}O_{14}$ calculated: C 61.88, H 6.06; found C 58.95, H 5.82

General procedure for obtaining 10 and 12:

Compound 8 or 10 (1.64 mmol) dissolved in the mixture of 100 ml THF and 100 ml aq. KOH (2M). Mixture heated to 90°C overnight. Once, the reaction mixture reached RT, THF evaporated under reduced pressure. Aqueous solution treated with 6M HCl to pH1. Precipitation filtered and washed with water. Dried under vacuum overnight. Yield for compound 9; 89%, compound 11; 95%

Compound 10:

1H NMR (300 MHz, DMSO) δ 13.29 (s, 4H), 8.46 (t, J = 1.6 Hz, 2H), 8.42 (d, J = 1.6 Hz, 4H), 7.25 (s, 2H), 4.24 – 4.15 (m, 4H), 3.63 – 3.54 (m, 4H), 3.22 (s, 6H).

13C NMR (126 MHz, DMSO) δ 167.12, 150.23, 138.70, 134.67, 131.67, 129.22, 129.08, 116.25, 70.93, 69.07, 58.68.

LRMS (ESI+) for compound 10 calculated: $C_{28}H_{2}6O_{12}$,554.14 found: $C_{28}H_{25}O_{12}$, 553.14

Elemental analysis (%) for $C_{28}H_{2}6O_{12}$ calculated: C 60.65, H 4.46; found: C 52.46, H 4.73.

Compound 12:

1H NMR (500 MHz, DMSO) δ 13.31 (s, 4H), 8.45 (t, J = 1.7 Hz, 2H), 8.38 (d, J = 1.6 Hz, 4H), 7.23 (s, 2H), 4.20 – 4.15 (m, 4H), 3.67 – 3.62 (m, 4H), 3.46 (dd, J = 5.8, 3.8 Hz, 4H), 3.33 (d, J = 2.1 Hz, 4H), 3.14 (s, 6H).

13C NMR (126 MHz, DMSO) δ 167.13, 150.24, 138.75, 134.66, 131.62, 129.33, 129.07, 116.33, 71.60, 70.18, 69.48, 69.46, 58.37.

LRMS (ESI+) for compound 12 calculated: $C_{32}H_{34}O_{14}$ 642.19 found: $C_{32}H_{34}O_{14}K$ 681.16 (one K atom plus)

Elemental analysis (%) for $C_{32}H_{34}O_{14}$ calculated: C 59.81, H 5.33; found: C 58.13, H 5.18

Procedure for obtaining 13 (applicable to all final ligands):

Double necked flask dried oven before reaction. Compound 6 (0.107 mmol) and compound 8 (0.24 mmol) were tared, then 10 ml ethanol and 5 ml water were added under Argon atmosphere. After 20 min mixing under argon, Potassium carbonate (0.47 mmol) and Tetrakis(triphenylphosphine)palladium (0) (0.017 mmol) added and mixture refluxed. Reaction continued overnight.

Reaction mixture filtered over celite. Ethanol from the mixture is evaporated, and later some water is added followed by acidification with concentrated HCl. White slightly yellow solid filtered and rinsed with water and acetone. Yield for compound 12: 52%,

Compound 13:

1H NMR (300 MHz, DMSO) δ 8.45 (t, J = 1.6 Hz, 2H), 8.38 (d, J = 1.6 Hz, 4H), 7.23 (s, 2H), 4.17 (dd, J = 4.2, 2.2 Hz, 4H), 3.66 (dd, J = 5.4, 3.7 Hz, 4H), 3.47 – 3.45 (m, 4H), 3.38 (d, J = 1.0 Hz, 4H), 3.33 (d, J = 2.5 Hz, 4H), 3.31 (d, J = 1.2 Hz, 4H), 3.17 (s, 6H). (Because water molecule peaks were slightly "mixed")

13C NMR (126 MHz, DMSO) δ 167.10, 150.22, 138.76, 134.67, 131.63, 129.28, 129.07, 116.30, 71.61, 70.39, 70.12, 69.92, 69.47, 69.41, 58.42.

LRMS (ESI+) for compound 13 calculated: $C_{36}H_{42}O_{16}$, 730.25; found: $C_{36}H_{41}O_{16}$, 729.24

Elemental analysis (%) for $C_{36}H_{42}O_{16}$ calculated: C 59.17, H 5.79; found: C 57.39, H 5.63.

General procedure for obtaining 14-16:

Double necked flask dried oven before reaction. Compound 4-6 (1 eq) and 4-carboxyphenylboronic acid (3 eq) was tared, then ethanol and water were added (2/1: V/V) under Argon atmosphere. After 20 min mixing under argon, Potassium carbonate (6 eq) and Tetrakis(triphenylphosphine)palladium (0) (0.1 eq) added and mixture refluxed. Reaction continued overnight.

Reaction mixture filtered over celite. Ethanol from the mixture is evaporated, and later some water is added followed by acidification with concentrated HCl. White slightly brown solid filtered and rinsed with water, acetone and diethyl ether. Yield for compound 14: 89%, compound 15: 68%, compound 16: 80%.

Compound 14:

1H NMR (500 MHz, DMSO) δ 12.97 (s, 2H), 8.01 – 7.96 (m, 4H), 7.78 (d, J = 8.3 Hz, 4H), 7.15 (s, 2H), 4.19 – 4.14 (m, 4H), 3.63 – 3.57 (m, 4H), 3.25 (s, 6H).

13C NMR (126 MHz, DMSO) δ 167.24, 149.80, 142.04, 129.55, 129.42, 129.25, 128.98, 115.93, 70.49, 68.44, 58.23.

LRMS (ESI+) for compound 14 calculated: $C_{26}H_{26}O_8$, 466.16; found: $C_{26}H_{25}O_8$, 465.16

Elemental analysis (%) for $C_{26}H_{26}O_8$ calculated: C 66.94, H 5.62; found: C 62.88, H 5.30.

Compound 15:

1H NMR (500 MHz, DMSO) δ 12.96 (s, 2H), 8.02 – 7.96 (m, 4H), 7.84 – 7.78 (m, 4H), 7.17 (s, 2H), 4.20 – 4.14 (m, 4H), 3.71 – 3.64 (m, 4H), 3.55 – 3.49 (m, 4H), 3.44 – 3.39 (m, 4H), 3.21 (s, 6H).

^{13}C NMR (126 MHz, DMSO) δ 167.17, 149.70, 141.94, 129.51, 129.29, 129.11, 128.88, 115.80, 71.26, 69.61, 68.88, 68.50, 57.99.

LRMS (ESI+) for compound 15 calculated: $C_{30}H_{34}O_{10}$, 554.22; found: $C_{30}H_{34}O_{10}K$, 593.18

Elemental analysis (%) for $C_{30}H_{34}O_{10}$ calculated: C 64.97, H 6.18; found: C 64.67, H 6.04.

Compound 16:

1H NMR (500 MHz, DMSO) δ 12.90 (s, 2H), 7.98 (dd, J = 8.4, 1.6 Hz, 4H), 7.79 (dd, J = 8.3, 1.8 Hz, 4H), 7.16 (s, 2H), 4.17 (dd, J = 5.8, 3.4 Hz, 4H), 3.72 – 3.66 (m, 4H), 3.53 – 3.51 (m, 4H), 3.50 – 3.48 (m, 4H), 3.47 (dd, J = 5.7, 3.7 Hz, 4H), 3.39 – 3.38 (m, 4H), 3.19 (s, 6H). (Because water molecule peaks were slightly “mixed”)

13C NMR (126 MHz, DMSO) δ 167.76, 150.21, 131.92, 129.99, 129.82, 129.41, 129.20, 116.30, 71.70, 70.37, 70.32, 70.06, 69.43, 69.01, 58.48.

LRMS (ESI+) for compound 16 calculated: $C_{34}H_{42}O_{12}$ 642.27; found: $C_{34}H_{41}O_{12}$, 641.26

Elemental analysis (%) for $C_{34}H_{42}O_{12}$ calculated: C 63.54, H 6.59; found: C 63.90, H 6.45.

Procedure for obtaining 17:

In a 100 ml round bottom flask 1,3-dimethyl-2-nitrobenzene (33 mmol) dissolved in 20 ml CH_2Cl_2 in an ice bath. Later, separately bromine (36 mmol) was dissolved in 10 ml CH_2Cl_2 and added dropwise under an inert atmosphere. After addition flask coated with aluminum foil and iron powder was added (10 mmol). Finally, the mixture refluxed at 39°C. After 2 hours reaction stopped, the mixture filtered over celite quenched with 25 ml water, and the organic phase separated. Aqueous phase washed twice with 15 ml CH_2Cl_2. Organic phases were collected and washed twice with brine. Dried over $MgSO_4$. Reduced under vacuum, the slightly yellowish powder was obtained. Yield: 90%.

Ref: J. Med. Chem, 2018,61,16, 7201-7217

Procedure for obtaining 18:

Compound 16 (4,65 mmol) and 4-methylphenylboronic acid (4.5 mmol) tared, later under inert atmosphere 45 ml DMF and 15 ml water. After Cs_2CO_3 (13.2 mmol) and Tetrakis(triphenylphosphine)palladium (0) (0.05 mmol) mixture refluxed. Reaction continued overnight, later mixture evaporated completely and was extracted with water (product is not soluble), fast rinsed with methanol. Yield: 77%.

Compound 18:

1H NMR (300 MHz, CDCl3) δ 7.25 (dd, J = 1.4, 0.7 Hz, 1H), 7.22 (dd, J = 1.4, 0.7 Hz, 2H), 7.17 (d, J = 2.0 Hz, 2H), 7.15 – 7.13 (m, 1H), 2.41 (s, 3H), 2.33 (d, J = 0.6 Hz, 3H), 2.17 (s, 3H).

Elemental analysis (%) for $C_{15}H_{15}NO_2$ calculated: N 5.81, C 74.67, H 6.27; found: N 5.56 C 73.22, H 6.09.

Procedure for obtaining 19:

1.5 mmol compound 17 dissolved in 20 ml pyridine, later 10 ml water added. Mixture refluxed and $KMnO_4$ (45 mmol) added portion-wise. Reaction continued overnight, later mixture was filtered, reduced, extracted with water, acidified with HCl, filtered, and rinsed with water. The yield of compound 18: 67%.

Compound 19:

1H NMR (300 MHz, DMSO) δ 13.63 (d, J = 284.0 Hz, 3H), 8.11 – 7.40 (m, 6H). (Peaks were very close to each other)

13C NMR (126 MHz, DMSO) δ 167.49, 152.83, 144.08, 140.42, 131.77, 130.47, 129.98, 129.87, 129.44, 128.98, 128.73, 126.29.

LRMS (ESI+) for compound 19 calculated: $C_{15}H_9NO_8$, 331.03; found: $C_{15}H_8NO_8$, 330.02

Elemental analysis (%) for : $C_{15}H_9NO_8$ calculated: N 4.23, C 54.39, H 2.74; found: N 4.17 C 56.19, H 3.35.

Procedure for obtaining 20:

10 mmol 4-bromo-2,6-xylenol dissolved in 45 ml acetone, later 14 ml dimethyl sulfate and 50 mmol K_2CO_3 were added and refluxed. The reaction is quite fast but it stopped overnight. Reaction mixture evaporated, extracted with ethyl acetate, washed with 40 ml water and 40 ml brine, dried over $MgSO_4$, and reduced. Yellow oil with a humid wood odor was obtained. Yield 93%

ACS, Appl Mater, interfaced 2014, 6, 22, 20557-20568.

Procedure for obtaining 21:

Compound 19 (4.65 mmol) and benzene-1,4-diboronic acid (2.2 mmol) dissolved in 45 ml DMF and 15 ml water under an inert atmosphere. Later Cs_2CO_3 (6.7 mmol) and Tetrakis(triphenylphosphine)palladium (0) (0.02 mmol) added and mixture refluxed overnight. After some time white beautiful floating crystals appear in the solution. This makes it easy to separate the product because it was the product. The reaction mixture was just filtered and rinsed with water. Yield for compound 20: 60%.

Compound 21:

1H NMR (500 MHz, CDCl3) δ 7.59 (s, 4H), 7.28 (s, 4H), 3.77 (s, 6H), 2.37 (s, 12H).

13C NMR (126 MHz, CDCl3) δ 156.73, 139.59, 136.47, 131.30, 127.59, 127.32, 59.96, 16.44.

LRMS (ESI+) for compound 21 calculated: $C_{24}H_{26}O_2$, 346.19; found: $C_{24}H_{27}O_2$, 347.20

Elemental analysis (%) for : $C_{24}H_{26}O_2$ calculated: C 83.20, H 7.56; found: C 82.24, H 7.46.

Procedure for obtaining 22:

0.92 mmol of compound 20 dissolved in the mixture of pyridine/water (20/10 ml) and refluxed. Later $KMnO_4$ (40 mmol) was added portion-wise. After an overnight reaction, the mixture was filtered and rinsed with KOH solution. Filtrate dried under a rotary evaporator, extracted with water and acidified with HCl (12M). White product filtered and rinsed with water. The yield of compound 21: 64%.

Compound 22:

1H NMR (300 MHz, DMSO) δ 13.24 (s, 4H), 8.11 (s, 4H), 7.81 (s, 4H), 3.86 (s, 6H).

13C NMR (126 MHz, DMSO) δ 167.03, 157.16, 137.43, 134.69, 131.14, 128.53, 127.41, 63.15.

LRMS (ESI+) for compound 22 calculated: $C_{24}H_{18}O_{10}$, 466.09; found $C_{24}H_{18}O_{10}Na$, 489.08

Elemental analysis (%) for : $C_{24}H_{18}O_{10}$ calculated: C 61.81, H 3.89; found: C 59.16, H 3.86.

Procedure for obtaining 23:

Under nitrogen atmosphere, 0.2 mmol of compound 21 was mixed with 5 ml HBr solution in CH_3COOH and 5 ml CH_3COOH and heated to 90^oC for 2 hours. The reaction mixture evaporated and was washed with water. The white, slightly brownish powder was obtained. The yield of compound 22: 71%

Compound 23:

1H NMR (300 MHz, DMSO) δ 8.25 (s, 4H), 7.71 (s, 4H).

13C NMR (126 MHz, DMSO) δ 169.53, 161.94, 137.60, 133.54, 129.47, 127.25, 118.35.

LRMS (ESI+) for compound 23 calculated: $C_{22}H_{14}O_{10}$, 438.06; found $C_{22}H_{13}O_{10}$, 437.05

Elemental analysis (%) for $C_{22}H_{14}O_{10}$, calculated: C 60.28, H 3.22; found: C 57.43, H 3.34.

Crystallization methods and crystallographic data

You will see that for some MOFs there is less information than others. This is due to problems such as weak diffraction, high disorder, low-quality crystals, etc.

1) Network SUM-201 or Ni@H4L1. SUM-200, 202,203 and 204 have the same PXRD

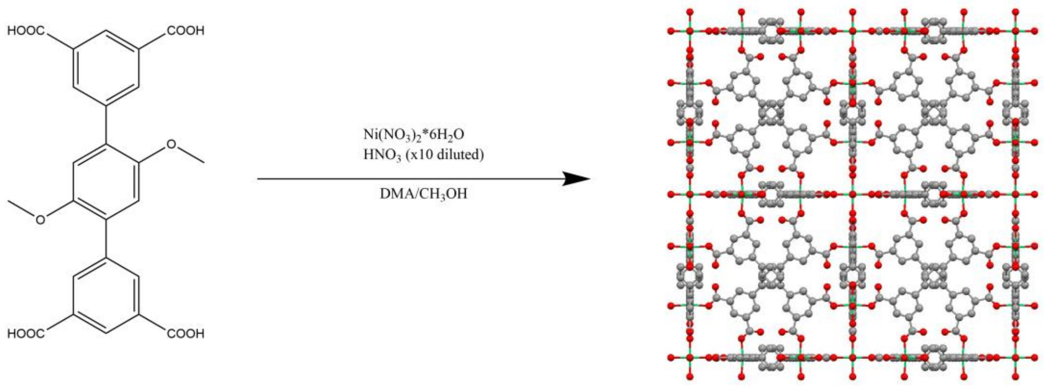

Crystallization conditions: heating of DMA/CH_3OH solution (1/1 mL) of **H4L1** (4 mg, 1 eq) and $Ni(NO_3)_2$*$6H_2O$ (10 mg, 6.4 eq) and 2 drops of HNO_3 (x10 diluted in water) at 100 °C for 24 h. *for SUM-202: DMA/ CH_3OH (0.5/1 mL)

Formula	**$C_{24} H_{18} N_2 Ni O_{16}$**
Space group	**F m -3 m**
Cell lengths	**a** 34.6639(10) **b** 34.6639(10) **c** 34.6639(10)
Cell angles	**a** 90 **b** 90 **g** 90
Cell volume	41651.7
Z	**Z**: 56
R factor (%)	38.42

2) Network SUM-401 or Mg@H4L1.

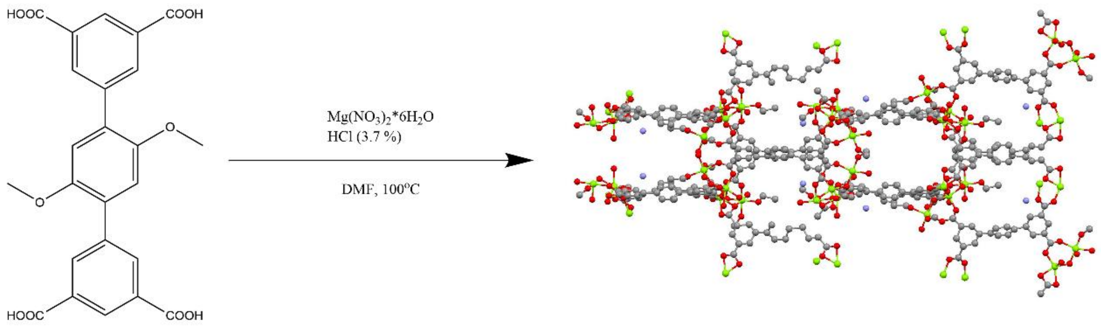

Crystallization conditions: heating of DMF solution (3 mL) of **H4L1** (2 mg, 1 eq) and $Mg(NO_3)_2 \cdot 6H_2O$ (6 mg, 5.5 eq) and 3 drops of HCl (3.7 %) at 100 °C for 24 h.

Formula	
Space group	**I -4**
Cell lengths	**a** 18.9287(8) **b** 18.9287(8) **c** 54.703(4)
Cell angles	**a** 90 **b** 90 **g** 90
Cell volume	19599.9
Z	
R factor (%)	

3) Network SUM-102 or Cu@H4L2. SUM-103 and SUM-104 has the same PXRD

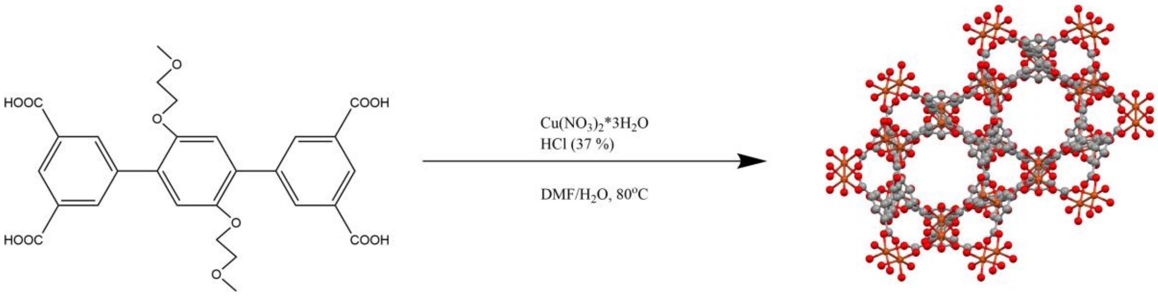

Crystallization conditions: heating of DMF/H_2O solution (4/1.3 mL) of **H4L2 or 10** (10 mg, 1 eq) and $Cu(NO_3)_2*3H_2O$ (17.9 mg, 4.1 eq) and 33 μL of HCl (37%) at 80 °C for 24 h. *The same topology crystals were obtained with $Zn(NO_3)_2*6H_2O$ (4.1 eq) with H4L3 or **12** (1 eq) in DMF (2 mL).

Chemical formula	$C_{14}H_{15}CuO_7$	
Formula weight	358.80 g/mol	
Temperature	173(2) K	
Wavelength	0.71073 Å	
Crystal system	trigonal	
Space group	R -3 m	
Unit cell dimensions	a = 18.5565(7) Å	α = 90°
	b = 18.5565(7) Å	β = 90°
	c = 38.7407(16) Å	γ = 120°
Volume	11552.9(10) $Å^3$	
Z	2	
Density (calculated)	0.103 g/cm^3	
Absorption coefficient	0.097 mm^{-1}	
F(000)	368	
Theta range for data collection	1.37 to 27.48°	
Index ranges	-23<=h<=24, -22<=k<=23, -50<=l<=50	
Reflections collected	36566	
Independent reflections	3224 [R(int) = 0.0884]	
Refinement method	Full-matrix least-squares on F^2	
Data / restraints / parameters	3224 / 2 / 107	
Goodness-of-fit on F^2	0.882	
Δ/σ_{max}	0.004	
Final R indices	2575 data; I>2σ(I)	R1 = 0.0865, wR2 = 0.2479
	all data	R1 = 0.1040, wR2 = 0.2680
Largest diff. peak and hole	1.440 and -1.076 e$Å^{-3}$	

4) Network SUM-403 or Mg@H4L3.

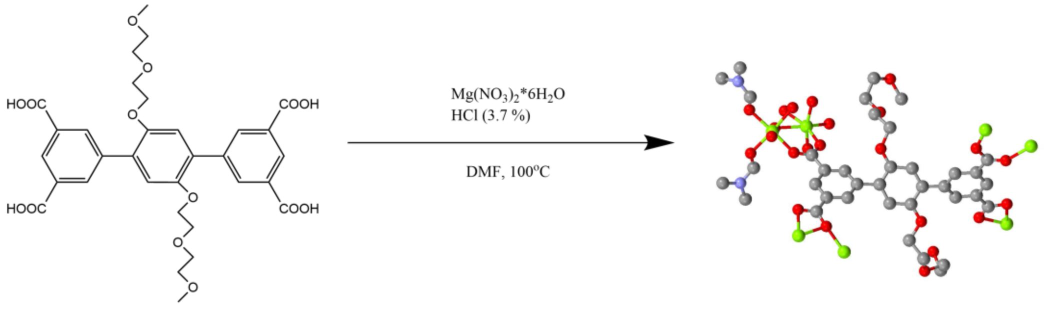

Crystallization conditions: heating of DMF solution (2 mL) of **H4L3 or 12** (3 mg, 1 eq) and $Mg(NO_3)_2*6H_2O$ (12 mg, 10 eq) and 2 drops of HCl (3.7 %) at 100 °C for 24 h.

Chemical formula	$C_{19}H_{23}MgNO_{8.50}$	
Formula weight	425.69 g/mol	
Temperature	173(2) K	
Wavelength	0.71073 Å	
Crystal size	0.120 x 0.130 x 0.140 mm	
Crystal system	monoclinic	
Space group	P 1 21 1	
Unit cell dimensions	a = 10.0803(12) Å	α = 90°
	b = 18.2435(18) Å	β = 101.595(5)°
	c = 14.2050(17) Å	γ = 90°
Volume	2559.0(5) $Å^3$	
Z	4	
Density (calculated)	1.105 g/cm^3	
Absorption coefficient	0.108 mm^{-1}	
F(000)	896	
Theta range for data collection	1.46 to 28.13°	
Index ranges	-13<=h<=13, -23<=k<=21, -18<=l<=18	
Reflections collected	31265	
Independent reflections	11883 [R(int) = 0.1269]	
Max. and min. transmission	0.9870 and 0.9850	
Data / restraints / parameters	11883 / 45 / 659	
Goodness-of-fit on F^2	1.279	
Δ/σ_{max}	4.676	
Final R indices	6799 data; I>2σ(I)	R1 = 0.1119, wR2 = 0.2495
	all data	R1 = 0.1868, wR2 = 0.2840
Largest diff. peak and hole	0.781 and -0.585 $eÅ^{-3}$	

5) Network LBM-10 or Cu@H4LOMe

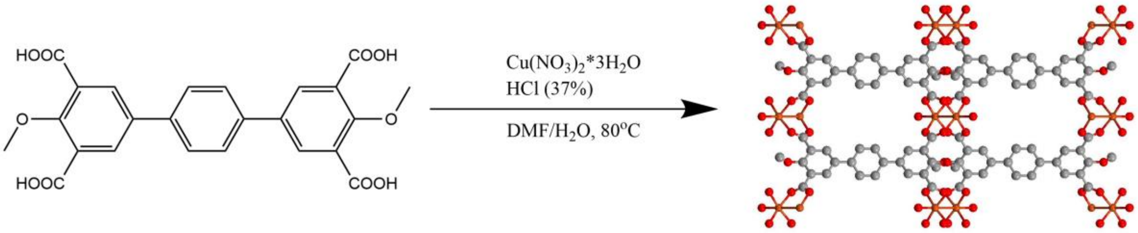

Crystallization conditions: heating of DMF/H_2O solution (4/1.3 mL) of **H4LOMe or 22** (8.4 mg, 1 eq) and $Cu(NO_3)_2*3H_2O$ (18 mg, 4.1 eq) and 33 µL of HCl (12 M) at 80 °C for 24 h.

Chemical formula	$C_{12}H_{10}CuO_7$	
Formula weight	329.74 g/mol	
Temperature	173(2) K	
Wavelength	0.71073 Å	
Crystal size	0.100 x 0.120 x 0.120 mm	
Crystal system	orthorhombic	
Space group	I m m a	
Unit cell dimensions	a = 16.1111(11) Å	α = 90°
	b = 27.702(3) Å	β = 90°
	c = 9.9992(7) Å	γ = 90°
Volume	4462.7(6) $Å^3$	
Z	8	
Density (calculated)	0.982 g/cm^3	
Absorption coefficient	0.995 mm^{-1}	
F(000)	1336	
Theta range for data collection	1.47 to 30.23°	
Index ranges	-22<=h<=22, -39<=k<=39, -14<=l<=12	
Reflections collected	45848	
Independent reflections	3481 [R(int) = 0.0683]	
Max. and min. transmission	0.9070 and 0.8900	
Data / restraints / parameters	3481 / 1 / 105	
Goodness-of-fit on F^2	1.234	
Δ/σ_{max}	0.082	
Final R indices	2369 data; I>2σ(I)	R1 = 0.0934, wR2 = 0.2753
	all data	R1 = 0.1298, wR2 = 0.3170
Largest diff. peak and hole	2.336 and -1.290 $eÅ^{-3}$	
R.M.S. deviation from mean	0.328 $eÅ^{-3}$	

6) Network LBM-30 or Ca@H4LOMe

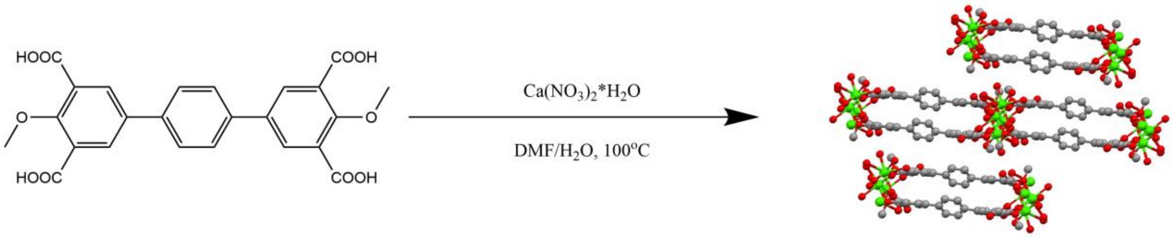

Crystallization conditions: heating of DMF/H_2O solution (2/1 mL) of **H4LOMe or 22** (4 mg, 1 eq) and $Ca(NO_3)_2*H_2O$ (10 mg, 7 eq) at 100 °C for 24 h.

Chemical formula	$C_{24}H_{14}Ca_2O_{20}$	
Formula weight	702.51 g/mol	
Temperature	173(2) K	
Wavelength	0.71073 Å	
Crystal system	triclinic	
Space group	P -1	
Unit cell dimensions	a = 9.035(3) Å	α = 108.174(10)°
	b = 13.624(3) Å	β = 96.673(10)°
	c = 15.392(3) Å	γ = 98.257(11)°
Volume	1755.2(7) $Å^3$	
Z	2	
Density (calculated)	1.329 g/cm^3	
Absorption coefficient	0.400 mm^{-1}	
F(000)	716	
Theta range for data collection	1.41 to 27.69°	
Index ranges	-11<=h<=11, -17<=k<=17, -18<=l<=18	
Reflections collected	12349	
Independent reflections	5519 [R(int) = 0.1352]	
Data / restraints / parameters	5519 / 0 / 152	
Goodness-of-fit on F^2	1.162	
Δ/σ_{max}	0.588	
Final R indices	2952 data; I>2σ(I)	R1 = 0.3351, wR2 = 0.6949
	all data	R1 = 0.4314, wR2 = 0.7391
Largest diff. peak and hole	2.573 and -1.782 $eÅ^{-3}$	
R.M.S. deviation from mean	0.307 $eÅ^{-3}$	

7) Network LBM-50 or Zn@H4LOMe

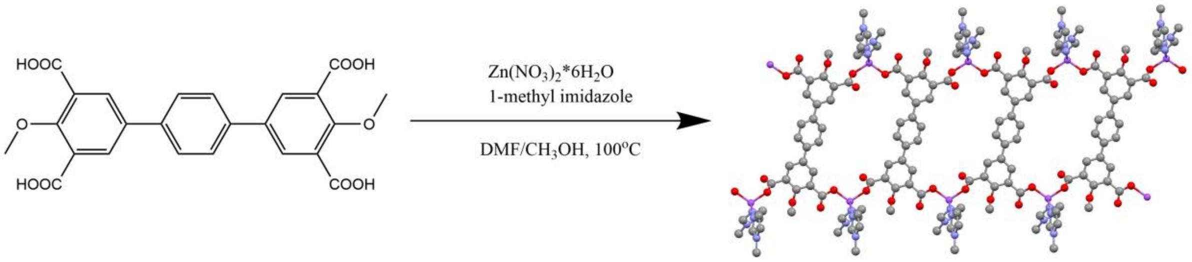

Crystallization conditions: heating of DMF/CH_3OH solution (2/0.5 mL) of **H4LOMe or 22** (1.7 mg, 1 eq) and $Zn(NO_3)_2*6H_2O$ (10.6 mg, 10 eq) and 2 drops 1-methyl imidazole at 100 °C for 24 h.

Chemical formula	$C_{43}H_{45}N_9O_{11}Zn_2$	
Formula weight	994.62 g/mol	
Temperature	173(2) K	
Wavelength	0.71073 Å	
Crystal size	0.100 x 0.100 x 0.120 mm	
Crystal system	triclinic	
Space group	P -1	
Unit cell dimensions	a = 9.2264(4) Å	α = 81.564(2)°
	b = 9.6780(4) Å	β = 76.532(2)°
	c = 14.8129(6) Å	γ = 81.926(2)°
Volume	1264.61(9) $Å^3$	
Z	1	
Density (calculated)	1.306 g/cm^3	
Absorption coefficient	1.010 mm^{-1}	
F(000)	514	
Theta range for data collection	2.42 to 30.12°	
Index ranges	-13<=h<=12, -12<=k<=11, -20<=l<=20	
Reflections collected	26399	
Independent reflections	6753 [R(int) = 0.0448]	
Max. and min. transmission	0.9080 and 0.8810	
Data / restraints / parameters	6753 / 6 / 321	
Goodness-of-fit on F^2	1.044	
$Δ/σ_{max}$	0.006	
Final R indices	6031 data; I>2σ(I)	R1 = 0.0426, wR2 = 0.1307
	all data	R1 = 0.0484, wR2 = 0.1361
Largest diff. peak and hole	1.021 and -0.401 $eÅ^{-3}$	

8) Network LBM-20 or Cu@H4LOH

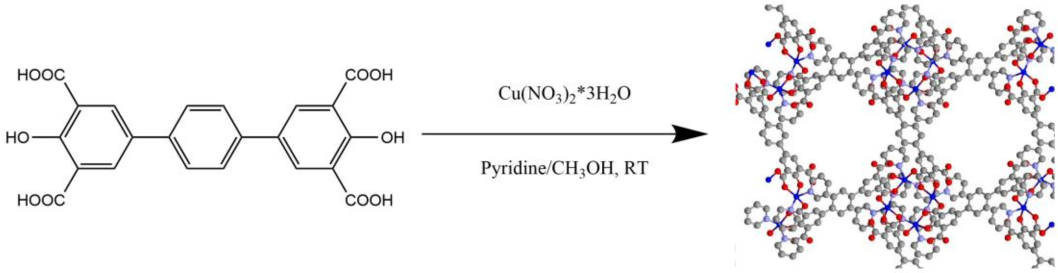

Crystallization conditions: H4LOH or 23 (10.5 mg, 1 eq) dissolved in 2 mL pyridine. $Cu(NO_3)_2*3H_2O$ (37 mg, 6 eq) dissolved in 2 mL of CH_3OH. First pyridine layer added to the tube later 200 µL separation layer and finally methanol layer added. After few days green crystals appeared.

Chemical formula	$C_{47}H_{39}Cu_2N_5O_{12}$	
Formula weight	992.91 g/mol	
Temperature	173(2) K	
Wavelength	0.71073 Å	
Crystal size	0.080 x 0.080 x 0.100 mm	
Crystal system	tetragonal	
Space group	I 41/a	
Unit cell dimensions	a = 32.5970(8) Å	α = 90°
	b = 32.5970(8) Å	β = 90°
	c = 11.1415(3) Å	γ = 90°
Volume	11838.6(7) $Å^3$	
Z	8	
Density (calculated)	1.114 g/cm^3	
Absorption coefficient	0.771 mm^{-1}	
F(000)	4080	
Theta range for data collection	1.77 to 27.88°	
Index ranges	-27<=h<=36, -42<=k<=33, -14<=l<=12	
Reflections collected	14827	
Independent reflections	7040 [R(int) = 0.0530]	
Max. and min. transmission	0.9410 and 0.9270	
Data / restraints / parameters	7040 / 0 / 314	
Goodness-of-fit on F^2	1.017	
Δ/σ_{max}	0.022	
Final R indices	4890 data; I>2σ(I)	R1 = 0.0796, wR2 = 0.2376
	all data	R1 = 0.1115, wR2 = 0.2654
Largest diff. peak and hole	1.645 and -0.478 $eÅ^{-3}$	

9) Network LBM-40 or Ca@H4LOH

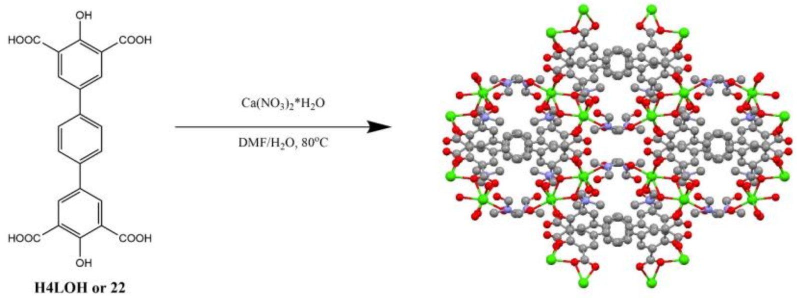

H4LOH or 22

Crystallization conditions: heating of DMF/H_2O solution (2/1 mL) of **H4LOH or 23** (3.3 mg, 1 eq) and $Ca(NO_3)_2*H_2O$ (10.6 mg, 7.5 eq) at 80 °C for 48 h.

Chemical formula	$C_{34}H_{38}Ca_2N_4O_{15}$	
Formula weight	822.84 g/mol	
Temperature	173(2) K	
Wavelength	0.71073 Å	
Crystal size	0.080 x 0.100 x 0.120 mm	
Crystal system	monoclinic	
Space group	C 1 2/c 1	
Unit cell dimensions	a = 19.4072(18) Å	α = 90°
	b = 16.1290(12) Å	β = 92.802(3)°
	c = 12.4575(9) Å	γ = 90°
Volume	3894.8(5) $Å^3$	
Z	4	
Density (calculated)	1.403 g/cm^3	
Absorption coefficient	0.366 mm^{-1}	
F(000)	1720	
Theta range for data collection	1.64 to 28.11°	
Index ranges	-25<=h<=25, -21<=k<=21, -14<=l<=16	
Reflections collected	25478	
Independent reflections	4696 [R(int) = 0.0536]	
Max. and min. transmission	0.8450 and 0.7540	
Data / restraints / parameters	4696 / 12 / 265	
Goodness-of-fit on F^2	1.098	
Δ/σ_{max}	0.056	
Final R indices	3857 data; I>2σ(I)	R1 = 0.0559, wR2 = 0.1496
	all data	R1 = 0.0696, wR2 = 0.1607
Largest diff. peak and hole	0.667 and -0.585 $eÅ^{-3}$	

10) Network SUM-552 or Zn@H2L2@bipy

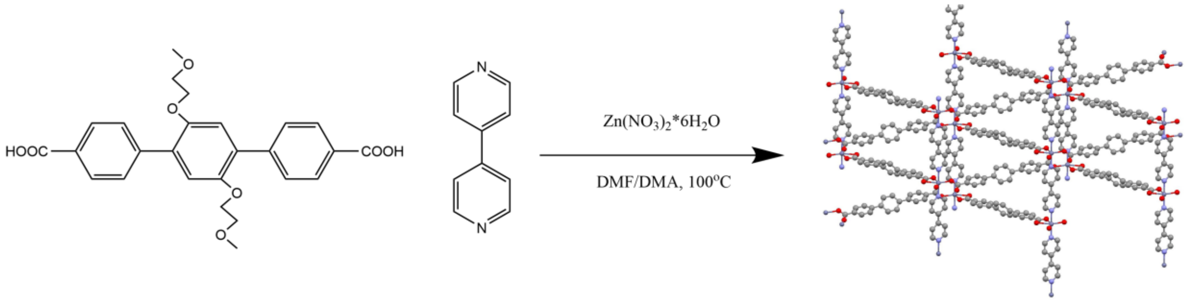

Crystallization conditions: heating of DMF/DMA solution (1/1 mL) of **H2L2 or 14** (6 mg, 1 eq) and $Zn(NO_3)_2$*$6H_2O$ (21 mg, 5.5 eq) and 4,4'-bipyridine (3.1 mg, 1.5 eq) at 100 °C for 24 h.

Chemical formula	$C_{36}H_{32}N_2O_8Zn$	
Formula weight	686.00 g/mol	
Temperature	173(2) K	
Wavelength	0.71073 Å	
Crystal size	0.150 x 0.180 x 0.190 mm	
Crystal system	triclinic	
Space group	P -1	
Unit cell dimensions	a = 8.6864(4) Å	α = 73.801(2)°
	b = 11.4284(5) Å	β = 83.284(2)°
	c = 17.5540(8) Å	γ = 68.094(2)°
Volume	1552.44(12) $Å^3$	
Z	2	
Density (calculated)	1.468 g/cm^3	
Absorption coefficient	0.849 mm^{-1}	
F(000)	712	
Theta range for data collection	1.99 to 28.07°	
Index ranges	-11<=h<=11, -15<=k<=15, -23<=l<=23	
Reflections collected	240457	
Independent reflections	7048 [R(int) = 0.0651]	
Max. and min. transmission	0.7458 and 0.6346	
Data / restraints / parameters	7048 / 9 / 455	
Goodness-of-fit on F^2	1.035	
Δ/σ_{max}	0.001	
Final R indices	6696 data; I>2σ(I)	R1 = 0.0370, wR2 = 0.0922
	all data	R1 = 0.0392, wR2 = 0.0940
Largest diff. peak and hole	1.163 and -1.173 $eÅ^{-3}$	

11) Network SUM-503 or Zn@H2L3

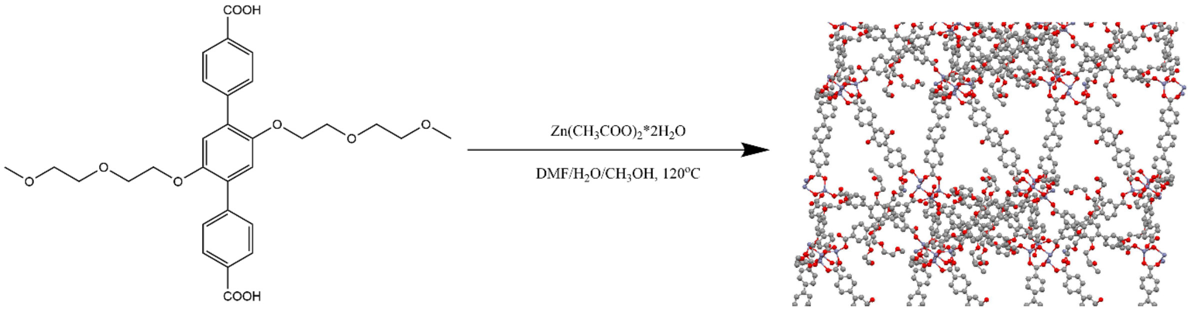

H2L3 or 14

Crystallization conditions: heating of $DMF/H_2O/CH_3OH$ solution (1/1/1 mL) of **H2L3 or 15** (10 mg, 1 eq) and $Zn(CH_3COO)_2*2H_2O$ (45 mg, 13.5 eq) at 120 °C for 48 h.

Formula	$C_{180} H_{30} N_{30} O_{30} Zn$
Space group	P -1
Cell lengths	**a** 18.0412(8) **b** 20.5164(11) **c** 28.7012(13)
Cell angles	**a** 87.969(2) **b** 71.835(2) **g** 64.132(2)
Cell volume	9019.56
Z	**Z**: 2
R factor (%)	15.26

12) **Network SUM-603 or Zr@H2L3**

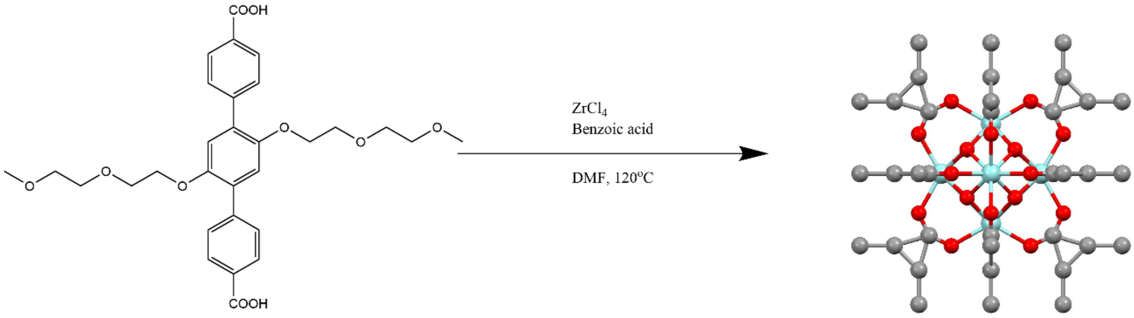

H2L3 or 14

Crystallization conditions: heating of DMF (2 mL) solution of **H2L3 or 15** (4 mg, 1 eq) and $ZrCl_4$ (4.7 mg, 3 eq) and benzoic acid (50 mg, 58 eq) at 120 °C for 24 h.

Formula	$C_6 O_{16} Zr_3$
Space group	F m -3 m
Cell lengths	**a** 32.5040(8) **b** 32.5040(8) **c** 32.5040(8)
Cell angles	**a** 90 **b** 90 **g** 90
Cell volume	34340.8
Z	48
R factor (%)	17.45

Nizami ISRAFILOV

Élaboration de nouveaux matériaux de types MOF dotés de fonctionnalités supramoléculaires. Synthèse, études physicochimiques et applications.

Résumé

La constante de liaison élevée et la sélectivité des composés supramoléculaires, principalement des éthers couronnes et des cryptands, nous ont inspirés à créer des structures similaires en incorporant des groupes porteurs de glyme à l'intérieur (également à l'extérieur) des pores des Metal-Organic Frameworks (MOF), eux-mêmes basés sur la principe auto-assemblage de la chimie supramoléculaire.

Le premier chapitre décrit la synthèse des ligands avec des groupes glyme de différentes longueurs, également l'amélioration de la procédure de synthèse.

Le deuxième chapitre porte sur la synthèse de nouvelles séries de MOF, SUM (Strasbourg University Materials) et LBM (Le Bel Materials), leurs hybrides avec la silice SBA-15, et la caractérisation physico-chimique de ces composés via différentes méthodes : SCXRD, PXRD , FT-IR, TGA, SEM, TEM et BET.

Le troisième chapitre traite de l'application (principalement l'adsorption) des MOF par rapport à différentes molécules invitees. Avec SUM-103 à 273K et 10 bar, une adsorption exceptionnelle de 38.5 mmol g^{-1} de CO_2 a été obtenue, également SUM-103 a montré une adsorption de 194 ± 4 mg g^{-1} de bleu de méthylène dans l'eau. Un autre résultat intéressant était la capacité d'absorption volumétrique élevée de SUM-102 pour le formaldéhyde (1007 g m^{-3}), qui est près de deux fois supérieure à la référence HKUST-1. Enfin, nous terminons la thèse par la conclusion générale, où nous résumons tous les chapitres mentionnés ci-dessus et écrivons sur notre vision de l'avenir des MOF.

Mots clés : Interactions supramoléculaires, MOF, SUM, adsorption, glyme, colorant, CO_2, BET.

Résumé en anglaise

The high binding constant and the selectivity of supramolecular compounds, mainly crown ethers and cryptands inspired us to create similar structures by incorporating glyme bearing groups inside (also outside) the pores of Metal-Organic Frameworks (MOFs), which itself based on the self-assembly principle of supramolecular chemistry.

The first chapter describes the synthesis of the ligands with various length glyme groups, also an improvement of the synthesis procedure.

The second chapter is about the synthesis of new MOF series, namely SUM (Strasbourg University Materials) and LBM (Le Bel Materials), their hybrids with SBA-15 silica, and physio-chemical characterization of these compounds via various methods: SCXRD, PXRD, FT-IR, TGA, SEM, TEM, and BET.

The third chapter discusses the application (mainly adsorption) of the MOFs versus different guest molecules. With SUM-103 at 273K and 10 bar, outstanding 38.5 mmol g^{-1} CO_2 adsorptions were obtained, also SUM-103 showed 194 ± 4 mg g^{-1} methylene blue adsorption in water. Another interesting result was the high volumetric uptake capacity of SUM-102 for formaldehyde (1007 g m^{-3}), which is nearly twice higher than benchmark HKUST-1. Finally, we finish the thesis with the general conclusion, where we summarize all the beforementioned chapters and write about our vision of the future of the MOFs.

Keywords: Supramolecular interactions, MOF, SUM, adsorption, glyme, dye, CO_2, BET